

DISSERTATION

Computational Simulation of the Thermal Conductivity of MMCs under Consideration of the Inclusion–Matrix Interface

ausgeführt zum Zwecke der Erlangung des akademischen Grades eines
Doktors der technischen Wissenschaften unter der Leitung von

ao.Univ.Prof. Dipl.-Ing. Dr.techn. Helmut J. BÖHM, MSc
E317
Institut für Leichtbau und Flugzeugbau

eingereicht an der Technischen Universität Wien
Fakultät für Maschinenbau

von

Dipl.-Ing. Dominik DUSCHLBAUER
Matrikelnummer: 9331820
Vergeinerstr. 19
A-4240 Freistadt

Wien, im Dezember 2003

Dominik Duschlbauer

Acknowledgements

I am deeply indebted to my thesis advisor, Prof. H. J. Böhm, and my FWF project manager, Dr. H. E. Pettermann, for their invaluable assistance in preparing this work, for their never ending patience in long discussions, as well as their patience with any of my many “quick” questions. I also would like to thank Prof. H. P. Degischer for agreeing to act as a coadvisor.

I gratefully acknowledge the financial support of my studies by the Austrian Science Fund (FWF), grant P14532-PHY.

I also wish to acknowledge the fruitful discussions with Erich Neubauer, Austrian Research Centers Seibersdorf, Austria.

Additionally, I would like to express my thanks to all my former and current colleagues at the ILFB, who have always been helpful and friendly. The positive atmosphere at the ILFB has helped me during many scientific setbacks and made my time at the ILFB an inspiring and interesting period.

Abstract

Steadily increasing clock speeds and miniaturization in microelectronics are leading to increasing power densities. Accordingly, there is a demand for new, advanced materials in electronic package design that allow to engineer higher density systems. Certain metal matrix composites are promising candidate materials for electronic packaging applications due to the possibility of tailoring their properties. The latter, however, requires deep understanding and a thorough insight into the mechanisms of interaction between the constituents on the microlevel and of their effect on the overall behavior.

The present study aims to improve the understanding of heat conduction in composite materials, special attention is paid to the effects of imperfectly bonded constituents, i.e. the presence of interfacial thermal resistances.

An overview of selected analytical and numerical methods for describing the overall behavior of composite materials is provided. Subsequently, an introduction into hot pressed carbon–copper composites is given, which have high potential for electronic packaging applications.

Mori–Tanaka mean field approaches, among them newly developed methods, and a periodic microfield approach form the backbone of computational methods, which are employed in this work to estimate the effective conductivity of composites. These methods are discussed in detail in Chapter 4, where also the topic of heat conduction in homogeneous solids is addressed and the limits and assumptions underlying the employed micromechanical approaches are critically reviewed.

Single inclusion problems (i.e. solitary, imperfectly bonded inclusions embedded in an isotropic, unbounded matrix), are studied. For the case of ellipsoidal inclusion geometries an analytical method is developed which enables replacement of the original imperfectly bonded inclusion by a less conductive but perfectly bonded inclusion. The replacement formalism is extended to arbitrary inclusion shapes, the solution technique involving “di-

lute” unit cells. This numerical replacement procedure in combination with the Mori–Tanaka scheme forms a very versatile, “hybrid” micromechanical tool.

Results are presented primarily for carbon–copper composites. Different microgeometries are investigated and Mori–Tanaka predictions are compared with unit cell predictions, as well as with experimental results.

Kurzfassung

Höhere Taktraten und Miniaturisierung erzeugen immer größere Leistungsdichten in mikroelektronischen Bauteilen. Um eine Überhitzung zu vermeiden ist ein effizienter Wärmeabtransport nötig. Gewisse Metallmatrix Verbundwerkstoffe sind dafür vielversprechende Materialien, da sie es dem Ingenieur erlauben, spezielle Eigenschaften gezielt “maßzuschneidern”. Letzteres erfordert jedoch ein sehr gutes Verständnis der Wechselwirkungen der unterschiedlichen Konstituenten eines Verbundwerkstoffes untereinander und deren Auswirkungen auf die effektiven Eigenschaften des Verbundwerkstoffes.

Die vorliegende Arbeit untersucht die Wärmeleitung in Verbundwerkstoffen, wobei ein spezielles Augenmerk auf den Einfluß von thermischen Widerständen auf die effektive Wärmeleitfähigkeit gelegt wird.

In der Arbeit wird zunächst ein Überblick über ausgewählte analytische und numerische mikromechanische Methoden gegeben, welchem eine kurze Beschreibung der untersuchten Kohlefaser-Kupfer Verbundwerkstoffe folgt, die großes Potential für die Anwendung in Wärmesenken besitzen.

Um die effektive Wärmeleitfähigkeit von Verbundwerkstoffen zu berechnen werden in dieser Arbeit hauptsächlich die Mori-Tanaka Methode und die Einheitszellen Methode verwendet. Diese Verfahren werden ausführlich in Kapitel 4 diskutiert. In diesem Kapitel wird auch ein kurzer Überblick zur Wärmeleitung in homogenen Festkörpern gegeben und es werden die den Methoden zugrundeliegenden Annahmen und Einschränkungen kritisch betrachtet.

Konfigurationen bestehend aus einzelnen Inklusionen, welche in einer unendlich grossen isotropen Matrix eingebettet sind, werden unter Berücksichtigung thermischer Kontaktwiderstände am Interface untersucht. Für den Fall ellipsoidaler Inklusionsgeometrien wird eine analytische Methode hergeleitet, welche es erlaubt, die Inklusion mit Kontaktwiderstand durch eine schlechter leitende zu ersetzen, welche perfekt mit der umgebenden

Matrix verbunden ist (d.h. ohne thermischen Kontaktwiderstand). Weiters wird eine verallgemeinerte Variante dieser Austauschoperation basierend auf Einheitszellen für beliebige Inklusionsgeometrien hergeleitet. Gemeinsam mit der Mori–Tanaka Methode formt diese numerische Austauschoperation ein mächtiges, “hybrides” mikromechanisches Werkzeug.

Resultate werden primär für Kohlefaser–Kupfer Verbundwerkstoffe berechnet. Verschiedene Mikrogeometrien werden untersucht und die Ergebnisse der Mori–Tanaka–Methode werden mit denen von Einheitszellen verglichen, sowie mit Experimenten.

Notation

Tensors up to the second rank are used in this work. The rank equals the number of subscripts.

- Tensors of rank zero (“scalars”) are not connected with any direction and therefore unrelated to any axis of reference. They are completely specified by a single number. Examples: Temperature T and density γ .
- Tensors of rank one (“vectors”) are given by three scalar components for a given set of linearly independent reference axes. Examples: Temperature gradient $T_{,i}$ and heat flux q_i .
- Tensors of rank two are given by nine numbers and relate two vectors. Examples: Thermal conductivity K_{ij} .

Dummy Suffix Notation

The Einstein summation convention is used in this work: Unless stated otherwise, if a subscript occurs twice in any term, summation from 1 to 3 with respect to that suffix is automatically understood. Dummy suffixes *must* occur as pairs in a term. If a suffix occurs once in a term, it is called a “free suffix”. The same free suffixes must be present in *all* terms on *both* sides of an equation.

A suffix i following a comma denotes differentiation with respect to x_i .

Some Remarks to First Rank Tensors

Note that x_i can refer to a *direction* of a principal axis as well as to the *coordinates* of a point. The latter is also denoted by \vec{x} .

Some Remarks to Second Rank Tensors

Kronecker Delta The Kronecker delta, δ_{ij} , is defined as

$$\delta_{ij} = \begin{cases} 0 & \text{for } i \neq j \\ 1 & \text{for } i = j \end{cases} .$$

The Kronecker delta can also be given in terms of the derivatives of the direction vectors x_i :

$$\delta_{ij} = \frac{\partial x_i}{\partial x_j} = x_{i,j}$$

Note that $\delta_{ii} = 3$.

Principal Components, Principal Axes An important property of *symmetric* second rank tensors is their possession of principal axes which are three directions at right angles defining a coordinate system. With respect to this coordinate system the second rank tensor takes the form of a diagonal tensor, i.e. off diagonal terms are zeros. The diagonal terms are referred to as principal components and are indicated by capital roman subscripts, I, II, and III, where I and III stand for the maximum and minimum principal components, respectively.

Commonly used Superscripts

- (*) overall effective, uniform far field
- (i) inclusion phase
- (m) matrix phase
- (r) any phase

Contents

Abstract	II
Kurzfassung	IV
Notation	VI
1 Introduction	1
1.1 Motivation	1
2 Micromechanics: Some Basic Definitions	4
2.1 Length Scales, Homogenization, Localization	4
2.2 Basic Micromechanical Strategies	6
3 The investigated MMC: Carbon–Copper Composites	12
3.1 Production Routes	12
3.2 Fiber Arrangements, Aggregates, Aspect Ratio Distributions	14
3.3 Material Properties	16
3.4 Interfacial Thermal Barriers	18
4 Micromechanical Methods	21
4.1 Heat Conduction in Homogeneous Solids	21
4.2 The Mori–Tanaka–Method	26
4.3 Periodic Microfield Approach	39

<i>CONTENTS</i>	IX
5 Single Inclusion Problems	46
5.1 Spheroidal Inhomogeneities	47
5.2 Non-ellipsoidal Inhomogeneities	72
5.3 Symmetry Relations	76
6 Some Results for Single Inclusion Problems	78
6.1 Perfectly Bonded Cylinders	79
6.2 Imperfectly Bonded Cylinders	88
7 Results for Aligned Carbon Fibers	95
7.1 Aligned Continuous Fibers	97
7.2 Aligned Staggered Short Fibers	102
8 Results for Randomly Oriented Carbon Fibers	109
8.1 Three Dimensional Random Fiber Arrangements	110
8.2 Planar Random Fiber Arrangements	123
8.3 The Influence of Microtopological Descriptors	136
9 Conclusions	147
A Orientational Averaging	149
Curriculum Vitae	153
Bibliography	153

Chapter 1

Introduction

Composite materials consist of two or more different prefabricated constituents. If the latter are uniformly distributed the material can be treated as a homogeneous continuum at a sufficiently large length scale. Composites are found in nature as well as in engineered materials. They have proven highly attractive for a broad spectrum of engineering applications due their inherent capability at being designed with overall properties that meet certain demands.

Introductions to modeling of the thermo–physical behavior of composites may be found in e.g. [1], with extensive lists of references given therein.

1.1 Motivation

1.1.1 Outline of the Problem

In the 1960's Moore made the prediction that the performance of microprocessors would double every 18 months [2]. Now, some 35 years later developments still supports Moore's prediction (commonly known as "Moore's law"). However, steadily increasing clock speeds which goes in hand with miniaturization (i.e. increasing numbers of gates per unit area of the silicon) in microelectronics has been creating problems of heat dissipation. For example, the die size of a Pentium 4 is 12.5 mm square and dissipates up to 80 W [3], corresponding to an average energy density of 0.5×10^6 W/m². Note that the on–die power distribution is typically not uniform and at spots of local power concentrations ("hot spots") the energy densities are much higher. The same trend can be observed in the field of power electronics

where transistors can generate up to $3 \times 10^6 \text{ W/m}^2$?.

So far there is no indication that the power dissipation is reaching a plateau and it is apparent that for the near future power dissipation will be a major bottleneck across the microelectronics industry ?, defining the limits of performance and reliability of electronic systems. Accordingly, efficient thermal management which can maintain low operating temperatures (i.e. ensure consequent electrical performance) is essential, for the full potential of future technologies to be realized.

1.1.2 Thermal Management Issues

Electronic package design is a sophisticated electrical, thermal, and mechanical task. Overviews and recent developments as well as references may be found in ??????. In the following a brief introduction which is geared towards heat spreaders and thermal issues is given. On the left hand side of Fig. 1.1 a schematic set up of an electronic package is depicted. The package can be thought of as a series connection of thermal resistances. The overall thermal resistance not only depends on the conductive properties of the components and their dimension in the direction of the heat flow but also on the thermal contact resistances between the interface material, the heat sink, and the die. In order to dissipate heat to the surrounding environment a temperature mismatch between the surface of the heat sink and the ambient temperature is necessary. The latter can be interpreted in terms of another

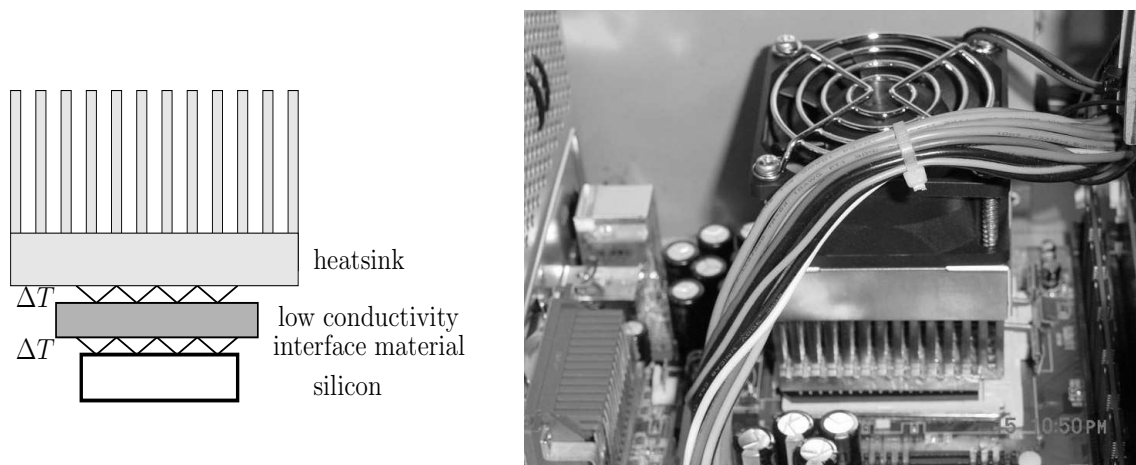


Figure 1.1: Schematic setup of an electronics package (left) and a typical standard PC application (right, from <http://bonez.net/pictures/pages/heatsink.htm>).

thermal resistance, and forced convection is usually employed to keep this contribution small, compare Fig. 1.1, right.

The temperature of the silicon is then determined by the heat it is generating, the overall thermal resistance of the package, and the ambient temperature.

From Fig.1.1, left, several key criteria for a heat sink can be readily derived from a “materials point of view”, which are

- adapted coefficients of thermal expansion (CTE) of the components
- stability during thermal cycling
- high thermal conductivity
- low specific weight

The latter point is especially relevant in the aerospace and automotive industry where weightsaving is optimistically correlated to saving costs of 500–5000 €/kg and 2–50 €/kg, respectively ?.

Today’s competitive environment has increased the role of advanced materials in electronics package design. Optimization has spurred the development of new materials that allow to design higher density systems. Certain metal matrix composites (MMCs) are ideal for electronic packaging applications, because of the possibility of tailoring their thermo-mechanical and thermophysical properties. The coefficient of thermal expansion (CTE) and the thermal conductivity are the two most important design parameters for heat spreader materials.

In industry copper and copper-based composites have been mainly used where high electrical and high thermal conductivities are required. Pure copper, however, has a much higher CTE than semiconductors and their substrates. The high thermal conductivity, low mass density, and negative axial CTE of carbon fibers make carbon-copper composites potential candidates for use in thermal management applications.

Chapter 2

Micromechanics: Some Basic Definitions

2.1 Length Scales, Homogenization, Localization

The description of the properties of composite materials has to account for two length scales at least. On the *macroscale* a composite may be viewed as a material with smeared out or homogenized properties while on some small length scale (the *microscale*) different constituents can be distinguished:

- Macroscale: the length scale of the structure, component, or sample
- Microscale: the length scale of the reinforcement diameters or distances

Below the microscale a number of “sub microscales” can typically be identified, accounting for e.g. polycrystalline or porous constituents of a composite material.

In this work the constituent materials are approximated to be homogeneous on the microscale. The framework of continuum mechanics is chosen for studying the conduction of heat in heterogeneous solids, the behavior of the constituents is described by constitutive laws. In analogy to studies of the thermomechanical behavior of inhomogeneous materials this approach is referred to as continuum micromechanics.

The central aim of micromechanical descriptions of composites is the bridging of the length scales. One main effort of theoretical studies of composite materials is to deduce overall or effective properties from the known material properties of the constituents, their

arrangement on the microscale, and the properties of the interfaces between the constituents. This scale transition from the micro to the macro scale is referred to as *homogenization* and is usually carried out by volume averaging of the microfields. The transition from the macro scale to the micro scale is referred to as *localization*. It allows to “zoom in” on the local microfields due to macroscopic loading.

In micromechanical approaches the microfields (heat flux and temperature gradient in the case of heat conduction problems) in an inhomogeneous material are typically split into contributions corresponding to the different length scales, which may be termed “fast” and “slow” variables. It is assumed that the length scales are sufficiently different so that

- variations of the temperature gradient and flux fields on the microscale (fast variables) influence the macroscale behavior only by their average values (i.e. from the point of view of the macroscale the composite acts as a bulk material)
- variations of the temperature gradients or fluxes on the macroscale (slow variables) are not significant at the microscale, where these fields appear to be locally constant and act as “applied” homogeneous far field temperature gradients or fluxes.

If the macrofield fluctuates rapidly the situation drastically changes and goes beyond the scope of this work, for details and references see ??.

2.1.1 Basic Notation

Homogenized temperature gradients, $T_{,i}^{(*)}$, and fluxes, $q_i^{(*)}$, take the form

$$T_{,i}^{(*)} = \frac{1}{V} \int_V T_{,i}(\vec{x}) \, dV = \frac{1}{V} \int_\Gamma T|_\Gamma n_i \, d\Gamma \quad , \quad (2.1)$$

$$q_i^{(*)} = \frac{1}{V} \int_V q_i(\vec{x}) \, dV = \frac{1}{V} \int_\Gamma q_j n_j x_i \, d\Gamma \quad . \quad (2.2)$$

Here, Γ is the surface of the control volume V , n_i stands for the associated surface normal unit vector, and $T|_\Gamma$ are the temperatures on the external surface of volume V . In Eqs. (2.1) and (2.2) the divergence theorem (“Gauss theorem”) is utilized to express a volume integral with a surface integral. Note that this equivalence holds for perfectly bonded constituents and the absence of cracks only. If the latter conditions are not fulfilled, either appropriate corrections terms must be introduced into the volume integral formulations ?? or imperfectly bonded constituents must be replaced by perfectly bonded constituents of reduced

conductivity. The latter approach is pursued in this work. Note that the same fundamental relations hold in the context of elasticity as well, where volume averaged strains and stresses are replaced by boundary displacements and tractions, respectively, provided the constituents are perfectly bonded.

The local temperature gradient fields, $T_{,i}(\vec{x})$, and flux fields, $q_i(\vec{x})$, at the micro scale in relation to macroscopic fields are of considerable interest. The localization relations can be formally denoted as

$$T_{,i}(\vec{x}) = D_{ij}(\vec{x}) T_{,j}^{(*)} \quad , \quad (2.3)$$

$$q_i(\vec{x}) = F_{ij}(\vec{x}) q_j^{(*)} \quad , \quad (2.4)$$

where $D_{ij}(\vec{x})$ and $F_{ij}(\vec{x})$ are known as the temperature gradient concentration tensor and flux concentration tensor (or localization tensors), respectively.

The microtopology of real composites is, at least to a certain extent, stochastic and highly complex. Exact expressions for the localization tensors cannot realistically be provided and approximations have to be introduced.

Typically, these approximations are based on the ergodic hypothesis, i.e. it is assumed that the heterogeneous material is statistically homogeneous. This implies that randomly selected and sufficiently large subvolumes within a sample give rise to the same effective material properties. The subvolume investigated for the purpose of homogenization is referred to as the representative volume element (RVE). The dimensions of a RVE define the *miniscale*. Ideally, it should be sufficiently large so that ensemble averages and RVE averages are the same (i.e. allowing for a meaningful sampling of the microfields). On the other hand, the RVE must be sufficiently small from a macroscopic view and for an analysis of the microfields to be computationally feasible. These conditions may be symbolically written as MICRO \ll MINI \ll MACRO, with the miniscale being some intermediate length scale that is characteristic of the size of the volume elements used for averaging.

For a more thorough discussion of RVEs see [1].

2.2 Basic Micromechanical Strategies

Homogenization methods aim to find an RVE's response to prescribed loads. In the case of heat conduction the loads typically take the form of uniform far field temperature gradient fields or flux fields. The homogenization procedures described in this section can all be employed as micromechanically based constitutive material models at higher length scales,

i.e. they can link the homogenized fluxes to the homogenized temperature gradients¹. Localization procedures are used for finding the local response of the phases for given macroscopic loads. With the exception of bounding methods, all discussed micromechanical strategies can be utilized as localization procedures as well.

In the following overview micromechanical homogenization techniques are categorized into two main groups, models based on *averaged* microfields and models based on *resolved* microfields.

This division is not strict as in this work a “hybrid” approach, i.e. combination of both methods is used to advantage.

2.2.1 Models Based on Averaged Microfields

Methods based on averaged microfields describe the microgeometry of inhomogeneous materials on the basis of statistical information. These methods typically hinge upon idealized ellipsoidal inclusion geometries and the underlying mathematics is tractable by means of tensor analysis. Therefore these methods are sometimes referred to as “analytical methods”, a term which is not necessarily applicable in the strict sense.

Mean Field Approaches

Mean Field Approaches (MFAs) in micromechanics aim to obtain the overall properties of inhomogeneous materials, such as their overall conductivity and resistivity tensors, $K_{ij}^{(*)}$ and $R_{ij}^{(*)}$, respectively, in terms of appropriate phase properties. The descriptions being based on phase averaged temperature gradient fields $\bar{T}_{,i}^{(r)}$ and phase averaged flux fields $\bar{q}_i^{(r)}$. Such descriptions use information on the microtopology, such as the inclusion shape and orientation, and (to some extent) the statistics of the microgeometry. The localization relations take the form

$$\bar{T}_{,i}^{(r)} = \bar{D}_{ij}^{(r)} T_{,j}^{(*)} \quad , \quad (2.5)$$

$$\bar{q}_i^{(r)} = \bar{F}_{ij}^{(r)} q_j^{(*)} \quad , \quad (2.6)$$

and the effective fields become

$$T_{,i}^{(*)} = \sum_r \xi^{(r)} \bar{T}_{,i}^{(r)} \quad , \quad (2.7)$$

¹With the exception of bounding methods where two sets of homogenized properties are obtainable, corresponding to an upper and lower bound.

$$q_i^{(*)} = \sum_r \xi^{(r)} \bar{q}_i^{(r)} \quad , \quad (2.8)$$

where (r) stands for a phase of the composite and $\xi^{(r)}$ is its corresponding volume fraction. Note that for MFAs the averaged phase concentration tensors $\bar{D}_{ij}^{(r)}$ and $\bar{F}_{ij}^{(r)}$ are not functions of the spatial coordinates within the RVE (contrary to Eqs. (2.3) and (2.4)). Mean field equations tend to be formulated in terms of the phase concentration tensors. They have a clear physical background and an inherent capability for "zooming in" on the micro fields. MFAs have proven highly successful for describing the linear and nonlinear thermomechanical behavior of inhomogeneous materials as well as any type of transport problem obeying the Laplace equation (e.g. thermal and electrical conductivity, dielectric and magnetic permeability).

From a practical point of view some important mean field approaches are Mori–Tanaka methods ???, self-consistent schemes ??, and differential schemes ?? which provide estimates for the overall behavior of inhomogeneous materials with different microstructures. In Section 4.2 the Mori–Tanaka method is discussed in detail as it is used in a substantial part of the present work.

Bounding Methods

If only limited information about the microgeometry of a composite is available, it is good practice to find an interval to which the effective properties of the composite must be limited based on energetical considerations. This interval is bounded by the *upper* and *lower* bounds. The more information on the phase arrangement of the composite is available, the tighter the bounds.

The results presented in this section apply to perfect thermal interfaces.

Wiener Bounds The simplest bounding expression is given by the Wiener bounds ? which in their tensorial form read as

$$\left[\sum_r \xi^{(r)} R_{ij}^{(r)} \right]^{-1} \leq K_{ij}^{(*)} \leq \sum_r \xi^{(r)} K_{ij}^{(r)} \quad . \quad (2.9)$$

The effective conductivity of a composite material must always lie in between the Wiener bounds, independent of its microstructure. These bounds are universal and very simple but they are usually too slack for practical use. The Wiener bounds have their equivalent in elasticity with the Hill bounds ?. If the Poisson numbers of the constituents fulfil special

conditions, the upper and lower Hill bound coincide with the Voigt bounds and Reuss bounds, respectively.

Note that the upper Wiener bound is sharp for uniform temperature gradient fields and the lower Wiener bound is sharp for uniform flux fields. Accordingly, the effective axial conductivity of microgeometries of unidirectional, continuous fibers embedded in a matrix material can be computed with the right hand side of Eq. (2.9). The Wiener bounds are also strictly fulfilled for control volumes that are too small to be RVEs.

Hashin–Shtrikman Bounds The Hashin–Shtrikman bounds (HS bounds) apply to inhomogeneous materials with statistically isotropic overall symmetry and are much tighter than the Wiener bounds. Hashin and Shtrikman ? established variational theorems and subsequently derived bounds on the effective magnetic permeability of macroscopically homogeneous and isotropic multiphase materials which can be utilized for heat conduction as well. For a two phase heterogeneous material with isotropic phases ($K^{(1)} > K^{(2)}$) and isotropic overall conductivity the HS lower bound is given by

$$K_{\text{HS}}^{\text{l.b.}} = \xi^{(1)}K^{(1)} + \xi^{(2)}K^{(2)} - \frac{\xi^{(1)}\xi^{(2)}[K^{(2)} - K^{(1)}]^2}{3K^{(2)} - \xi^{(2)}[K^{(2)} - K^{(1)}]} \quad , \quad (2.10)$$

and the HS upper bound is given by

$$K_{\text{HS}}^{\text{u.b.}} = \xi^{(1)}K^{(1)} + \xi^{(2)}K^{(2)} - \frac{\xi^{(1)}\xi^{(2)}[K^{(2)} - K^{(1)}]^2}{3K^{(1)} + \xi^{(1)}[K^{(2)} - K^{(1)}]} \quad . \quad (2.11)$$

The effective conductivity of any macroscopically isotropic composite must satisfy

$$K_{\text{HS}}^{\text{l.b.}} \leq K^{(*)} \leq K_{\text{HS}}^{\text{u.b.}} \quad . \quad (2.12)$$

If $K^{(1)} < K^{(2)}$, Eqs. (2.10) and (2.11) still hold but with exchanged values of the upper and lower bounds.

Composites with randomly oriented anisotropic inclusions exhibit macroscopically isotropic effective conductivities and therefore satisfy Eq. (2.12). For anisotropic effective conductivities the HS bounds do not apply. The formalism employed by Hashin and Shtrikman is generalized to anisotropic composites by Kohn and Milton ? and Milton ?, where an extensive list of references is provided. For the case of oriented anisotropic inclusions of arbitrary shape, Walpole ? derived bounds on the effective elastic moduli. Eduljee and McCullough ? provide HS–type bounds on the effective elastic properties of discontinuous fiber reinforced composites. Solutions for the elastic case can immediately be transformed and applied to heat conduction problems.

Improved Bounds and Bounds for Imperfectly Bonded Phases Tighter bounds can be obtained when more detailed information on the microstructure than phase volume fractions and overall symmetries are considered, such as statistical information in the form of n -point correlation functions on the phase arrangement. Details relating to spherical inclusion geometries can be found in ???.

The bounding methods presented up to this section apply for perfect interfaces only. For the case of imperfectly bonded constituents Lipton and Vernescu ? derived lower bounds in terms of the interfacial surface area, constituents' volume fractions, constituents' conductivities, and the interfacial thermal properties.

2.2.2 Models Based on Resolved Microfields

Another group of strategies employs simplified microgeometries for which the microfields are resolved to a high degree at the cost of restrictions to the generality of the microstructure. Appropriately reconstructed microstructures can be viewed as realizations of the underlying phase arrangement statistics. Accordingly, results from sets of simulations of different model geometries may be evaluated in terms of ensemble averages. For algorithms reconstructing matrix-inclusion microgeometries to approximate predefined statistical descriptors see e.g. ?.

Typical applications of models based on resolved microstructures comprise non-linear material behavior, non-ellipsoidal inclusion shapes, and detailed investigations of inclusion-inclusion interaction effects.

Models based on resolved microgeometries typically employ standard numerical engineering methods for resolving the microfields such as the Finite Difference Method, the Boundary Element Method, and the Finite Element Method.

Periodic Microfield Approach

Periodic microfield approaches aim at describing the macroscale and microscale behavior of heterogeneous media by investigating model composites with periodic phase arrangements. The corresponding periodic microfields are typically obtained by analyzing a unit cell by analytical or numerical methods. Together with the Mori-Tanaka method periodic microfield approaches form the backbone of computational tools employed in this work and a detailed discussion is given in Section 4.3.

Windowing Methods

Windowing methods are based on placing test windows at random positions in an inhomogeneous material and subjecting them to homogeneous temperature gradient and flux boundary conditions, respectively. Provided sufficiently large windows are chosen, predictions of this type give rise to lower and upper estimates, respectively ?. Ensemble averages of such estimates in turn provide upper and lower bounds on the overall effective conductivity of the material. While for small window sizes boundary perturbations may give rise to slack bounds, for sufficiently large window sizes (i.e. RVEs) the bounds coincide. Effects of boundary conditions for various two-dimensional arrangements in the context of heat conduction are studied by Jian *et al.* ?.

Embedding Methods

The real composite is approximated by a model consisting of a core containing a discrete phase arrangement that is surrounded by an outer region with smeared-out material properties to which the boundary conditions and loads are applied. The material properties of the outer region may be assigned a priori, they can be determined self-consistently, or the outer region is modelled as a heterogeneous material with a very coarse phase arrangement to reduce computational cost.

Embedding methods are especially useful for studying regions where homogenization conditions are not met, e.g. due to high macroscopic gradients.

Chapter 3

The investigated MMC system: Carbon–Copper Composites

Because most investigations in the present study relate to hot pressed short fiber carbon–copper composites a short overview of several aspects of this composite material is given in this chapter.

3.1 Production Routes

Bundles of continuous carbon fibers are chopped to lengths ranging from 400 μm to 700 μm . Subsequently the fibers are desized, i.e. they are subjected to heat treatment at temperatures around 300°C–400°C which removes/burns the resin binders that were added on the fibers during production. Due to the poor wettability of carbon by copper the carbon fibers must be precoated before hot pressing. Two different coating technologies of practical importance are considered, an electrochemical coating process and sputter deposition. Both technologies influence the fiber–matrix adhesion and thermal interface properties significantly ???. Coated fibers (and copper powder) are mixed in order to ensure a homogeneous distribution, and are then consolidated and evacuated. Finally, a defined hot pressing sequence follows.

Electrochemical Fiber Coatings Carbon fibers are electrochemically precoated with copper, the thickness reaching up to an equivalent of 50% copper and more, $\xi^{(Cu)} = 0.5$. As the copper–coatings form the entire matrix after hot pressing, no additional copper powder

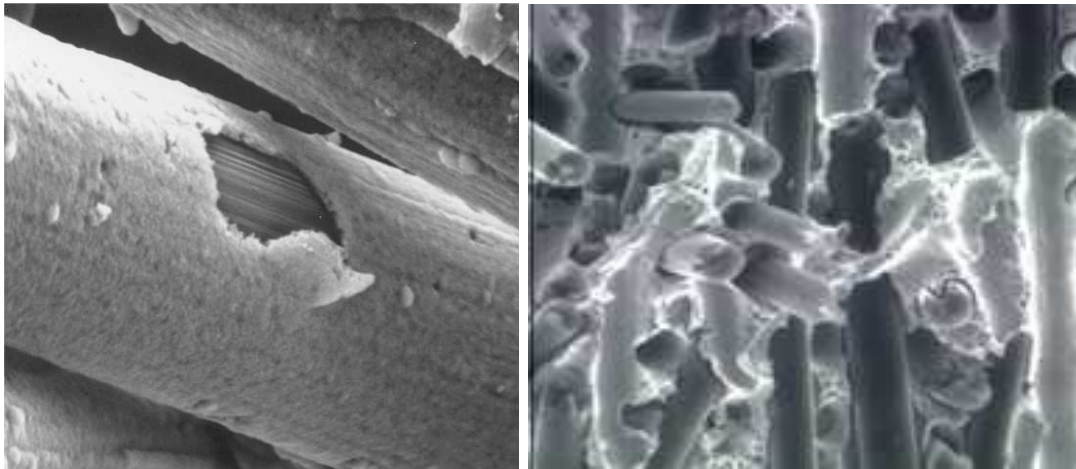


Figure 3.1: Copper coatings applied electrochemically suffer from weak adhesion with the carbon fibers. Fracture surfaces typically show pulled out fibers (right). ?

is required. The coated fibers are consolidated and then the precompact composite is hot pressed, for details see ???. One disadvantage of this production route is the relatively weak adhesion between the copper matrix and the fiber (Fig. 3.1).

Sputter Deposition If copper is deposited on the fiber via sputter deposition ?, the fiber–matrix adhesion can be improved by a factor of up to 10 in terms of pull–off tests when compared to coatings deposited electrochemically ?, with a concomitant improvement of the thermal interfacial conductances. The sputter deposition process also allows for depositing adhesion promoters such as Cr, Ti, and Mo in thin layers of 1 nm to 5 nm thickness ¹. During sputter deposition the fibers are kept in a rotating cage in order to avoid shadowing and to obtain uniform coatings. As the thickness of the sputtered copper layer is less than 1 μm , copper powder must be added for the copper matrix to be free of pores after hot pressing.

¹The tradeoff for improved interface properties due to adhesion promoters is a possible reduction of matrix conductivity.

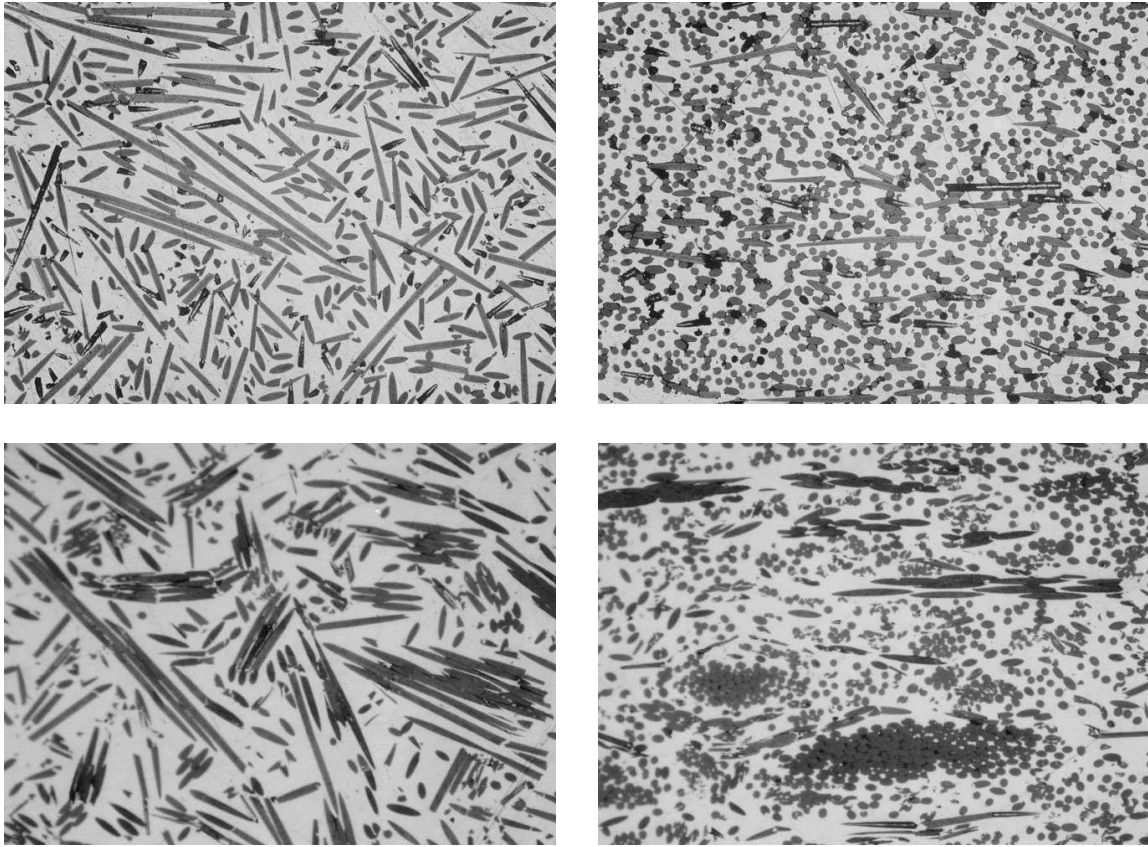


Figure 3.2: Two sets of corresponding metallographical sections of carbon-copper composites with differently sized aggregates. Sections normal to the direction of compression (left) and sections parallel to the direction of compression (right). ?

3.2 Fiber Arrangements, Aggregates, Aspect Ratio Distributions

Due to the unidirectional compression mode the fibers show planar random orientation distributions with little out-of-plane deviation (Fig. 3.2). As a consequence transversally isotropic material symmetries of the composite result.

The investigated composites have fiber volume fractions of up to 50%. Having in mind that the precoated fibers have an aspect ratio of around 40–70 one must realize that tightly packed arrangements of planar randomly distributed fibers cannot exist. Two main mechanisms can be elaborated which govern the emergence of the microstructures of the composites.

The first mechanism is that fibers tend to align in course of compression, forming aggregates

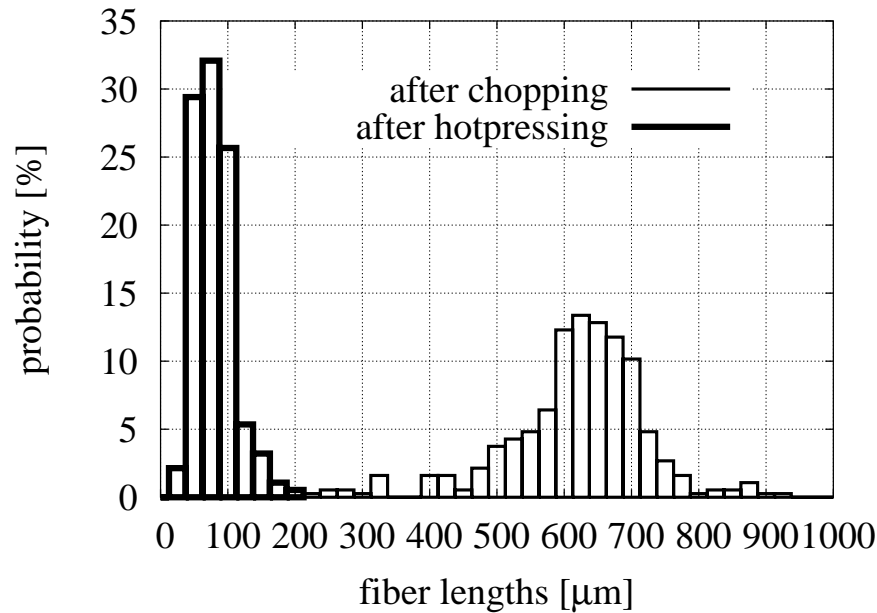


Figure 3.3: Fiber length distributions of electrochemically coated fibers and a hot pressed carbon pitch fiber–copper composite with a fiber volume fraction of 39%. The average fiber length before hot pressing is 600 μm , after hot pressing it is 67 μm ?.

? of locally aligned fibers of very high local fiber volume fractions. Figure 3.2 shows the metallographical sections of two Cu–C composites. The sections in the upper row show homogeneously distributed fibers as desired, even though some tendencies to form aggregates can be spotted. For the composite depicted in the bottom row of Fig. 3.2 large aggregates can be observed, which may lead to poor effective conductivities.

The second mechanism is that fibers break in the course of compression. Multi-modal fiber lengths allow for much higher volume fractions than can be attained with fibers of fixed size. Fibers of small aspect ratio are able to squeeze in and fill matrix “pockets”. In Fig. 3.3 the aspect ratio distributions of the fibers before hot pressing and after hot pressing are shown. Buchgraber ? states that the fiber aspect ratio distribution in the actual composite is independent of the aspect ratio distribution of the chopped fibers. Note that the investigated hot pressed carbon–copper composite shows inclusion–matrix topology, i.e. fibers do not touch each other due to the copper coatings.

3.3 Material Properties

All material data is given with respect to room temperature. No temperature dependence of the conductivities and interfacial resistances is taken into account.

3.3.1 The Carbon Fibers

The numerical investigations relate to pitch-based carbon fibers which exhibit excellent axial thermal conductivities (up to 1100 W/mK) and low CTEs. From this point of view these fibers are ideal for heat sink applications. Their main disadvantage is the high cost of production due to the high temperatures needed for graphitization (3000°C).

The reason for the high thermal conductivities in fiber direction of pitch fibers is the ordered structure of graphite. A well defined hexagonal network is created during melt spinning as the graphite orients under tension and is further refined during carbonization and graphitization. The highly ordered graphite forms planar networks which are stacked on top of each other (Fig. 3.4, left). These planes are wrinkled and oriented parallel to the fiber axis forming different microstructures such as radial or onion layer arrangements (Fig. 3.4, right) which influence the transversal conductivity of the fibers. According to Klett *et al.* the transversal conductivity of fibers with onion-like layer arrangement is smaller than that of fibers with radially arranged layers.

The conductivity in the transverse direction of pitch carbon fibers is usually much lower than the axial conductivity. Reported data for the transverse conductivities range from 1/100–1/10 of the axial conductivity.

Two sets of transversally isotropic material data for the carbon fibers are employed as reference data for the present study (Table 3.1).

Table 3.1: Heat conduction properties of the carbon pitch fibers at room temperature (transversal isotropic data).

T	$K_{11}^{(C)}$	$K_{22}^{(C)} = K_{33}^{(C)}$
[°C]	[W/mK]	[W/mK]
20	1000	10
20	1000	100

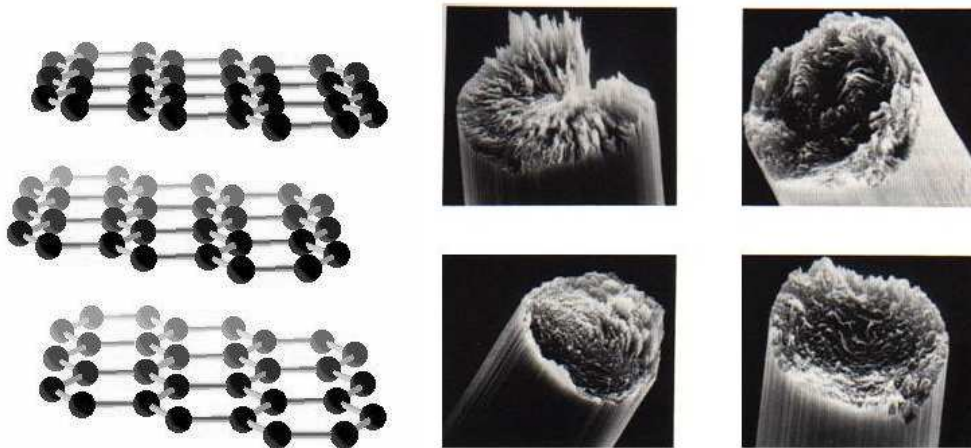


Figure 3.4: Densely packed graphite layers (left). Different morphologies of carbon pitch fibers. From the top left, clockwise: radial, random, quasi-onion-skin, onion ? (right).

3.3.2 The Copper Matrix

Copper is well suited for heat sink applications due to its high conductivity. A few aspects of this metal are discussed with respect to its application in MMCs in general and carbon reinforcements in particular. For more details and extensive lists of references see ?.

Copper is a rather noble metal and it does not suffer from corrosion which plagues aluminum. Another advantage of copper over aluminum (and magnesium) in MMC applications is its non-reactivity with carbon, i.e. possible composite microstructural degradation by interfacial reactions (aluminum carbide in the case of Al/C) is prevented. However, the wetting of liquid metals on carbon substrates is typically poor ? and considerable effort is required for a good interfacial bonding between carbon fibers and copper (see Production Routes, Section 3.1).

Due to the relatively high melting point of copper (1083°C) the fabrication of copper matrix composites is commonly done by powder metallurgy.

Compared to other metals, pure copper has a very high conductivity of around 400 W/mK. However, the conductivity of copper is significantly reduced by impurities such as oxygen and other contaminants ?. Almost all numerical investigations in the present work are based on a matrix conductivity of 360 W/mK (Table 3.2). Supplementary studies are carried out where variations of the matrix conductivity and its influence on the effective overall conductivity are investigated (see Section 8.3).

Table 3.2: Heat conduction properties of copper at room temperature (isotropic data).

T	$K^{(\text{Cu})}$
[°C]	[W/mK]
20	360

3.4 Interfacial Thermal Barriers

The presence of interfacial thermal resistances can severely reduce the effective heat flow passing through the interface. In the context of heat sink materials this mechanism takes effect on a microscopic level, as the heat interchange between matrix and fibers is impeded and full advantage cannot be taken of high fiber conductivities. On a macroscopic level, the heat transfer between components is reduced too, by these effects, which, however is not covered in the present work.

An interfacial thermal resistance is characterized by the *skin constant* or *interface parameter* β which is given in the units of W/m²K. One contribution can be thought of as a thermal contact resistance β_c due to poor mechanical and chemical bonding, due to the presence of impurities at the interface, or due to debonded regions. But even if materials with different conduction mechanisms are in perfect mechanical contact, some scattering of phonons, which are the principal carriers of heat, takes place and thus results in a thermal interface barrier ?. The latter contribution is referred to as a thermal boundary resistance β_b , also known as Kapitza resistance. In the present work the interface parameter, β , refers to the combined effects of both thermal contact resistance and thermal boundary resistances, i.e. $\beta = \beta_c + \beta_b$. In the literature the thermal interface resistance is referred to as LC type interface (low conductivity) ?. It is beyond the scope of this work to detail the physical background of thermal resistances. For more details and an extensive list of references the reader is referred to Swartz and Pohl ?. The mathematical implementation and description of interfacial thermal resistances is deferred to subsequent chapters.

3.4.1 The Carbon-Copper Interface

Copper and carbon are very different with respect to their heat conduction mechanisms. In copper heat is transported by electrons, while in carbon in the form of graphite, the main conduction mechanism are lattice vibrations (phonons) with conduction by electrons

Table 3.3: Measured interfacial resistances for electrochemically deposited copper coatings, β^{ec} , and sputtered copper with an Ti adhesion promoter, β^{sp} ??.

T	β^{ec}	β^{sp}
[°C]	[W/m ² K]	[W/m ² K]
20	0.13×10^6	1.33×10^6

playing a secondary role ².

A photothermal method ? was employed by Neubauer *et al.* ? to estimate the thermal contact resistance between carbon and copper. The actual measurements were carried out on flat, copper coated carbon substrates. Amorphous, isotropic glassy carbon was chosen due to its smooth surface in order to decrease surface roughness effects. In Table 3.3 the results are listed for electrochemically deposited copper coatings, β^{ec} , as well as sputtered copper coatings, that use a thin Ti layer as an adhesion promoter, β^{sp} ??.

Note that the measured thermal resistances apply to amorphous carbon, and not necessarily to pitch carbon fibers.

Due to different morphologies of the end faces and the cylindrical surfaces (side faces) of carbon fibers there may be different β -values there. Additionally fibers may show locally differing values of β . Furthermore, variations may be caused by the breaking of carbon fibers during hot pressing of the precoated fibers, which leaves coated side faces and non-coated end faces, so that high risk and low risk regions of potential interface degradation are present. At such regions the actual interfacial resistances differ from the measured interfacial resistances (Table 3.3). It is one aim of the present work to determine effects of different interfacial configurations on the effective conductivity of carbon-copper composites. Accordingly, based on the assumption of either perfect interfaces or imperfect interfaces, the latter being characterized by β^{sp} and β^{ec} , in combination with a possible failure of the end faces interface due to breaking of the carbon fibers, six combinations of different interfacial resistances at fiber ends and side faces are obtained, which are listed in Table 3.4 and each of which is considered in the present work.

²Carbon in the form of diamond has no free electrons and therefore is an electrical insulator. Heat is transported entirely by phonons.

Table 3.4: Investigated scenarios of non-ideal interfacial conduction.

case	β^{end}	β^{side}
	[W/m ² K]	[W/m ² K]
<i>C1</i>	∞	∞
<i>C2</i>	0	∞
<i>C3</i>	0.13×10^6	0.13×10^6
<i>C4</i>	0	0.13×10^6
<i>C5</i>	1.33×10^6	1.33×10^6
<i>C6</i>	0	1.33×10^6

Chapter 4

Micromechanical Methods

In this chapter the Mori–Tanaka method and the unit cell approach, the two modeling tools mainly utilized in this work, are discussed. Beforehand the basic laws and definitions of heat conduction are recalled and the range of applicability of the presented homogenization tools is discussed.

4.1 Heat Conduction in Homogeneous Solids

The mathematical description of heat flow at the continuum level is based on two fundamental sets of equations.

The first of them describes the conservation of energy. The enthalpy density balance for a control volume dV of a homogeneous solid can be given as

$$\gamma c_p T_{,t} = -q_{i,i} + g \quad . \quad (4.1)$$

The left hand side of Eq. (4.1) is the rate of change of the energy density stored within the control volume dV , with γ being the density and c_p the specific heat, both of which are assumed to be independent of time t and temperature T in the following. The right hand side of Eq. (4.1) describes the rate of heat entering V through its bounding surfaces, $q_{i,i}$, and the rate of heat generation g in V . The divergence of the heat flux field, $q_{i,i}$, indicates whether heat flows into the volume, $q_{i,i} < 0$, or out of the volume, $q_{i,i} > 0$. The term g is given in W/m^3 and may be due to nuclear, electrical, chemical, or magnetic sources.

The second governing equation is an empirical constitutive law which relates the flux

field q_i in a homogeneous solid to the temperature gradient field $T_{,i}$ according to

$$q_i = -K_{ij} T_{,j} \quad , \quad (4.2)$$

where K_{ij} is the second rank symmetric conductivity tensor of a homogeneous solid. Note that unless stated otherwise, summation is taken from 1 to 3 if a suffix occurs twice in any term. A suffix following a comma denotes differentiation with respect to x_i . Equation (4.2) is known as Fourier's law of heat conduction (analogous to Fick's law of diffusion). Rearranging Eq. (4.2) gives

$$T_{,i} = -R_{ij} q_j \quad , \quad (4.3)$$

with R_{ij} being the second rank, symmetric resistivity tensor of a homogeneous solid. The conductivity tensor and resistivity tensor are each others' inverses,

$$K_{ik} R_{kj} = \delta_{ij} \quad , \quad (4.4)$$

where δ_{ij} is the Kronecker Delta ($\delta_{ij} = 0$ for $i \neq j$ and $\delta_{ij} = 1$ for $i = j$). Note that in general for the tensor components $K_{ij} \neq 1/R_{ij}$ holds. Note also that in the case of anisotropic conductivities the flux and the gradient do not have the same direction in general.

Substituting $q_{i,i}$ in Eq. (4.1) by Eq. (4.2) yields

$$\gamma c_p T_{,t} = [K_{ij} T_{,j}]_{,i} + g \quad , \quad (4.5)$$

the differential equation of heat conduction for a stationary, homogeneous solid with heat generation within the solid.

From Eq. (4.5) a few special cases can be derived. In the absence of heat sources Eq. (4.5) reduces to

$$T_{,t} = [\alpha_{ij} T_{,j}]_{,i} \quad , \quad (4.6)$$

where α_{ij} is the thermal diffusivity tensor of the homogeneous solid which is defined as $\alpha_{ij} = K_{ij}/(\gamma c_p)$. Note that in the case of uniform conductivities¹ Eq. (4.6) reduces to the Fourier equation,

$$T_{,t} = \alpha_{ij} [T_{,j}]_{,i} \quad . \quad (4.7)$$

For steady state conditions the time dependent term vanishes and two important cases

¹A uniform conductivity implies $K_{ij} \neq K_{ij}(\vec{x})$ and $K_{ij} \neq K_{ij}(T)$.

can be obtained from Eq. (4.5), again assuming uniform conductivities. Allowing heat generation within the homogeneous solid yields

$$K_{ij} [T_{,j}]_{,i} + g = 0 \quad , \quad (4.8)$$

which is Poisson's equation. Assuming that there is no heat generation, $g = 0$, the Laplace equation is obtained,

$$[T_{,i}]_{,i} = 0 \quad , \quad (4.9)$$

which is equivalent to $q_{i,i} = 0$.

4.1.1 Applicability of the Utilized Methods

The micromechanical methods as employed in this work are used under the assumption that the Laplace equation is satisfied in each constituent of the investigated heterogeneous medium, implying steady state conditions, no source term, and *locally* uniform phase conductivities². For every point \vec{x} of the investigated heterogeneous material the equations

$$q_{i,i}(\vec{x}) = 0 \quad \text{and} \quad q_i(\vec{x}) = -K_{ij}(\vec{x}) T_{,j}(\vec{x}) \quad (4.10)$$

hold, governing the temperature field $T(\vec{x})$. Under these premises within the framework of the presented methods the fluctuating conductivity tensors $K_{ij}(\vec{x})$ and resistivity tensors $R_{ij}(\vec{x})$ of a composite material can be replaced by position independent, energetically equivalent effective conductivities $K_{ij}^{(*)}$ and resistivities $R_{ij}^{(*)}$, respectively. The effective properties link the homogenized temperature gradient field, $T_{,i}^{(*)}$, and flux field, $q_i^{(*)}$, Eqs. (2.1) and (2.2), respectively, according to Fourier's law (Eqs. (4.2) and (4.3)),

$$q_i^{(*)} = -K_{ij}^{(*)} T_{,j}^{(*)} \quad \text{and} \quad T_{,i}^{(*)} = -R_{ij}^{(*)} q_j^{(*)} \quad . \quad (4.11)$$

The homogenized temperature field, $T^{(*)}$, satisfies Laplace equation (Eq. (4.9)).

4.1.2 Some Remarks

For steady state conditions and the absence of a source term but temperature dependent conductivities Eq. (4.5) can be rewritten as

$$[K_{ij} T_{,j}]_{,i} = K_{ij,i} T_{,j} + K_{ij} [T_{,j}]_{,i} = 0 \quad , \quad (4.12)$$

²Note that the periodic microfield approach can account for the presence of source terms as well as inhomogeneous phase conductivities, provided the distribution of the latter complies to the periodicity of the geometry and is temperature independent. Such conditions, however, are not accounted for in the present work.

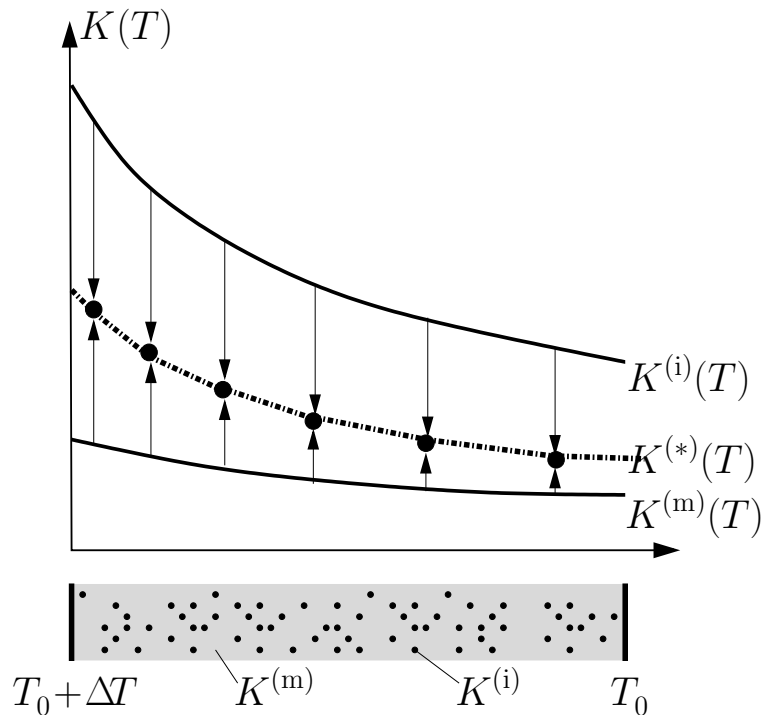


Figure 4.1: The effective conductivity of a composite, $K^{(*)}(T)$, consisting of constituents with temperature dependent conductivities ($K^{(m)}(T)$ and $K^{(i)}(T)$) can be estimated by a e.g. piecewise linear approximations of the conductivities.

which shows that temperature dependencies of the conductivity automatically introduce a position dependence via Eq. (4.12), which can have restrictions on the applicability of homogenization schemes as discussed in Section 2.2.

While temperature dependent conductivities can be accounted for without difficulties within the framework of embedding methods they cannot be captured exactly with the micromechanical approaches employed in this work, i.e. the Mori–Tanaka approach and the periodic microfield approach (compare also Section 4.3). However, it is good practice to evaluate effective conductivities for appropriate discrete temperatures based on fixed values of the constituents’ conductivities that conform to these temperatures (Fig. 4.1). One must be aware that such a procedure is an approximation. The RVE must satisfy the MICRO \ll MINI \ll MACRO principle, but its size must be such that accumulated variations of the conductivity due to macroscopic temperature gradients are small enough on the miniscale to be reasonably approximated as constant. Estimates of temperature dependent conductivities can then be used for steady state thermal analyses.

In the same way homogenized temperature dependent diffusivities, $\alpha_{ij}^{(*)}$, can be used for transient thermal analyses. In the context of microelectronic packaging applications transient analyses are necessary to assess the impact of peak loads or possible breakdowns of cooling. Again, the suggested homogenization approach is only applicable, if the micro-scale is sufficiently smaller than the miniscale being modeled³.

It shall further be pointed out that a piecewise linear approximation of the effective conductivity or diffusivity represents another source of inaccuracy. The latter, however, can be tuned as small as desired by increasing the number of discrete temperatures for which an estimate of the effective conductivity is obtained. Piecewise linear approximations and polynomial fits are typical standard applications for the FEM.

The outlined approach is related to some descriptions of the thermo-mechanical behavior of functionally graded materials (FGMs) which use layer-type approximations, with each layer being treated as a composite on its own ?.

³Transient investigations of unidirectionally reinforced composites in fiber direction could potentially yield unprecise estimates when homogenized behavior is used.

4.2 The Mori–Tanaka–Method

The Mori–Tanaka approximation is based on Eshelby’s equivalent inclusion formalism ? and dates back to the works of Brown and Stobbs ? and Mori and Tanaka ?. Since then it has been used to advantage for solving various thermo–mechanical problems related to composite material.

In this work the Mori–Tanaka interpretation as introduced by Benveniste ? is used. Benvenistes “direct” approach was originally proposed in the context of elasticity but is applicable to the case of conductivity ?? as well.

4.2.1 Approach and Assumptions

A Mori–Tanaka formalism for perfectly bonded constituents is derived. For the case of imperfect thermal interfaces a replacement operation must be invoked first, see Chapter 5, which allows to replace imperfectly bonded inclusions by perfectly bonded “replacement inclusions” of lower conductivity. The following derivation is based on averaged dilute concentration tensors. Accordingly, a procedure that allows to derive dilute concentration tensors for inclusions of arbitrary shapes will be detailed in Chapter 5. Note that the resulting formulas are not restricted to spheroidal inclusion geometries but apply to any type of inclusion the averaged dilute concentration tensor of which is known.

The derived formulas apply to $N + 1$ –phase composite materials, only perfectly bonded phases being considered. While the inclusion phases ($r = 1, 2, \dots, N$) may be transversally isotropic, the matrix phase ($r = 0$) is restricted to isotropic behavior. At this point the term *phase* must be defined. In this work an inclusion phase comprises inclusions of identical material properties and identical shape (i.e. identical dilute concentration tensors) but different orientations (in ? the term “inclusion family” is used). The statistical description of the orientation distribution of an inclusion phase is given by its orientation distribution function (ODF), $\rho^{(r)}$. The volume fraction of the r^{th} phase is $\xi^{(r)}$, the sum over all phases equalling

$$\sum_{r=0}^N \xi^{(r)} = 1 \quad . \quad (4.13)$$

Due to its dual structure the Mori–Tanaka method can be developed based on either applied uniform temperature gradients $T_{,i}^{(*)}$ or uniform flux fields $q_i^{(*)}$. Therefore separate equations are derived and given in a two–column style – the left hand side relating to the “temperature–gradient” domain yielding the effective conductivity and the right hand side

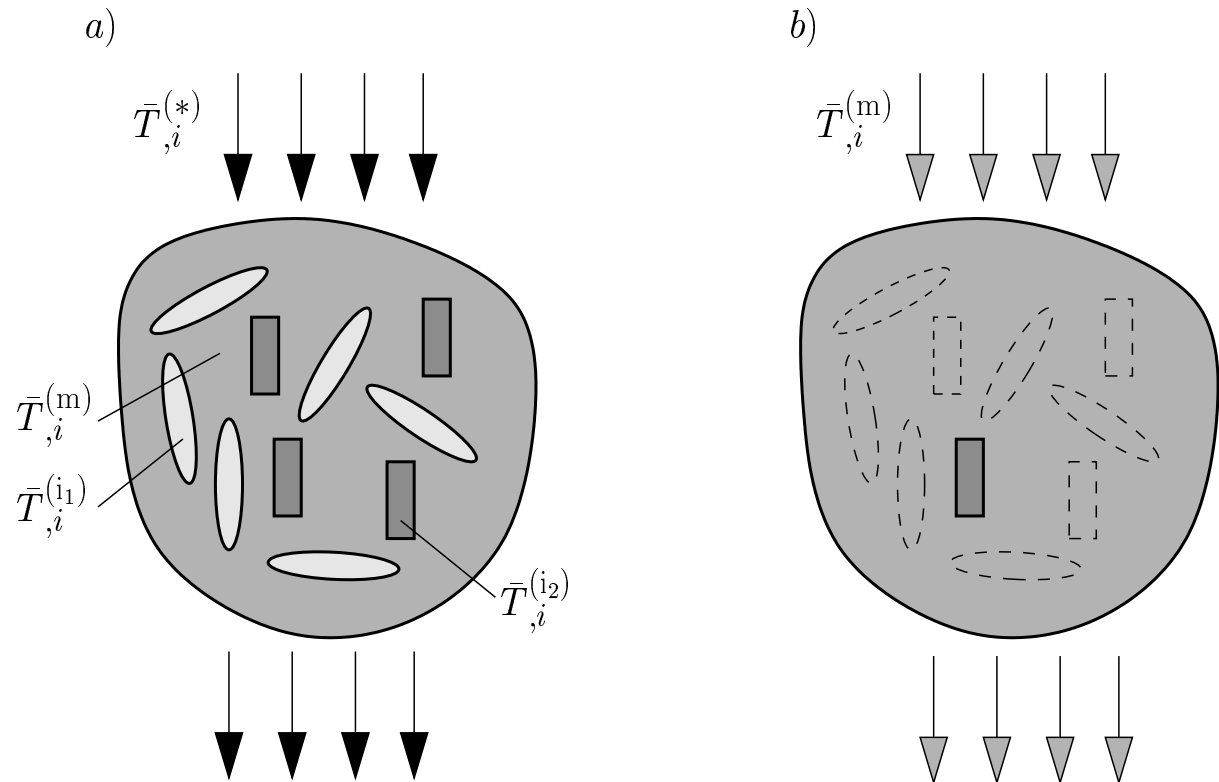


Figure 4.2: a) Within the framework of mean field approaches the temperature gradients and flux fields of the phases are approximated to be constant. b) Dilutely dispersed inclusions subjected to an effective matrix field, $\bar{T}_{,i}^{(m)}$, which differs from $\bar{T}_{,i}^{(*)}$ are modeled.

relating to the “flux” domain yielding the effective resistivity.

4.2.2 Effective Properties – Concentration Tensors

Mean Field Assumption

The Mori–Tanaka method hinges upon the mean field assumption. Within the framework of mean–field approaches only the phase averaged flux and temperature gradient fields are considered (Fig. 4.2a) in the case of heat conduction problems. Phase averaged gradient fields and flux fields with respect to the global coordinate system can be defined by means of orientational averaging as $\bar{T}_{,i}^{(r)} = \langle \mathcal{L} T_{,i}^{(r)} \rangle$ and $\bar{q}_i^{(r)} = \langle \mathcal{L} q_i^{(r)} \rangle$, respectively. The angular brackets designate orientational averaging, where the ODF is normalized to give $\langle \rho^{(r)} \rangle = 1$, and the additional superscript \mathcal{L} indicates that the tensors are given with respect to the

global coordinate system (Appendix A). The ODF, $\rho^{(r)}$, must not be a smooth function. In the case of discrete inclusion orientations the integral $\langle \cdot \rangle$ degenerates to a sum over the inclusion orientations. The corresponding ODF is then given by a set of Dirac-deltas.

The integral expression $\langle \cdot \rangle$ actually involves two steps of averaging carried out on two different levels. The phase averaged fields, $\bar{T}_{,i}^{(r)}$ and $\bar{q}_i^{(r)}$, are obtained by orientational averaging of single inclusion fields, $\angle T_{,i}^{(r)}$ and $\angle q_i^{(r)}$, which in turn are constant only in special cases and are approximated to be constant otherwise. Averaging of the dilute inclusion fields is necessary, if the inclusion shape is non-ellipsoidal or if interfacial resistances are present (compare chapter 5). The bars indicating the averaging process at the dilute level are omitted in the following, so there is no confusion with the level of averaging. Furthermore it must be noted that inclusion interaction effects and non-uniform matrix fields cause fluctuations within the fields of individual inclusions. These effects and their consideration are discussed in course of the derivation when appropriate.

From the definition of volume averaging one immediately obtains the following relations between the effective fields of the composite and the phase averaged fields

$$T_{,i}^{(*)} = \sum_{r=0}^N \xi^{(r)} \bar{T}_{,i}^{(r)} \qquad q_i^{(*)} = \sum_{r=0}^N \xi^{(r)} \bar{q}_i^{(r)} \quad (4.14)$$

$$= \xi^{(m)} \bar{T}_{,i}^{(m)} + \sum_{r=1}^N \xi^{(r)} \bar{T}_{,i}^{(r)} \qquad = \xi^{(m)} \bar{q}_i^{(m)} + \sum_{r=1}^N \xi^{(r)} \bar{q}_i^{(r)} \quad (4.15)$$

adopting the notation (m) for the matrix phase (0). Note again that the averaged temperature gradient and flux field are given with respect to the global coordinate system.

Fourier's law is employed to recast Eqs. (4.14) and (4.15) into the following form

$$K_{ij}^{(*)} T_{,j}^{(*)} = \sum_{r=0}^N \xi^{(r)} \left\langle \angle K_{ij}^{(r)} \angle T_{,j}^{(r)} \right\rangle \qquad R_{ij}^{(*)} q_j^{(*)} = \sum_{r=0}^N \xi^{(r)} \left\langle \angle R_{ij}^{(r)} \angle q_j^{(r)} \right\rangle \quad (4.16)$$

$$= \xi^{(m)} K_{ij}^{(m)} \bar{T}_{,j}^{(m)} + \sum_{r=1}^N \xi^{(r)} \left\langle \angle K_{ij}^{(r)} \angle T_{,j}^{(r)} \right\rangle \qquad = \xi^{(m)} R_{ij}^{(m)} \bar{q}_j^{(m)} + \sum_{r=1}^N \xi^{(r)} \left\langle \angle R_{ij}^{(r)} \angle q_j^{(r)} \right\rangle \quad (4.17)$$

If the inclusion conductivities/resistivities are isotropic, $\angle K_{ij}^{(r)}$ and $\angle R_{ij}^{(r)}$ are independent of the orientation and can be moved from in between the angular brackets, simplifying Eqs. (4.16) and (4.17) considerably.

The local averaged temperature gradient and averaged flux of inclusions of a given orientation and associated with the r^{th} phase can be formally linked to the corresponding

effective field by concentration tensors,

$$\langle T_{,i}^{(r)} \rangle = \langle D_{ij}^{(r)} T_{,j}^{(*)} \rangle \quad \langle q_i^{(r)} \rangle = \langle F_{ij}^{(r)} q_j^{(*)} \rangle \quad (4.18)$$

By means of orientational averaging phase averaged temperature gradient concentration tensors, $\bar{D}_{ij}^{(r)} = \langle \langle D_{ij}^{(r)} \rangle \rangle$, and flux concentration tensors, $\bar{F}_{ij}^{(r)} = \langle \langle F_{ij}^{(r)} \rangle \rangle$, are introduced which are defined such that they relate the phase averaged fields to macroscopic fields giving

$$\bar{T}_{,i}^{(r)} = \bar{D}_{ij}^{(r)} T_{,j}^{(*)} \quad \bar{q}_i^{(r)} = \bar{F}_{ij}^{(r)} q_j^{(*)} \quad (4.19)$$

with $r = 0, 1, \dots, N$. The concentration tensors must fulfill certain conditions, see e.g. ?? where a number of identities for the elastic case are listed. Volume weighted sums of the concentration tensors must equal the unit tensor, a fact used to advantage in the following derivations,

$$\sum_{r=0}^N \xi^{(r)} \bar{D}_{ij}^{(r)} = \delta_{ij} \quad \sum_{r=0}^N \xi^{(r)} \bar{F}_{ij}^{(r)} = \delta_{ij} \quad (4.20)$$

$$\xi^{(m)} \bar{D}_{ij}^{(m)} + \sum_{r=1}^N \xi^{(r)} \bar{D}_{ij}^{(r)} = \delta_{ij} \quad \xi^{(m)} \bar{F}_{ij}^{(m)} + \sum_{r=1}^N \xi^{(r)} \bar{F}_{ij}^{(r)} = \delta_{ij} \quad (4.21)$$

Using the identity in Eq. (4.21) together with the definition of the concentration tensors as given in Eq. (4.19) allows to rearrange Eqs. (4.16) and (4.17) so that the effective conductivity tensor and resistivity tensor is given in the following forms,

$$K_{ij}^{(*)} = \sum_{r=0}^N \xi^{(r)} \langle \langle K_{ik}^{(r)} \rangle \rangle \langle \langle D_{kj}^{(r)} \rangle \rangle \quad R_{ij}^{(*)} = \sum_{r=0}^N \xi^{(r)} \langle \langle R_{ik}^{(r)} \rangle \rangle \langle \langle F_{kj}^{(r)} \rangle \rangle \quad (4.22)$$

$$= \xi^{(m)} K_{ik}^{(m)} \bar{D}_{kj}^{(m)} + \sum_{r=1}^N \xi^{(r)} \langle \langle K_{ik}^{(r)} \rangle \rangle \langle \langle D_{kj}^{(r)} \rangle \rangle \quad = \xi^{(m)} R_{ik}^{(m)} \bar{F}_{kj}^{(m)} + \sum_{r=1}^N \xi^{(r)} \langle \langle R_{ik}^{(r)} \rangle \rangle \langle \langle F_{kj}^{(r)} \rangle \rangle \quad (4.23)$$

$$= K_{ij}^{(m)} + \sum_{r=1}^N \xi^{(r)} \langle \langle (K_{ik}^{(r)} - K_{ik}^{(m)}) \rangle \rangle \langle \langle D_{kj}^{(r)} \rangle \rangle \quad = R_{ij}^{(m)} + \sum_{r=1}^N \xi^{(r)} \langle \langle (R_{ik}^{(r)} - R_{ik}^{(m)}) \rangle \rangle \langle \langle F_{kj}^{(r)} \rangle \rangle \quad (4.24)$$

with Eq. (4.21) being used for transforming Eq. (4.23) to Eq. (4.24).

At this stage it is convenient to introduce “orientationally averaged conductivities”, $\hat{K}_{ij}^{(r)}$, and “orientationally averaged resistivities”, $\hat{R}_{ij}^{(r)}$, such that

$$\hat{K}_{ik}^{(r)} \bar{D}_{kj}^{(r)} = \langle \langle K_{ik}^{(r)} \rangle \rangle \langle \langle D_{kj}^{(r)} \rangle \rangle \quad \hat{R}_{ik}^{(r)} \bar{F}_{kj}^{(r)} = \langle \langle R_{ik}^{(r)} \rangle \rangle \langle \langle F_{kj}^{(r)} \rangle \rangle \quad (4.25)$$

is fulfilled. For the case of isotropic conductive properties obviously $\hat{K}_{ij}^{(r)} = K_{ij}^{(r)}$ and $\hat{R}_{ij}^{(r)} = R_{ij}^{(r)}$ holds, because in that case the conductivity tensor and the resistivity tensor are orientation independent and can be moved out of the integrals on the right hand side of Eq. (4.25). For anisotropic materials it can be shown that $\hat{K}_{ij}^{(r)}$ and $\hat{R}_{ij}^{(r)}$ are each others inverses, i.e. $\hat{K}_{ik}^{(r)} \hat{R}_{kj}^{(r)} = \delta_{ij}$. As can be seen from Eq. (4.25) the orientationally averaged material properties that are assigned to each inclusion family are chosen such that Eqs. (4.22)–(4.24) are considerably simplified and they formally coincide with the equations as given in ? for isotropic constituents,

$$K_{ij}^{(*)} = \sum_{r=0}^N \xi^{(r)} \hat{K}_{ik}^{(r)} \bar{D}_{kj}^{(r)} \quad R_{ij}^{(*)} = \sum_{r=0}^N \xi^{(r)} \hat{R}_{ik}^{(r)} \bar{F}_{kj}^{(r)} \quad (4.26)$$

Equations (4.22)–(4.24) have been derived by consistently applying the mean field idea and by introducing averaged phase concentration tensors (Eq. (4.19)). They allow for calculating the effective conductivities and resistivities of a composite if the corresponding concentration tensors are known. It is worth noting that if imperfect thermal interfaces are not treated on the dilute level the right hand sides of Eqs. (4.14) and (4.15) need to be extended ??.

Taking advantage of the identity in Eq. (4.20) the left hand side of Eqs. (4.22) can be multiplied with the volume weighted sum of the concentration tensors, which allows to recast Eqs. (4.22)–(4.24) into an equivalent but more symmetric form

$$\sum_{r=0}^N \xi^{(r)} \left\langle \left(K_{ik}^{(*)} - \langle K_{ik}^{(r)} \rangle \right) \langle D_{kj}^{(r)} \rangle \right\rangle = 0 \quad \sum_{r=0}^N \xi^{(r)} \left\langle \left(R_{ik}^{(*)} - \langle R_{ik}^{(r)} \rangle \right) \langle F_{kj}^{(r)} \rangle \right\rangle = 0 \quad (4.27)$$

Combining Eq. (4.19) and Fourier's law allows to link the temperature gradient and flux concentration tensors to the effective properties according to

$$\bar{D}_{ij}^{(m)} = R_{ik}^{(m)} \bar{F}_{kl}^{(m)} K_{lj}^{(*)} \quad \bar{F}_{ij}^{(m)} = K_{ik}^{(m)} \bar{D}_{kl}^{(m)} R_{lj}^{(*)} \quad (4.28)$$

$$\bar{D}_{ij}^{(r)} = \left\langle \langle R_{ik}^{(r)} \rangle \langle F_{kl}^{(r)} \rangle \right\rangle K_{lj}^{(*)} \quad \bar{F}_{ij}^{(r)} = \left\langle \langle K_{ik}^{(r)} \rangle \langle D_{kl}^{(r)} \rangle \right\rangle R_{lj}^{(*)} \quad (4.29)$$

These expressions hold for any type of mean field based concentration tensors. Equation (4.29) can be used to determine averaged dilute flux concentration tensors based on dilute averaged temperature gradient concentration tensors by replacing $\bar{R}_{ij}^{(*)}$ with $R_{ij}^{(m)}$.

The problem of finding effective properties has been shifted to that of finding appropriate concentration tensors.

Idea of the Effective Field

For inclusion volume fractions of less than a few percent where neighboring inclusions do not “feel each other” the concentration tensors may be obtained from single inclusion problems, see Chapter 5. Corresponding to each phase a representative solitary inclusion embedded in a matrix material of infinite extent is considered and its *dilute* temperature gradient concentration tensor, ${}^0D_{ij}^{(i)}$, or *dilute* flux concentration tensor, ${}^0F_{ij}^{(i)}$, are evaluated. The superscript 0 denotes the dilute volume fractions. Note that the dilute concentration tensors refer to inclusion fields which are inhomogeneous in general⁴. Bars indicating the volume averaging process of the inclusion temperature gradient field and flux field on the dilute level are omitted in this chapter in order to avoid confusion with orientational averaged quantities.

For volume fractions of more than a few percent inclusion interaction must explicitly be accounted for. One way for achieving this consists of approximating the temperature gradient or flux field acting on an inclusion by an appropriate averaged matrix temperature gradient or flux field. This may be viewed as a perturbation field superimposed on the applied far field temperature gradient or flux. In the context of elasticity this idea of combining the concept of an average matrix stress with Eshelby–type equivalent inclusion approaches goes back to Brown and Stobbs ? and Mori and Tanaka ?.

Based on ? the determination of the concentration tensors is based on the solution of an auxiliary problem. The core assumption is that the inclusions are not subjected to the applied external field but to an appropriate matrix field, the *effective field*, which is initially unknown. The effective matrix field differs from that of the composite due to the presence of all inclusions (Fig. 4.2b). This core assumption can be written as

$$\bar{T}_{,i}^{(r)} = {}^0\bar{D}_{ij}^{(r)} \bar{T}_{,j}^{(m)} \qquad \bar{q}_i^{(r)} = {}^0\bar{F}_{ij}^{(r)} \bar{q}_j^{(m)} \qquad (4.30)$$

with $r = 1, 2, \dots, N$ for each inclusion phase. In Eq. (4.30) averaged dilute temperature gradient concentration tensors ${}^0\bar{D}_{ij}^{(r)}$ and the dilute flux concentration tensors ${}^0\bar{F}_{ij}^{(r)}$ have been introduced which are evaluated by means of orientational averaging as

$${}^0\bar{D}_{ij}^{(r)} = \left\langle \angle {}^0D_{ij}^{(r)} \right\rangle \qquad {}^0\bar{F}_{ij}^{(r)} = \left\langle \angle {}^0F_{ij}^{(r)} \right\rangle \qquad (4.31)$$

for each inclusion phase. Naturally the dilute matrix concentration tensors ${}^0D_{ij}^{(m)}$ and ${}^0F_{ij}^{(m)}$ approach the unit tensor which can also be seen directly from Eq. (4.21) with $\xi^{(r)} \rightarrow 0$

⁴Only for the special case of perfectly bonded dilute ellipsoids will the inclusion fields be uniform for uniform far field gradients, see Chapter 5

($r = 1, 2, \dots, N$) and $\bar{D}_{ij}^{(m)}$ and $\bar{F}_{ij}^{(m)}$ degenerating to ${}^0D_{ij}^{(m)} = \delta_{ij}$ and ${}^0F_{ij}^{(m)} = \delta_{ij}$, respectively, due to the absence of inclusions.

The phase averaged inclusion fields in Eq. (4.15) can be replaced by the relations given in Eq. (4.30), yielding

$$T_{,i}^{(*)} = \xi^{(m)} \bar{T}_{,i}^{(m)} + \sum_{r=1}^N \xi^{(r)} {}^0\bar{D}_{ij}^{(r)} \bar{T}_{,j}^{(m)} \quad q_i^{(*)} = \xi^{(m)} \bar{q}_i^{(m)} + \sum_{r=0}^N \xi^{(r)} {}^0F_{ij}^{(r)} \bar{q}_j^{(m)} \quad (4.32)$$

$$= \left[\xi^{(m)} \delta_{ij} + \sum_{r=1}^N \xi^{(r)} {}^0\bar{D}_{ij}^{(r)} \right] \bar{T}_{,j}^{(m)} \quad = \left[\xi^{(m)} \delta_{ij} + \sum_{r=1}^N \xi^{(r)} {}^0\bar{F}_{ij}^{(r)} \right] \bar{q}_j^{(m)} \quad (4.33)$$

From comparing Eq. (4.33) with the definition of the concentration tensors Eq. (4.19) one immediately obtains the Mori–Tanaka concentration tensors as

$${}^{\text{MT}}\bar{D}_{ij}^{(m)} = \left[\xi^{(m)} \delta_{ij} + \sum_{r=1}^N \xi^{(r)} {}^0\bar{D}_{ij}^{(r)} \right]^{-1} \quad {}^{\text{MT}}\bar{F}_{ij}^{(m)} = \left[\xi^{(m)} \delta_{ij} + \sum_{r=1}^N \xi^{(r)} {}^0\bar{F}_{ij}^{(r)} \right]^{-1} \quad (4.34)$$

for the matrix phase, by using Eq. (4.30) and Eq. (4.34) the concentration tensors for the r^{th} inclusion phase then follows as

$${}^{\text{MT}}\bar{D}_{ij}^{(r)} = {}^0\bar{D}_{ik}^{(r)} {}^{\text{MT}}\bar{D}_{kj}^{(m)} \quad {}^{\text{MT}}\bar{F}_{ij}^{(r)} = {}^0\bar{F}_{ik}^{(r)} {}^{\text{MT}}\bar{F}_{kj}^{(m)} \quad (4.35)$$

Note that in case of isotropic inclusion materials the effective conductivity and resistivity can be readily determined with Eqs. (4.22)–(4.24) and the phase averaged concentration tensors (Eqs. (4.34)–(4.35)). In the case of inclusion families with nonaligned inclusions the only integral remaining to be solved is the one given in Eq. (4.31). Inclusion families of aligned inclusions do not require orientational averaging, the respective concentration tensors must only be transformed to the global coordinate system. In case of orthotropic phases, however, either $\hat{K}_{ij}^{(r)}$ and $\hat{R}_{ij}^{(r)}$ need to be evaluated or the concentration tensor for a given orientation with respect to the global coordinate system

$$\angle {}^{\text{MT}}D_{ij}^{(r)} = \angle {}^0D_{ik}^{(r)} {}^{\text{MT}}\bar{D}_{kj}^{(m)} \quad \angle {}^{\text{MT}}F_{ij}^{(r)} = \angle {}^0F_{ik}^{(r)} {}^{\text{MT}}\bar{F}_{kj}^{(m)} \quad (4.36)$$

must be evaluated for each possible orientation as demanded in Eqs. (4.22)–(4.24).

Finally, it can be proven that within the presented framework the effective conductivity and resistivity are the inverses of each other. First Eq. (4.23) is multiplied with inverses of ${}^{\text{MT}}\bar{D}_{ij}^{(m)}$ and ${}^{\text{MT}}\bar{F}_{ij}^{(m)}$, respectively. For the left hand sides the Mori–Tanaka matrix concentration tensors are expressed by Eq. (4.34). For the right hand sides, Eq. (4.35) is

used to introduce dilute inclusion phase concentration tensors, ${}^0\bar{D}_{ij}^{(r)}$ and ${}^0\bar{F}_{ij}^{(r)}$. Following relationships are then obtained

$$K_{ik}^{(*)} \left[\xi^{(m)} \delta_{kj} + \sum_{r=1}^N \xi^{(r)} \left\langle \angle^0 D_{kj}^{(r)} \right\rangle \right] = \xi^{(m)} K_{ij}^{(m)} + \sum_{r=1}^N \xi^{(r)} \left\langle \angle K_{ik}^{(r)} \angle^0 D_{kj}^{(r)} \right\rangle, \quad (4.37)$$

$$R_{ik}^{(*)} \left[\xi^{(m)} \delta_{kj} + \sum_{r=1}^N \xi^{(r)} \left\langle \angle^0 F_{kj}^{(r)} \right\rangle \right] = \xi^{(m)} R_{ij}^{(m)} + \sum_{r=1}^N \xi^{(r)} \left\langle \angle R_{ik}^{(r)} \angle^0 F_{kj}^{(r)} \right\rangle. \quad (4.38)$$

Now Eq. (4.29) is applied for the dilute case, i.e. $\bar{R}_{ij}^{(*)} \rightarrow R_{ij}^{(m)}$, and substituted for ${}^0F_{ij}^{(r)}$ in Eq. (4.38). The isotropic matrix resistivity can be moved out of the integral giving an equivalent to Eq. (4.38) in the following form

$$R_{ik}^{(*)} \left[\xi^{(m)} \delta_{kj} + \sum_{r=1}^N \xi^{(r)} \left\langle \angle K_{kl}^{(r)} \angle^0 D_{lm}^{(r)} \right\rangle R_{mj}^{(m)} \right] = \xi^{(m)} R_{ij}^{(m)} + \sum_{r=1}^N \xi^{(r)} \left\langle \angle^0 D_{mn}^{(r)} \right\rangle R_{nj}^{(m)} \quad (4.39)$$

and multiplying Eq. (4.39) with the matrix conductivity finally yields

$$R_{ik}^{(*)} \left[\xi^{(m)} K_{kj}^{(m)} + \sum_{r=1}^N \xi^{(r)} \left\langle \angle K_{kl}^{(r)} \angle^0 D_{lj}^{(r)} \right\rangle \right] = \xi^{(m)} \delta_{ij} + \sum_{r=1}^N \xi^{(r)} \left\langle \angle^0 D_{ij}^{(r)} \right\rangle \quad (4.40)$$

By comparing Eq. (4.40) with Eq. (4.37) one immediately realizes that the effective conductivity and resistivity are indeed each others inverse.

4.2.3 Some Remarks

Localization

Phase averaged concentration tensors as given in Eqs. (4.34) and (4.35) can be used to advantage for estimating the effective conductivity and resistivity of composites with non-aligned inclusions (Eqs. (4.22–4.24)). From Eq. (4.19) the capability of “zooming in” on the phase averaged fields is evident, allowing to determine the averaged local response of the phases due to some known macroscopic thermal load. For composites with inclusion families conforming to some non-aligned ODF the phase averaged values, however, are of limited practical value for assessing the local fields of single individual inclusions. More insight can be obtained by evaluating the temperature gradient and flux field of a given inclusion by using an equivalent to Eq. (4.30) which can be written in the form

$$\angle T_{,i}^{(r)} = \angle^0 D_{ij}^{(r)} \bar{T}_{,j}^{(m)} \quad \angle q_i^{(r)} = \angle^0 F_{ij}^{(r)} \bar{q}_j^{(m)} \quad (4.41)$$

Note again that dilute concentration tensors are determined from single inclusion problems and hence they might represent averaged quantities.

Equation (4.41) also provides the capability for estimating the temperature gradients and flux fields of inclusions that do not conform to the shape, orientation or conductive properties of any of the inclusion families which “build up” the averaged matrix fields due to applied thermal loads. Such inclusions can be thought of as “measuring instruments” and can be used to estimate the micro-field response of an inclusion for a given matrix field as a function of the shape, material properties and orientation. Due to their extremely small volume fractions (“ghost inclusions”) they do not contribute to the average matrix field. All that has to be done for evaluating their microfield response is to insert appropriate dilute concentration tensors ${}^0D_{ij}^{(r)\angle}$ and ${}^0F_{ij}^{(r)\angle}$ into Eq. (4.41) once the averaged matrix temperature gradient field, $\bar{T}_i^{(m)}$, and averaged matrix flux field, $\bar{q}_i^{(m)}$, have been evaluated. The concept of ghost inclusions can also be utilized in the case of elasticity ?. The resulting stress and strain fields in individual inclusions due to applied thermomechanical loads are of great practical value for assessing the load states of reinforcements with respect to fiber-fracture.

Limitations

Diagonal Symmetry It was shown by Benveniste, Dvorak and Chen ? that the Mori-Tanaka method yields unsymmetric elasticity tensors for many multiphase systems involving aligned inclusions of different shape and material properties. The derived Mori-Tanaka multiphase formulation for heat conduction as developed above, however, will always give symmetric effective conductivities and resistivities for aligned inclusions as only diagonal tensors are involved.

However, unsymmetric effective conductivities/resistivities are obtained for composites consisting of three or more phases, if at least two differently oriented inclusion phases are present which have different dilute concentration tensors ${}^0\bar{D}_{ij}^{(r)5}$.

Microgeometry For all volume fractions the Mori-Tanaka theory can be related to a distinct matrix-inclusion topology which may be viewed as a generalization of the microgeometry derived from Hashin’s composite sphere assemblage ? and composite cylinder assemblage ? as shown by Ponte Castañeda and Willis ?. In the case of “standard” Mori-

⁵Note that both inclusion concentration tensors must be “transversally isotropic”, i.e. in case of spherical inclusions, the respective conductivity must be transversally isotropic.

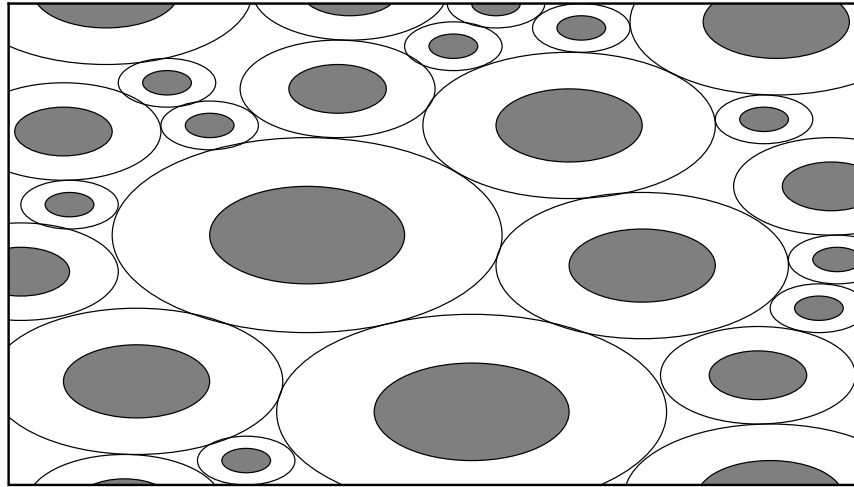


Figure 4.3: Ellipsoidal inclusions in ellipsoidally distributed spatial arrangement ($a_2/a_1 = 2$) as described by standard Mori–Tanaka–type approaches; after [?], figure modified from [?].

Tanaka methods which describe aligned inclusions, space is tightly packed with composite ellipsoids of constant aspect ratio but different size. The core of these ellipsoids consists of the inclusion material on which a layer of matrix material is placed to meet the volume fraction requirement (Fig. 4.3). The two ellipsoids which bound the matrix are aligned and have the same aspect ratio. Note that for the case of nonaligned inclusions the generalized Hashin–Shtrikman framework is violated by Mori–Tanaka estimates which then take on a more approximative character [?]. A microstructure based on randomly distributed inclusions has recently been discussed by Hu and Weng [?].

As in other micromechanical methods there is no intrinsic length scale in Mori–Tanaka methods, i.e. inclusion size effects can not be captured.

As each inclusion is completely surrounded by matrix material they cannot touch each other. Therefore the model fails to predict the physical properties of a composite around the percolation threshold inclusion volume fraction [??], where there exists a sudden change in the physical properties of e.g. the electrical conductivity of a conductor–insulator composite.

As is evident from the derivation of the concentration tensors inclusion interaction effects are accounted for only via the effective field with each inclusion “feeling all other inclusions in an averaged way”. Intra–inclusion fluctuations of the fields, by definition, cannot be handled by MFAs.

The Mori–Tanaka Method in Relation to other MFAs

Mori–Tanaka estimates for a composite containing spherical isotropic inclusions will always coincide with the HS upper bound (Eqs. (2.11)) if the matrix is the most resistive phase and with the HS lower bound (Eqs. (2.10)) if the matrix is the most conductive phase. If the matrix is neither the most resistive nor the most conductive phase, Mori–Tanaka conductivities with aligned spherical inclusions (not necessarily isotropic) will always lie within the HS bounds ?. It is also pointed out in ? that multiphase Mori–Tanaka estimates of aligned thin discs and aligned circular continuous fibers coincide with the appropriate HS bounds. Otherwise the effective conductivity will lie within the HS bounds.

Mori–Tanaka schemes are explicit schemes, i.e. in contrast to self consistent schemes no iterations are necessary for obtaining estimates of the effective conductivities. Another computational disadvantage of self consistent schemes compared to Mori–Tanaka schemes are possibly anisotropic effective conductivities, which require special treatment of the dilute inclusion concentration tensors (see Withers ? and Gavazzi and Lagoudas ? for specific analytical and general numerical solutions in the context of elasticity, respectively). As a tradeoff for high computational cost compared to Mori–Tanaka estimates self consistent schemes do not yield unsymmetric effective properties ?.

Further discussion of the Mori–Tanaka method can be found in ?? in the context of elastic two–phase materials, fundamental observations can be immediately transferred to the case of conductivity.

Methods Related to Mori–Tanaka Schemes

Analogous to Eshelby’s idea in elasticity an equivalent inclusion method for steady state heat conduction was introduced by Hatta and Taya ?? for aligned fibers as well as misoriented short fiber composites. In analogy to Eshelby’s eigenstrains they introduced “eigen thermal gradients” via uniform doublet distributions inside spheroidal inclusions. Inclusion interaction is accounted for by means of an averaged disturbance of the temperature gradient field, their assumptions being equivalent to those in ? in the context of elasticity. Their equivalent inclusion approach also proved to be highly successful for describing the effective conductivity of coated fiber composites ?.

The concept of introducing an average disturbance of the temperature gradient field is very

much akin to the concept of “back-stresses”, which is applied to the computation of the effective conductivity in ?.

Nomenclature

The equations derived in this section give a general framework for Mori–Tanaka methods for perfectly bonded constituents. It is shown that imperfect thermal interfaces can be accounted for by replacing single inclusions with interfacial thermal resistances with less conductive but perfectly bonded replacement inclusions (see Chapter 5).

This procedure, which can be combined with Mori–Tanaka methods or other mean field approaches, constitutes a major advance in the modeling of the thermophysical behavior of composite materials.

In addition to the idea of merging inclusion conductivities and interfacial resistances into reduced conductivities, the Mori–Tanaka theory is used in a more generalized sense in this work from the viewpoint of ODFs and inclusion shapes, as well.

In the literature on the thermophysical and thermomechanical behavior of composite materials the most frequent use of Mori–Tanaka methods have been studies of microgeometries of aligned spheroidal inclusions as shown in Fig. 4.3. Such applications are referred to as “standard MTM” in the following. There is also a considerable number of reports on the use of Mori–Tanaka approaches for composites with nonaligned spheroidal reinforcements, the orientations of which are described by ODFs, a number of schemes being used to carry out the orientational averaging ?. Such extended Mori–Tanaka schemes are subject to a number of limitations as discussed above. Both standard and extended Mori–Tanaka methods use thermal Eshelby tensors and are denoted as E–MT in this work.

In the present work a hybrid approach is introduced that uses numerically evaluated dilute temperature gradient concentration tensors, ${}^0D_{ij}^{(i)}$, and does not restrict the Mori–Tanaka method to ellipsoidal inclusion shapes. Such descriptions are referred to as a hybrid Mori–Tanaka method, H–MT, and are used with cylindrical fibers in Chapters 7 and 8.

In general ODFs, $\rho^{(i)}$ (see Appendix A), can be split in two groups. On the one hand $\rho^{(i)}$ can relate to discrete fiber orientations (i.e. Dirac–deltas in the Ψ_1 – Ψ_2 –domain), and on the other hand $\rho^{(i)}$ can be given by smooth functions in Ψ_1 and Ψ_2 .

Multiple discrete fiber orientations (MT/m) are used in part of this work. Note, that for the special case of aligned inclusions (MT/a) the corresponding ODF degenerates to a single Dirac–delta. The development and implementation of multiple discrete fiber orientations

Table 4.1: Nomenclature for the employed Mori–Tanaka methods.

ODF	inclusion shape	
	cylindrical	spheroidal
aligned inclusions	H–MT/a	E–MT/a
multiple discrete orientations	H–MT/m	E–MT/m
planar random	H–MT/2Dr	E–MT/2Dr
three dimensional random	H–MT/3Dr	E–MT/3Dr

allows for a direct comparison of Mori–Tanaka results and the predictions from multi–inclusion unit cell studies, in which a finite number of inclusions are used to describe periodic model composites. The main difference between unit cell models and such multiple discrete extended Mori–Tanaka approaches (MT/m) is that the latter are not constrained to periodic microgeometries but cannot handle fiber–fiber interaction effects as well as intraphase fluctuations of the microfields in the inclusions and the matrix.

With respect to “smooth” ODFs, planar random fiber arrangements with no out–of–plane deviation (MT/2Dr) and randomly oriented fibers (MT/3Dr) are mainly employed in this work.

4.3 Periodic Microfield Approach

In contrast to the Mori–Tanaka modeling approach discussed in the previous section where homogenization and localization are based on phase averaged temperature gradient and flux fields, one can employ simplified microgeometries for which the local microfields are resolved to a high degree. Periodic microfield approaches describe the macro scale and micro scale behavior of inhomogeneous materials by studying idealized periodic microstructures. These microstructures are partitioned into periodically repeating unit cells to which the investigations are limited without loss of information or generality. Thus, the volume modeled with an unit cell is an appropriate representative volume element of an idealized composite microgeometry.

Unit cells have proven to be highly flexible numerical tools, but they are subject to some intrinsic limitations. Temperature dependent conductivities cannot realistically be modelled as temperatures are accumulated from cell to cell, i.e. conduction properties of cells tiling the computational space are different from the modeled unit cell⁶. Note that this type of problem typically does not occur in the context of mechanics where material non-linearities typically are described in terms of stresses and strains (which corresponds to heat fluxes and temperature gradients) and not displacements (temperatures), the brackets showing the thermal “counterparts”.

The literature on periodic microfield approaches is extensive but focuses mainly on elasticity and plasticity problems. Rolfes and Hammerschmidt ? studied the transverse conductivity of unidirectional continuous fiber reinforced plastic laminates. Islam and Pramila ? investigated continuous fiber reinforced composites, where fibers with square and circular cross-section in square arrangements were considered. The interfacial thermal barrier was modeled as a layer of small (but finite) thickness and poor conductivity, i.e. by introducing a third phase (“interphase”). The same modeling procedure of the imperfect thermal interface was chosen in ?, for investigating the effective conductivity of particle reinforced composites by means of two-dimensional finite element (FEM) models. Two-dimensional problems of heat conduction in porous media (the voids being positioned randomly) were studied by Cruz and Patera ?. Klett *et al.* ? studied cross sections of randomly positioned continuous carbon fibers embedded in a carbon matrix, their model incorporated different fiber morphologies (onion-, radial layer structure) and interfacial debonding.

⁶Temperature dependent behavior of a composite may be approximated by a series of linear unit cell investigations spanning a certain temperature range (see Section 4.1).

4.3.1 Geometries, Mesh, and Application of Loads

In this work two dimensional and three dimensional model geometries are employed, the unit cells being rectangles and cuboids, respectively. The orientation of the unit cell determines a global Cartesian reference coordinate system. The dimensions of a unit cell are $L_1 \times L_2 \times L_3$ (Fig. 4.4). Fiber positions and orientations are generated with different techniques, which are discussed together with the investigated microtopologies in the corresponding results sections.

The microfields of all investigated microgeometries are evaluated with the Finite Element method ????. Due to its geometrical flexibility and its capability of implementing imperfect thermal contacts the FEM represents an efficient numerical engineering tool for the purpose of unit cell analyses. The phase arrangements are meshed with standard continuum elements – six node triangular elements and ten node tetrahedral elements for two dimensional and three dimensional unit cells, respectively. Element boundaries are posi-

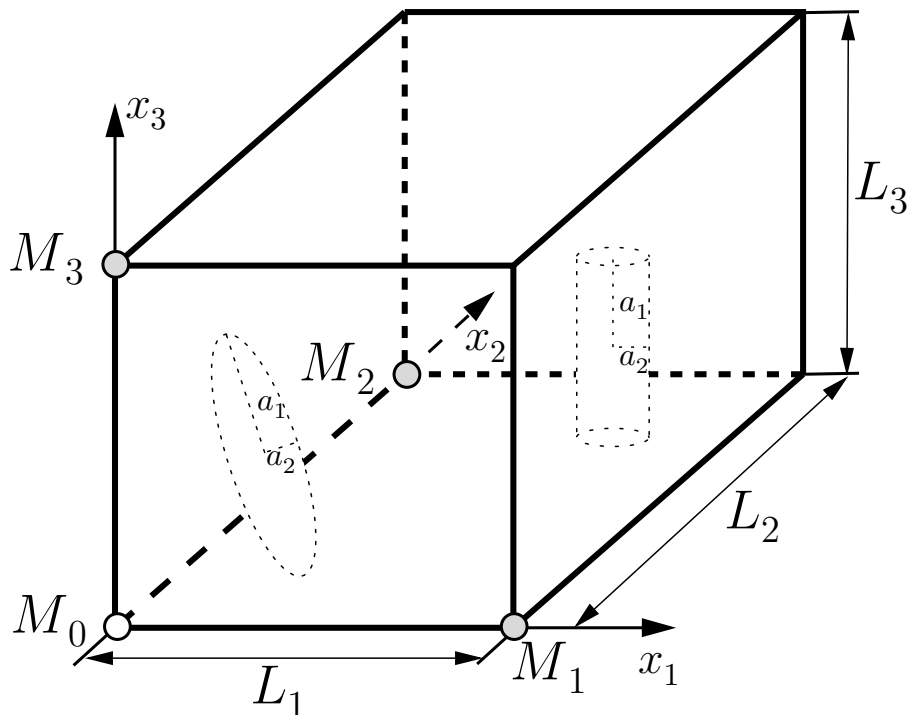


Figure 4.4: A cuboid unit cell with the dimensions L_i and corresponding master nodes M_i containing a spheroidal and a cylindrical inclusion (dotted lines) with the characteristic dimensions a_i . The orientation of the unit cell determines a global Cartesian reference coordinate system.

tioned at all constituent interfaces. The thermal interface is modelled with appropriate contact/target surface elements, which are overlaid on the interfaces, allowing for non-conformal meshes at the interfaces. The interface compatibility conditions (Eq. (5.20)) are enforced by means of contact elements, which requires non linear FEM solution procedures.

The advantage of the chosen approach is that almost any microgeometry can be handled. However, complex meshing operations, small discretisation lengths, and therefore large numbers of DOFs are potential drawbacks of the chosen approach. Note that smaller numbers of DOFs have been obtained for thermomechanical problems by using special elements (e.g. Voronoi FEM ?) or multiphase elements ??, but such approaches are presently restricted to perfectly bonded constituents. All FEM meshes are generated with ANSYS 5.7 and ANSYS 6.1 (ANSYS, Inc., Canonsburg, PA).

The unit cell can either be loaded by using the mathematical framework known as asymptotic homogenization ? or by prescribing nodal temperatures at the master nodes. The latter approach which is referred to as the method of “macroscopic degrees of freedom” in the literature ? is chosen in this work by assigning appropriate temperatures to the master nodes M_i (Fig. 4.4). The nodal temperature is fixed in $M_0(0/0/0)$ to be T_0 . The temperature difference between a master node M_i and M_0 is denoted as ΔT_i and together with the respective length of the unit cell, L_i , the macroscopic far field temperature gradient forced upon the unit cell is then given as $T_{,i}^{(*)} = \Delta T_i / L_i$.

4.3.2 Boundary Conditions

Appropriate boundary conditions (BCs) must ensure that compatible temperature profiles on the unit cell’s faces result for all possible temperature gradients forced upon the unit cell. The two types of BCs employed in this work, symmetry BCs and periodic BCs, are discussed in the following for planar geometries, the extension to three-dimensional cases being trivial. The BCs are incorporated in the models by using multipoint constraints (MPCs) between degrees of freedom.

Symmetry Boundary Conditions

If some microgeometry shows a set of parallel symmetry planes these planes have special properties. For applied far field gradients oriented perpendicular to a symmetry plane the resulting temperature distribution is constant within the symmetry plane under steady

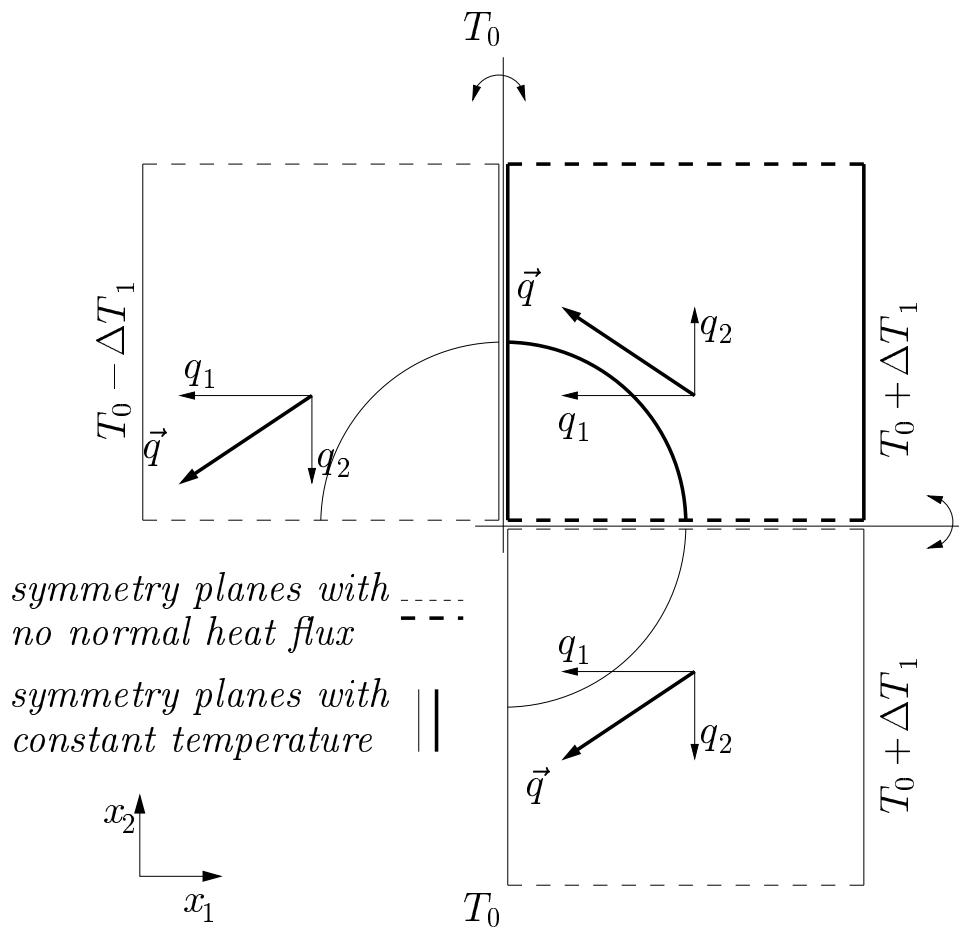


Figure 4.5: Sketch of a symmetric unit cell and two mirror symmetric unit cells for applied far field gradient parallel to the x_1 axis; heat flux at arbitrary point and its two counterparts, located in mirror symmetric unit cells

state conditions, i.e. symmetry planes are isothermal planes. For applied far field gradients acting parallel to a symmetry plane the resulting flux and gradient vectors at points on the plane will have zero out-of-plane components, i.e. no heat flow through the plane occurs, compare Fig. 4.5. The term *symmetry* can be misleading with respect to BCs of unit cells in thermal analyses and it has to be used with care. Considering both orientations of symmetry planes (parallel or perpendicular to the applied far field gradient) the norms of the vector field quantities (heat flux and temperature gradient) and of course the micro topology and material properties are arranged in a symmetric pattern with respect to the planes. The temperature field as well as the vectors of the gradient and flux field, however, are repeated antymmetrically with respect to symmetry planes oriented perpendicularly to

an applied far field gradient, and symmetrically with respect to symmetry planes oriented parallel to an applied far field gradient, see Fig. 4.5.

Symmetry BCs take a very simple form for uniform far field gradients along a principal axis, x_i , and can be applied by assigning constant nodal temperatures on the faces oriented perpendicular to x_i according to

$$T_{x_i=L_i} = T_0 + \Delta T_i = \text{const.} \quad \text{and} \quad T_{x_i=0} = T_0 = \text{const.} \quad , \quad (4.42)$$

forcing a far field gradient of the magnitude $|T_{,i}^{(*)}| = \Delta T_i / L_i$ upon the unit cell. The subscript $x_i=0$ addresses all nodes whose x_i -coordinates are equal to zero. The heat flux across faces parallel to the applied far field gradient is set to zero (Fig. 4.5), which is essentially a BC of the second kind. Only one component of the far field gradient can be applied at one time to avoid temperature incompatibilities in the temperature fields arising from the symmetry BCs.

Symmetry BCs are very useful for describing simple, regular microgeometries, but they are less suitable to model random phase arrangements. On the one hand a random arrangement suitable for symmetry BCs is rather restricted as the fibers may either not touch a face or must be bisected by one or more faces, and on the other hand it is assumed that the heat flux orthogonal to the applied gradient is zero which automatically sets the effective conductivity $K_{12}^{(*)}$ to zero. This applies only for sufficiently large random unit cells with isotropic effective conductivities.

Periodic Boundary Conditions

The most general type of BCs for unit cells are periodic BCs, which can handle any possible applied homogeneous temperature gradient. Periodic BCs are applied by coupling nodal temperatures on opposite faces of the unit cell according to

$$T_{x_i=L_i} - T_{x_i=0} = \Delta T_i \quad , \quad (4.43)$$

which enforces compatible temperature variations on opposing faces (Fig. 4.6). The temperature variations can be thought of as the fluctuating contributions to the temperatures, \tilde{T}_i (dotted lines in Fig. 4.6), around the prescribed linear temperature variation as given by T_0 and the applied temperature differences ΔT_i . Note that the fluctuations \tilde{T}_i are initially unknown and that opposite faces have identical distributions of \tilde{T}_i . It shall also be mentioned that Eq. (4.43) couples the temperatures of node pairs, i.e. nodes on opposing faces with the same “in face” coordinates. Nodes on edges of a three dimensional unit cell,

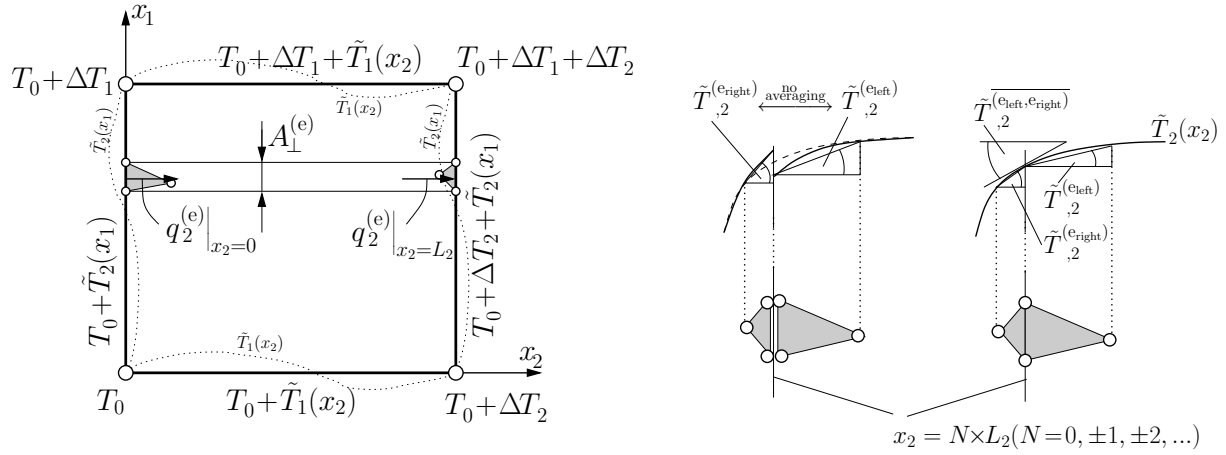


Figure 4.6: Sketch of a unit cell with periodic BCs, forcing identical temperature fluctuations, \tilde{T}_i on opposite faces (left). The nodal solutions of elements on faces are not evaluated in the sense of periodicity, because corresponding elements on the opposite face cannot contribute (right).

which belong to two faces, must be considered in two sets of MPCs and accordingly the right hand side of Eq. (4.43) must be modified by the sum of the temperature differences applied, respectively.

4.3.3 Effective Conductivities

The effective conductivity tensor of the composite as described by the unit cell is evaluated by means of Fourier's law, Eq. (4.11), applied for the homogenized medium. The effective flux, $q_i^{(*)}$, as induced by the far field gradient forced upon the unit cell is given as

$$q_i^{(*)} = \bar{Q}_i / A_i \quad , \quad (4.44)$$

where A_i is the area of an appropriate unit cell face and \bar{Q}_i is the average heat flow across two opposing faces, which is evaluated as

$$\bar{Q}_i = \sum_{(e)} \frac{1}{2} \left(q_i^{(e)} \Big|_{x_i=0} + q_i^{(e)} \Big|_{x_i=L_i} \right) A_\perp^{(e)} \quad . \quad (4.45)$$

Here $A_\perp^{(e)}$ stands for the area of element (e) belonging to a unit cell face and $q_i^{(e)}$ is the respective flux through this area (Fig. 4.6). The flux through an element's face, $q_i^{(e)}$, is approximated by an area-weighted sum of the nodal fluxes of the corner nodes of each

element. Note that only element faces contribute, that lie within a unit cell face (i.e. in the case of tetrahedral elements, three corner nodes must be in the unit cell's face).

Due to the assumption of periodicity, nodes on a unit cell's face always must be thought of as node halves (“twins”), which are cut by the unit cell. Such twins belong to related elements on opposite faces, e_{left} and e_{right} (see Fig. 4.6, right). Twins should have identical temperature gradients and fluxes, but they are on different temperature levels. However, as twins are separated by the unit cell, different nodal temperature gradients (and consistently nodal fluxes) are obtained as only the elements of one face are used for averaging of the nodal results. Accordingly, Eq. (4.45) can be thought to supplementary account for this averaging error.

Note that the effective heat flow Q_i is independent of x_i and any deviation is due approximations within the FEM. For the investigated cases and mesh size the error turned out to be very small, being less than 2% for the diagonal terms (i.e. Q_i due to $T_{,i}^{(*)}$) of the effective conductivity tensor $K_{ii}^{(*)}$ (no sum over i).

The right hand side of Eq.(4.11) is formed by the unknown conductivity tensor of the effective medium, $K_{ij}^{(*)}$, and by the far field gradient $T_{,i}^{(*)} = \Delta T_i / L_i$ which is forced upon the unit cell. Three different far field gradient vectors must be applied sequentially to determine the nine unknown coefficients of $K_{ij}^{(*)}$. These far field gradients must be linearly independent. Arranging them in the matrix $H_{ij} = \left(T_{,i}^{(*)} \right)_j$ with $j = 1, 2, 3$ denoting the j^{th} applied far field gradient vector, the rank of H_{ij} must equal 3 to successfully determine all components of the effective conductivity tensor. Choosing H_{ij} as δ_{ij} is of advantage as each run simply gives the respective column of $K_{ij}^{(*)}$.

It is found that effective conductivities obtained this way tend to slightly violate diagonal symmetry. The latter is enforced afterwards by means of averaging, i.e. $\bar{K}_{ij}^{(*)} = (K_{ij}^{(*)} + K_{ji}^{(*)})/2$. The bar indicating the “diagonalizing” process is omitted in what follows. Enforcing diagonal symmetry only affects the off-diagonal terms which are very small compared to the diagonal terms for the investigated case of randomly oriented inclusions (Chapter 8).

It shall also be mentioned that a far field gradient along x_i also induces global heat flows across faces parallel to x_i , i.e. $\bar{Q}_j \neq 0$, as the periodic unit cell in general is not aligned with the principal material directions of $K_{ij}^{(*)}$. Note that the latter always exist for symmetric second rank tensors ?.

Chapter 5

Single Inclusion Problems

Mean field methods are based on the solution of the boundary value problem of single inhomogeneities embedded in infinitely large matrix materials. This chapter is concerned with single inclusion problems. Solutions are derived for spheroidal inclusions and a general numerical solution procedure is proposed for inclusions of arbitrary shape. Both perfect thermal interfaces and interfacial thermal resistances are considered. Furthermore, symmetry relations are provided.

5.1 Spheroidal Inhomogeneities

In this section an analytical approach is presented for solving the steady state thermal conductivity problem of the following configuration. An infinite matrix material contains a single inhomogeneous spheroidal inclusion and a thermal resistance is present at the pertinent interface. The matrix shows isotropic conductivity while the inclusion is transversally isotropic, the principal material axes being aligned with the spheroid.

Analytical expressions are derived for the local gradient fields in the matrix and in the inclusion as well as for the temperature mismatch along the interface. An analytical method is developed which allows replacing the original imperfectly bonded inclusion by a less conductive but perfectly bonded inclusion. For the specific case of *confocal* distributions of the interface resistance the present approach yields the exact solution, i.e. the replacement operation leaves the matrix fields unchanged. For general spatial distributions of the interface properties (meeting the spheroidal symmetry properties) an approximate solution strategy is introduced that provides estimates.

The further application of the present method for investigations of non-dilute composites is discussed in terms of *homogenization* and *localization*. The effect of the inclusion size in combination with an interface resistance on the conductivity of non-homogeneous systems is addressed, as are critical inclusion dimensions.

The proposed method is compared with existing approaches from the literature. Additionally, cross links to established models of coated inclusions are provided. As an example the material system of diamond inclusions in zinc sulfide matrix is considered. Predictions are compared with results from analytical approaches as well as numerical results from finite element analyses.

5.1.1 Literature Overview

Whereas a range of approaches is available for estimating the effective thermal conductivity of heterogeneous media with perfectly bonded constituents, works taking into account imperfect thermal interfaces are less numerous. Problems of the latter type have received attention recently since highly conducting composite materials have started to be employed in e.g. heat sink applications in microelectronics.

Hasselmann and Johnson ? considered imperfectly bonded spherical particles and cylinders of circular cross section (oriented perpendicularly to the heat flow) at dilute volume fractions. Chen ? investigated a single cylinder of circular cross section embedded in an infinite

matrix, adopting the idea of an imperfect thermal interface with a variable interface parameter. Chiew and Glandt [?] as well as Benveniste [?] studied particle reinforced composites at nondilute volume fractions, accounting for a thermal barrier between the constituents. While particle interaction was modeled by means of a second order approximation in [?], a Mori–Tanaka method (effective field approach) and a self-consistent scheme (effective medium approach, EMA) were employed in [?]. For the case of spheroidal inclusions the problem is more difficult compared to the special cases of spherical or cylindrical inclusions. Benveniste and Miloh [?] outlined fundamental concepts in the theory of heat conduction in the presence of imperfect thermal interfaces. A procedure involving spheroidal harmonics was developed and applied to the case of spheroidal inclusions at dilute volume fractions. Lu [?] estimated the effective conductivities of composites reinforced by aligned spheroidal inclusions having the same shape, size and constant interface parameter β using an equivalent inclusion method.

An alternative approach to implementing interfacial thermal resistances is that of appropriately modifying models for coated inclusions so that the effect of the interfacial thermal barrier is obtained by a thin coating of very low conductivity. Nan *et al.* [?] provided estimates based on coatings of constant thickness and subsequently employed an EMA for predicting the overall conductivity of two–phase composite materials with an interfacial thermal resistance between the constituents. Dunn and Taya [?] introduced a variable interface parameter β as their considerations are based on coatings defined by two confocal spheroids, the interaction between inclusions being accounted for by means of a Mori–Tanaka scheme. Benveniste and Miloh [?] investigated coated ellipsoidal inclusions, the coating being represented by two confocal ellipsoids. As no restriction is placed on the coating’s thickness, their results can be applied to the case of interfacial thermal resistances in a straightforward way.

5.1.2 Perfectly Bonded Inclusions

In this section a single spheroidal inclusion of isotropic conductivity $K_{ij}^{(i)}$ embedded in an infinite, isotropic matrix material of conductivity $K_{ij}^{(m)}$ is considered, inclusion and matrix being treated as perfectly bonded. The interface Γ is the set of all points belonging to the second degree surface (quadric)

$$G_{ij}x_ix_j = 1 \quad . \quad (5.1)$$

The inverses of the square roots of the eigenvalues of G_{ij} are the semi–axes a_i of an ellipsoid. The axes of the global Cartesian coordinate system are taken to coincide with the principal

axes of the quadric. The present work refers to the special case of spheroids that are considered to be aligned with x_1 , i.e. $a_2 = a_3$.

For a uniform far field temperature gradient solutions for the temperature distribution inside the spheroid, $T^{(i)}$, and outside the spheroid, $T^{(m)}$, are given e.g. in ?, where also expressions for the more general case of ellipsoids are provided. Introducing the tensors ${}^0D_{ij}$ and ${}^\lambda D_{ij}$, the temperature distribution inside the spheroid can be expressed in the form

$$T^{(i)} = {}^0D_{ij} T_{,j}^{(*)} x_i + T_0 \quad , \quad (5.2)$$

and the temperature field outside the spheroid is given by

$$T^{(m)} = {}^\lambda D_{ik} {}^0D_{kj} T_{,j}^{(*)} x_i + T_0 \quad . \quad (5.3)$$

Without loss of universality the temperature at the origin, T_0 , is set to zero from now on. Temperature gradients $\partial T^{(*)}/\partial x_i$, are denoted as $T_{,i}$, and the superscript $(*)$ refers to the matrix phase at infinity, where the influence of the spheroid is not felt. ${}^0D_{ij}$ and ${}^\lambda D_{ij}$ can be expressed as

$${}^0D_{ij} = \left[\delta_{ij} + {}^0S_{ik} R_{kl}^{(m)} \left(K_{lj}^{(i)} - K_{lj}^{(m)} \right) \right]^{-1} \quad (5.4)$$

$${}^\lambda D_{ij} = \left[\delta_{ij} - ({}^\lambda S_{ik} - {}^0S_{ik}) R_{kl}^{(m)} \left(K_{lj}^{(i)} - K_{lj}^{(m)} \right) \right] \quad , \quad (5.5)$$

where δ_{ij} is the Kronecker Delta ($\delta_{ij} = 0$ for $i \neq j$ and $\delta_{ij} = 1$ for $i = j$), R_{ij} stands for the resistivity tensor that is the reciprocal of the conductivity tensor K_{ij} , and S_{ij} accounts for the influence of the aspect ratio of the spheroid. Following ? the components of S_{ij} can be evaluated for spheroidal inclusions from the integral functions

$${}^\lambda S_{11} = \frac{a_1 a_2^2}{2} \int_\lambda^\infty \frac{1}{(a_1^2 + s)^{\frac{3}{2}} (a_2^2 + s)} ds \quad (5.6)$$

$${}^\lambda S_{22} = {}^\lambda S_{33} = \frac{a_1 a_2^2}{2} \int_\lambda^\infty \frac{1}{(a_1^2 + s)^{\frac{1}{2}} (a_2^2 + s)^2} ds \quad , \quad (5.7)$$

all other components being zero. The lower integration boundary λ is the solution of

$$\left[G_{ij}^{-1} + \lambda \delta_{ij} \right]^{-1} x_i x_j = 1 \quad , \quad (5.8)$$

the loci of $\lambda = \text{const.}$ being confocal spheroids. For points on Γ or inside the spheroid λ is set to zero, and ${}^0S_{ij}$ coincides with the thermal equivalent of the interior field Eshelby tensor ????. For points outside the spheroid λ is taken to be the positive solution of Eq. (5.8) and the square root of λ can be thought of as a generalized distance from the interface Γ .

For $\lambda \rightarrow \infty$ the components of the exterior field Eshelby tensor ${}^\infty S_{ij}$ tend to zero, ${}^\infty D_{ij}$ becomes the inverse of ${}^0 D_{ij}$, and Eq. (5.3) is reduced to $T^{(m)} = T_{,i}^{(*)} x_i$, i.e. the influence of the spheroid vanishes.

The integral expressions for λS_{ii} , Eqs. (5.6) and (5.7), can be solved analytically. The results can be presented as functions of the lower integration limit λ .

$$\lambda S_{11} = \frac{a_1 a_2^2}{2} \left(\frac{2}{(a_2^2 - a_1^2)(a_1^2 + \lambda)^{\frac{1}{2}}} + \frac{2 \operatorname{atanh} \left(\left(\frac{a_1^2 + \lambda}{a_1^2 - a_2^2} \right)^{\frac{1}{2}} \right)}{(a_1^2 - a_2^2)^{\frac{3}{2}}} \right) . \quad (5.9)$$

$$\lambda S_{22} = \lambda S_{33} = \frac{a_1 a_2^2}{2} \left(\frac{(a_1^2 + \lambda)^{\frac{1}{2}}}{(a_1^2 - a_2^2)(a_2^2 + \lambda)} - \frac{\operatorname{atanh} \left(\left(\frac{a_1^2 + \lambda}{a_1^2 - a_2^2} \right)^{\frac{1}{2}} \right)}{(a_1^2 - a_2^2)^{\frac{3}{2}}} \right) . \quad (5.10)$$

Unlike in ??? a closed-form solution for inclusions of arbitrary aspect ratio is provided with the exception of spheres ($a_1 = a_2$). For that case the solutions of the integral expressions, Eqs. (5.6) and (5.7), reduce to

$$\lambda S_{11} = \lambda S_{22} = \lambda S_{33} = \frac{a_1^3}{3(a_1^2 + \lambda)^{\frac{3}{2}}} , \quad (5.11)$$

yielding ${}^0 S_{ii} = \frac{1}{3}$ (no sum over i) for spheres. Note that the identity ${}^0 S_{ii} = 1$ is valid for all inclusion geometries ?.

All solutions provided above apply to a perfect thermal interface denoted by Γ . The compatibility conditions on Γ state that the normal component of the heat flux and the temperature field are continuous across the interface, i.e. for points on Γ the conditions

$$q_i^{(i)} n_i \Big|_{\Gamma} = q_i^{(m)} n_i \Big|_{\Gamma} \quad \text{and} \quad T^{(i)} \Big|_{\Gamma} = T^{(m)} \Big|_{\Gamma} , \quad (5.12)$$

respectively, must be satisfied. Here n_i is the dimensionless unit normal vector on Γ pointing into the matrix phase and $q_i^{(r)}$ is the heat flux that is generated by the temperature gradient field $T_{,i}^{(r)}$ according to Fourier's law, Eq. (4.2), the superscript r standing for the matrix and inclusion phases, respectively.

Taking the derivative of Eq. (5.2) with respect to x_i yields

$$T_{,i}^{(i)} = {}^0 D_{ij} T_{,j}^{(*)} , \quad (5.13)$$

so that ${}^0 D_{ij}^{(i)}$ can be identified with the dilute concentration tensor as introduced in Eq. (4.30) for a single inclusion. Equation 5.13 shows that the temperature gradient field (and the

corresponding flux field) due to a uniform far field gradient is homogeneous within a spheroidal inclusion in correspondence with the well-known Eshelby property of ellipsoids. The gradient field in the matrix is not constant and approaches the far field gradient field only at large distances from the inclusion. Computing the local temperature gradients in the matrix phase, $T_i^{(m)}$, from Eq. (5.3) requires the derivatives of ${}^\lambda D_{ii}$ with respect to x_j , ${}^\lambda D_{ii,j}$. (Note that only the derivatives of the diagonal terms, ${}^\lambda D_{ii,j}$, need to be computed, the off-diagonal terms and their derivatives being zero). As can be seen from Eq. (5.5) the derivatives ${}^\lambda D_{ii,j}$ are proportional to the derivatives ${}^\lambda S_{ii,j}$. Analytical solutions of the temperature gradient field in the matrix $T_i^{(m)}$ can be obtained either by numerical differentiation or analytically, which is exact and, once implemented, computationally more efficient. Taking the derivative of the matrix temperature field, Eq. (5.3), with respect to x_j introduces the derivatives ${}^\lambda D_{ii,j}$. Equation (5.5) shows that the problem of evaluating the derivatives ${}^\lambda D_{ii,j}$ reduces to finding the derivatives of the integral functions, ${}^\lambda S_{ii,j}$. The latter can be calculated as

$${}^\lambda S_{ii,j} = {}^\lambda S_{ii,\lambda} \lambda_{,j} \quad . \quad (5.14)$$

Equation (5.14) introduces two sub-problems, namely evaluating the derivatives ${}^\lambda S_{ii,\lambda}$ and the derivatives $\lambda_{,i}$, each of which allows for an analytical solution.

First the derivatives of ${}^\lambda S_{ii}$ with respect to λ are calculated, yielding

$${}^\lambda S_{11,\lambda} = -\frac{a_1 a_2^2}{2} \frac{1}{(a_1^2 + \lambda)^{\frac{3}{2}} (a_2^2 + \lambda)} \quad , \quad (5.15)$$

$${}^\lambda S_{22,\lambda} = {}^\lambda S_{33,\lambda} = -\frac{a_1 a_2^2}{2} \frac{1}{(a_1^2 + \lambda)^{\frac{1}{2}} (a_2^2 + \lambda)^2} \quad . \quad (5.16)$$

For points on the interface Γ ($\lambda = 0$) the terms simplify to ${}^0 S_{11,\lambda} = -\frac{1}{2a_1^2}$ and ${}^0 S_{22,\lambda} = {}^0 S_{33,\lambda} = -\frac{1}{2a_2^2}$.

Secondly the derivatives of λ with respect to x_i are needed. Differentiating Eq. (5.8) with respect to x_i yields

$$\lambda_{,1} = \frac{2x_1}{(a_1^2 + \lambda)} \left[\frac{x_1^2}{(a_1^2 + \lambda)^2} + \frac{x_2^2 + x_3^2}{(a_2^2 + \lambda)^2} \right]^{-1} \quad , \quad (5.17)$$

$$\lambda_{,2} = \frac{2x_2}{(a_2^2 + \lambda)} \left[\frac{x_1^2}{(a_1^2 + \lambda)^2} + \frac{x_2^2 + x_3^2}{(a_2^2 + \lambda)^2} \right]^{-1} \quad , \quad (5.18)$$

$$\lambda_{,3} = \frac{2x_3}{(a_2^2 + \lambda)} \left[\frac{x_1^2}{(a_1^2 + \lambda)^2} + \frac{x_2^2 + x_3^2}{(a_2^2 + \lambda)^2} \right]^{-1} \quad . \quad (5.19)$$

In the present section, all tensors are given with respect to the global Cartesian coordinate system. As the orientation of the spheroid is chosen such that its principal axes coincide

with the global axes all second rank tensors are diagonal tensors. As a consequence $T_{,i}^{(*)}$ causes only a temperature gradient $T_{,i}^{(i)}$ in the inclusion and no normal temperature gradients. All of the above expressions can be immediately applied to the case of orthotropic inclusion conductivities, provided the axes of orthotropy coincide with the principal axes of the spheroid ?. The conductivity of the matrix phase, however, is restricted to be isotropic. It may be noted that the Eshelby property also holds for anisotropic matrix conductivities ?, but more complicated formulae must be used to handle such cases.

5.1.3 Imperfectly Bonded Inclusions

In this section it is shown that a spheroidal inclusion of transversally isotropic conductivity (the plane of isotropy being perpendicular to x_1), which is bonded imperfectly to the isotropic matrix, can be replaced by a less conductive, but perfectly bonded inclusion, referred to as replacement inclusion, such that the matrix field is left unchanged.

If an interfacial thermal resistance exists, then the interface is referred to as Γ_β , the subscript β indicating the presence of a thermal resistance on Γ . The variation of the interface parameter on Γ_β is restricted to functions that are axisymmetric with respect to x_1 and which, in addition, show mirror symmetry with respect to the x_2 - x_3 -plane. The temperature field is discontinuous at the imperfect interface, while the continuity of the heat fluxes across the interface is maintained. The temperature jump across the interface is linked to the heat flux across the interface via the interface parameter β according to

$$q_i^{(i)} n_i \Big|_{\Gamma_\beta} = q_i^{(m)} n_i \Big|_{\Gamma_\beta} = \beta \left(T^{(i)} \Big|_{\Gamma_\beta} - T^{(m)} \Big|_{\Gamma_\beta} \right) = \beta \Delta T \Big|_{\Gamma_\beta} \quad . \quad (5.20)$$

Two limiting cases can be readily obtained, on the one hand a perfectly insulating interface, Γ_0 , and, on the other hand, a perfectly "conducting" interface, Γ , the subscript ∞ being omitted.

The derivation of the proposed method is carried out in two steps. First investigations are carried out on the thermal fields along the principal axes x_i due to a uniform far field gradient $T_{,i}^{(*)}$. The problem is reduced to two independent one-dimensional ones on account of the symmetry assumptions prescribed to the interface parameter. At this stage the thermal resistance is solely defined in terms of principal interface parameters at the spheroid's poles, ${}^p\beta_{,i}$, the latter being defined as the intersection points between the principal axes of the spheroid and its surface. For the cases considered here the one-dimensional problems can be treated as decoupled scalar equations, because all tensors

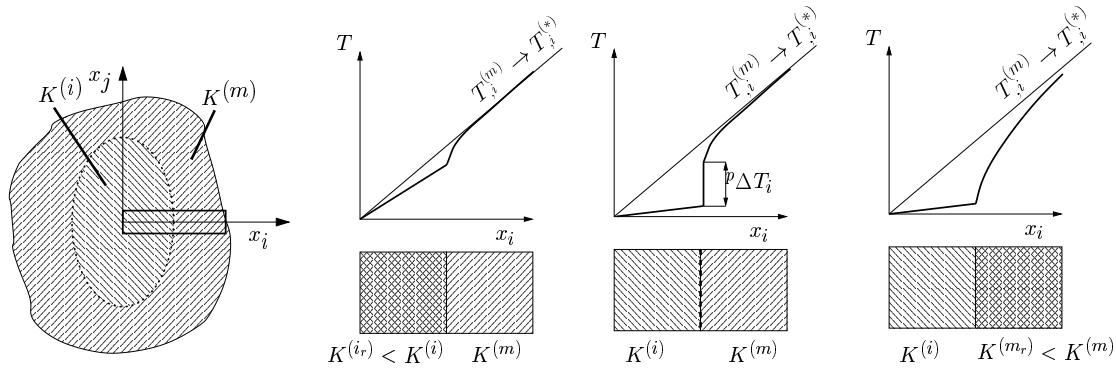


Figure 5.1: Sketch of the actual set-up of matrix $K^{(m)}$, inclusion $K^{(i)}$ and imperfect interface (center) and of the two auxiliary configurations (left and right) with perfect interfaces. The effects of the interfacial thermal resistance are modeled by introducing reduced phase conductivities ($K^{(m_r)}$ or $K^{(i_r)}$), the normal component of the flux across the interface being the same in all three configurations.

involved are diagonal.

In the second step the heat flux across the interface is used to link the principal interface parameters ${}^p\beta_i$ and ${}^p\beta_j$. Specific spatial distributions of β at the interface are identified for which the non-ideal thermal compatibility conditions, Eq. (5.20), are satisfied on Γ_β .

One-Dimensional Problems

The basic idea of the proposed method consists in accounting for the presence of a thermal barrier by either reducing the conductivity of the inclusion phase or that of the matrix phase, while treating the thermal interface as perfect. This way two auxiliary configurations incorporating perfectly bonded constituents are introduced, compare Fig. 5.1, for each of which Eqs. (5.2) to (5.13) are applicable. The two fictitious conductivities associated with this approach are referred to as the *reduced inclusion conductivity*, $K_{ij}^{(i_r)}$, and the *reduced matrix conductivity*, $K_{ij}^{(m_r)}$. They are chosen such that the (constant) heat flux in the inclusion is the same in the original and the two auxiliary configurations, giving rise to the conditions

$$\begin{aligned} q_i &= -K_{ik}^{(i)} {}^0D_{kj}^{(m_r,i)} T_{,j}^{(*)} \quad , \\ &= -K_{ik}^{(i_r)} {}^0D_{kj}^{(m,i_r)} T_{,j}^{(*)} \quad . \end{aligned} \quad (5.21)$$

As the dilute concentration tensors ${}^0D_{ij}$ depend on the conductivities of both matrix and inclusion, they are annotated with additional superscripts in order to avoid any confusion

with respect to the configurations they refer to.

The two auxiliary configurations, of course, give rise to different temperature distributions for a given uniform far field gradient $T_i^{(*)}$. The temperature mismatch between the two auxiliary configurations at the poles is set to equal the temperature jump of the imperfectly bonded configuration, ${}^p\Delta T_i$, there, giving

$${}^p\Delta T_i = \left[{}^0D_{ij}^{(m,ir)} - {}^0D_{ij}^{(mr,i)} \right] T_{,j}^{(*)} {}^p x_i \quad \text{no sum over } i, \quad (5.22)$$

where ${}^p x_i = \pm a_i$ are the semi-axes of the spheroid. Because from Eq. (5.20) the temperature jump at the i -th pole is known to be $q_i n_i = {}^p\beta_i {}^p\Delta T_i$ (no sum over i), Eqs. (5.21) and (5.22) can be used to solve for the two unknown components of the reduced conductivity tensors which, after some algebra, can be obtained as

$$K_{ii}^{(ir)} = \left[1 + ({}^p\beta_i a_i)^{-1} K_{ii}^{(i)} \right]^{-1} K_{ii}^{(i)} \quad \text{no sum over } i, \quad (5.23)$$

and

$$K_{ii}^{(mr)} = \left[1 + ({}^p\beta_i a_i)^{-1} \left({}^0S_{ii}^{-1} - 1 \right) K_{ii}^{(m)} \right]^{-1} K_{ii}^{(m)} \quad \text{no sum over } i. \quad (5.24)$$

Considerations of the thermal fields along the principal axes thus provide the components of the reduced conductivity tensors, with the relations between the principal components remaining to be studied. Before doing this, however, Eqs. (5.23) and (5.24) are briefly discussed. Each of the reduced conductivities can be seen to be independent of the material properties of the other phase, the reduction of the conductivity being ultimately determined by the product of the interface parameter and a characteristic length a_i which is referred to as *interface conductance*.

In Fig. 5.2 the dependence of the reduced inclusion conductivity, $K^{(ir)}$, on the interface conductance βa is plotted for a number of inclusion conductivities with the characteristic length a being chosen as the radius of spherical inclusions. A typical S-shape can be observed ????. When considering inclusion conductivities of up to 10^3 W/mK a marked variability of the reduced inclusion conductivity $K^{(ir)}$ is found for an intermediate range of the interface conductances [$10^1 - 10^4$ W/mK]. In the top left corner of Fig. 5.2 the dependence of $K^{(ir)}$ on the interface parameter is plotted for $K^{(i)} = 250$ W/mK. While the solid curve corresponds to a characteristic length a , the dashed curves correspond to lengths that are ten times smaller ($a/10$) and ten times larger ($10a$). Evidently a size effect (and thus an absolute length scale) has been introduced with Eq. (5.23), causing large inclusions to give rise to higher reduced conductivities than do small ones — a fact validated by experiments ???. Dunn and Taya ? suggested that this effect is due to the fact that the ratio of inclusion surface area to volume increases as the inclusion size decreases.

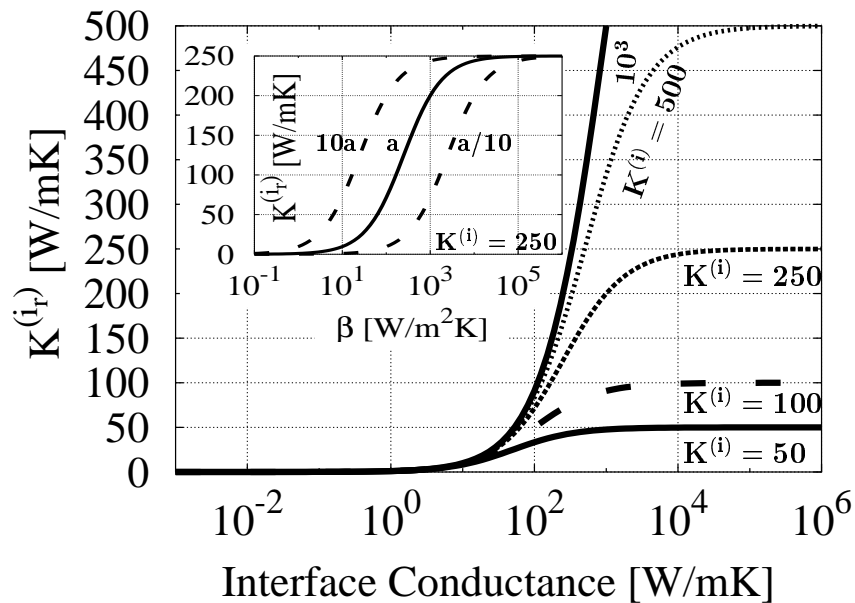


Figure 5.2: Reduced conductivities of spherical inclusions as functions of the interface conductance for inclusion conductivities of 50, 100, 250, 500, and 1000 W/mK. At the top left the reduced conductivity of a spherical inclusion ($K^{(i)} = 250$ W/mK) of unit radius is plotted over the interface parameter β (solid curve). The dashed lines correspond to spherical inclusions of the same conductivity but having ten times smaller and ten times larger radii.

For the case of spherical inclusions with an isotropic conductivity exceeding that of the matrix phase and a given interface parameter a critical particle radius, r_{cr} , can be defined, for which the reduced inclusion conductivity equals the matrix conductivity. Substituting $K^{(i_r)}$ by $K^{(m)}$ in Eq. (5.23) and solving for the characteristic length yields

$$r_{cr} = \frac{1}{\beta} \frac{K^{(i)} K^{(m)}}{K^{(i)} - K^{(m)}} \quad , \quad (5.25)$$

the subscripts being omitted on account of the isotropic phase conductivities. The concept of a critical particle radius was also pointed out by Torquato and Rintoul ? and by Lipton and Vernescu ??. The latter emphasized that Eq. (5.25) is not restricted to the dilute case but also holds for suspensions of spheres at nondilute volume fractions. The knowledge of the critical particle radius is of considerable practical interest, as a minimum reinforcement size can be determined which must be exceeded in order to achieve an effective conductivity of a composite material that surpasses that of the actual matrix material for a given interface parameter. Equation (5.25) can be applied to the case of cylindrical inclusions as

well, r_{cr} then playing the role of a critical cylinder radius.

As a by-product of the above procedure a fictitious reduced and (in general) orthotropic matrix conductivity, $K_{ij}^{(mr)}$, is obtained, compare Eq. (5.24). This reduced conductivity and the associated auxiliary configuration must be viewed with considerable care, because the corresponding dilute composite in general has a different overall conductivity than the actual configuration (note that Eq. (5.21) constrains the heat fluxes in the inclusions to be identical, but those in the surrounding matrix may differ). On account of the orthotropy of $K_{ij}^{(mr)}$ Eqs. (5.4) to (5.7) do not hold.

Furthermore it must be mentioned that the investigations pertinent to each principal axis are based on one pair of auxiliary configurations, hence a total of two pairs of auxiliary configurations are introduced in the case of spheroids. Accordingly, two reduced isotropic matrix conductivity tensors, $K_{11}^{(mr)}\delta_{ij}$ and $K_{22}^{(mr)}\delta_{ij} = K_{33}^{(mr)}\delta_{ij}$, and two reduced isotropic inclusion conductivity tensors, $K_{11}^{(ir)}\delta_{ij}$ and $K_{22}^{(ir)}\delta_{ij} = K_{33}^{(ir)}\delta_{ij}$, are obtained. Each of the reduced conductivities is isotropic because Eqs. (5.21) and (5.22) are based on isotropic constituent conductivities. As only diagonal tensors are involved, so that equations in x_i are decoupled, the two reduced matrix and inclusion conductivities can be condensed to give the (in general) orthotropic "tensors" $K_{ij}^{(mr)}$ and $K_{ij}^{(ir)}$.

Accordingly, the dilute concentration tensor ${}^0D_{ij}^{(mr,i)}$ does not relate to a matrix phase of orthotropic conductivity but relates to two of the original spheroidal inclusions ($K_{ij}^{(i)}$) each of which is embedded in an isotropic matrix material, respectively. Therefore the use of ${}^0D_{ij}^{(mr,i)}$ is restricted to determining inclusion gradient fields of one inclusion which is considered to be embedded in "two" isotropic matrix materials at the same time, once again taking advantage of the fact that only diagonal tensors are involved.

The concentration tensor ${}^0D_{ij}^{(m,ir)}$, however, relates to an orthotropic inclusion embedded in an isotropic matrix material and therefore Eqs. (5.2) to (5.13) are applicable.

Confocal Interface Parameters

Comparing the temperature distributions in the spheroids obtained from the two auxiliary configurations, the temperature mismatch ΔT_i on Γ_β due to an applied temperature gradient $T_{,i}^{(*)}$ can be seen to depend linearly on x_i ,

$$\Delta T_i = \left[{}^0D_{ij}^{(m,ir)} - {}^0D_{ij}^{(mr,i)} \right] T_{,j}^{(*)} x_i \quad , \quad \text{no sum over } i \quad . \quad (5.26)$$

As the gradient field $T_{,i}^{(i)}$ within the spheroid is constant, the corresponding heat flux across the interface, $q_i n_i$, can be evaluated by expressing n_i as

$$n_i = G_{ij} x_j \frac{1}{\sqrt{G_{km} G_{ml} x_k x_l}} \quad , \quad (5.27)$$

which shows that $q_i n_i$ depends nonlinearly on x_i .

As the heat flux across the interface, Eq. (5.21) and (5.27), and the temperature mismatch on Γ_β , Eq. (5.26), are known, the non-ideal thermal coupling conditions, Eq. (5.20), can be employed, giving $\beta(x_i) = q_i n_i \Delta T_i^{-1}$ (no sum over i). Introducing the known state at a pole, Eq. (5.22), and some lengthy algebra yield

$$\beta = \frac{{}^p\beta_i}{a_i} \frac{1}{\sqrt{G_{km} G_{ml} x_k x_l}} \quad , \quad (5.28)$$

the variation of the interface parameter depending on the spheroid's geometry, the polar principal interface parameters and the position on Γ only. Such a variation of the interface parameter fulfills the non-ideal thermal coupling conditions at any point on the interface for the given normal components of the heat flux and the temperature mismatch. Because Eq. (5.28) must be fulfilled for all one-dimensional contributions, ${}^p\beta_i$ unambiguously determines ${}^p\beta_j$ and vice versa as

$${}^p\beta_i a_j = {}^p\beta_j a_i \quad . \quad (5.29)$$

If the interface parameter β varies on Γ_β according to Eq. (5.28), the non-ideal thermal compatibility conditions are satisfied at any point on the interface for any applied far field gradient. In that case – and only in that case – the perfectly bonded replacement inclusion of conductivity $K_{ij}^{(ir)}$ gives rise to the same temperature distribution in the matrix phase on the interface, $T^{(m)} \Big|_\Gamma$, as does an imperfectly bonded inclusion of conductivity $K_{ij}^{(i)}$. Accordingly, the temperature field and the corresponding gradient fields throughout the whole matrix domain are not affected by the replacement operation provided Eq. (5.28) is fulfilled.

Models Based on Coatings A thermal interfacial resistance can be thought of as a very thin isotropic layer (“interphase”) of thickness t and very low isotropic conductivity $K^{(s)}$ that is spread over the surface of the spheroidal inclusion. Within the framework of such a model a variable interface parameter $\beta(\theta)$ corresponds to a coating of variable thickness $t(\theta) = K^{(s)}/\beta(\theta)$, where both $K^{(s)}$ and t tend towards zero, compare Fig. 5.3. Neglecting terms in t^2 it can be shown that Eq. (5.28) can be approximated by a coating of variable

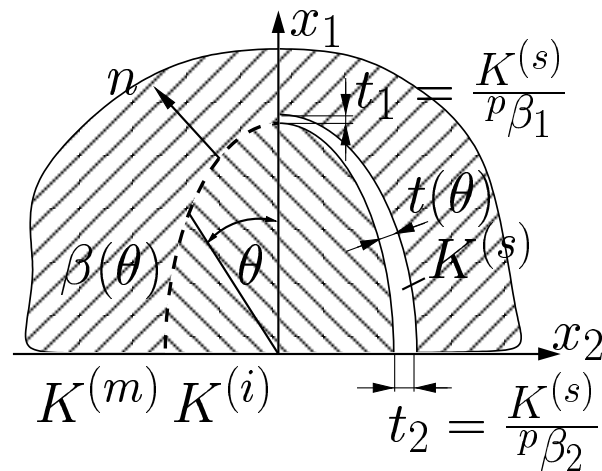


Figure 5.3: Sketch of an inclusion with an interfacial thermal resistance $\beta(\theta)$ described by a thin interfacial layer of thickness $t(\theta)$ of low conductivity $K^{(s)}$. A dependence of β satisfying the confocality condition is given by a variable coating thickness defined by two confocal spheroids.

thickness $t(\theta)$ defined by two confocal spheroids with semi-axes (a_1, a_2) and $(a_1 + t_1, a_2 + t_2)$, respectively, where $t_1 = K^{(s)}/p\beta_1$ and $t_2 = K^{(s)}/p\beta_2$. Accordingly, Eq. (5.28) is referred to as the *confocality condition*. Analytical micromechanical models employing confocal coatings have been used in ?? to study the effects of interfacial thermal resistances. Results from numerical evaluations in ? agree with those obtained by Eq. (5.23), but the present method is much simpler, involving only algebraic tensor operations.

Homogenization and Localization If the effective conductivity of a heterogeneous material with imperfectly bonded constituents is estimated by means of effective field or effective medium theories (e.g. Mori–Tanaka or self-consistent approaches), the thermal conduction behavior of the material can be modeled via the perfectly bonded replacement inclusions of reduced conductivity $K_{ij}^{(i_r)}$ as defined by the present approach. The respective non-dilute phase concentration tensors must be based on ${}^0D_{ij}^{(m, i_r)}$ evaluated from Eqs. (5.4) and (5.23). Zooming in on the local temperature gradient field of the actual inclusion (localization), however, must be carried out by means of the concentration tensor ${}^0D_{ij}^{(m, i)}$, which can be evaluated as

$${}^0D_{ij}^{(m, i)} = R_{ik}^{(i)} K_{kl}^{(i_r)} {}^0D_{lj}^{(m, i_r)} \quad , \quad (5.30)$$

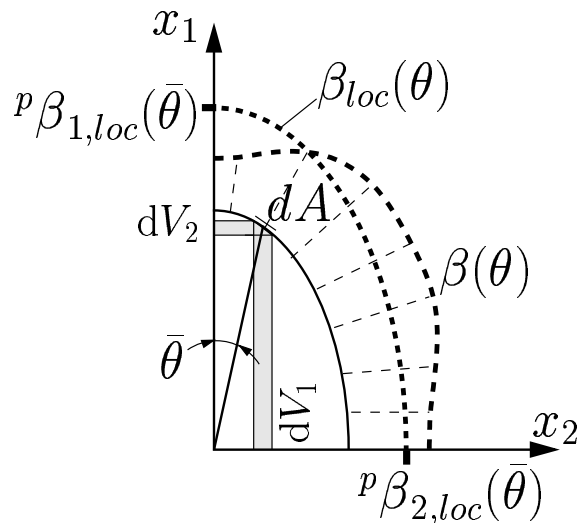


Figure 5.4: Sketch of the proposed averaging procedure for non-confocal thermal resistances $\beta(\theta)$ showing the volumes dV_1 and dV_2 associated with the annular area dA on Γ_β . At position $\bar{\theta}$ the actual resistance $\beta(\theta = \bar{\theta})$ is approximated by the local confocal resistance $\beta_{loc}(\bar{\theta})$ which is associated with the polar principal resistances ${}^p\beta_{1,loc}(\bar{\theta})$ and ${}^p\beta_{2,loc}(\bar{\theta})$.

using the equality of inclusion heat fluxes of the original configuration and the two auxiliary configurations. Note that evaluating the temperature gradient field of the actual inclusion directly with ${}^0D_{ij}^{(mr,i)}$ is a potentially inconsistent shortcut within the framework of the present approach.

5.1.4 Approximate Solutions for Non-Confocal Cases

If the spatial variation of the interface parameter does not satisfy the confocality condition, Eq. (5.28), the gradient fields will not be constant in ellipsoidal inclusions. An approximate solution procedure for obtaining estimates for the reduced inclusion conductivity is proposed for such cases.

Let the interface parameter $\beta(\theta)$ vary on Γ_β according to some function of θ which is axisymmetric with respect to x_1 and shows mirror symmetry with respect to the x_2 - x_3 -plane, i.e. $\beta(\theta) = \beta(\pi - \theta)$, but violates the confocality condition. Under these conditions it is sufficient to analyze the meridional cross section in the x_1 - x_2 -plane sketched in Fig. 5.4. As a first step, the actual non-confocally distributed interface parameter $\beta(\theta)$ is approximated by a set of confocal interface parameters $\beta_{loc}(\theta)$. These local approximations are

chosen such that $\beta_{\text{loc}}(\theta = \bar{\theta}) = \beta(\bar{\theta})$ holds for each location $\bar{\theta}$ on the interface Γ_β . The principal interface parameters at the poles corresponding to such a local approximation, ${}^p\beta_{i,\text{loc}}(\bar{\theta})$, can be obtained as

$${}^p\beta_{i,\text{loc}}(\bar{\theta}) = a_i \sqrt{G_{km}G_{ml}x_kx_l} \beta(\bar{\theta}) \quad . \quad (5.31)$$

by rearranging Eq. (5.28).

Next, the principal interface parameters obtained from Eq. (5.31) are plugged into Eq. (5.23) to obtain local estimates for the principal components of the reduced inclusion conductivities $K_{ii,\text{loc}}^{(i_r)}(\bar{\theta})$. Each of these local estimates is associated with an infinitesimal annular area $dA(\bar{\theta})$ on Γ_β and with two infinitesimal axisymmetric volumes in the inclusion, $dV_1(\bar{\theta})$ and $dV_2(\bar{\theta})$, which are arranged such that their projections to the interface along the respective principal axis coincide with dA , compare Fig. 5.4.

Finally, the principal components of the averaged reduced conductivities of inclusions with non-confocally distributed interface parameters, $\bar{K}_{ii}^{(i_r)}$, are obtained as volume weighted averages over $K_{ii,\text{loc}}^{(i_r)}$ in the form

$$\bar{K}_{ii}^{(i_r)} = \frac{1}{V^{(i)}} \int_{V_i^{(i)}} K_{ii,\text{loc}}^{(i_r)} dV_i \quad \text{no sum over } i \quad , \quad (5.32)$$

where $V^{(i)}$ is the volume of the spheroid. Corresponding averaged concentration tensors, ${}^0\bar{D}_{ij}^{(i_r)}$ as well as averaged gradient fields, $\bar{T}_i^{(i_r)}$, and flux fields, $\bar{q}_i^{(i_r)}$, can now be obtained from Eq. (5.4) and Eq. (4.2). If $\beta(\theta)$ satisfies the confocality condition, ${}^p\beta_{i,\text{loc}}$, of course, is constant, no integration needs to be carried out, and the exact solution is obtained.

It is worth noting that local dilute concentration tensors, $D_{ii,\text{loc}}^{(i_r)}$ and $D_{ii,\text{loc}}^{(i)}$, can be obtained from the reduced local conductivities, $K_{ii,\text{loc}}^{(i_r)}$, by using Eq. (5.30). $D_{ii,\text{loc}}^{(i_r)}$ and $D_{ii,\text{loc}}^{(i)}$ can provide valuable information on the fluctuations of the temperature gradient within the inclusion, such as the locations and magnitudes of the maximum and minimum temperature gradients.

Degenerate Spheroids The above averaging scheme simplifies considerably for inclusions that are cylinders ($a_1/a_2 \rightarrow \infty$) or infinitely thin discs ($a_1/a_2 \rightarrow 0$). In these cases the integration in Eq. (5.32) must be carried out only over dV_2 or dV_1 , respectively, and the conductivities in the other directions are not reduced by the thermal barriers. For the special case of a constant interface parameter, $\beta = \text{const.}$, no averaging is required for the above geometries as well as for spheres, as the confocality condition is fulfilled.

5.1.5 Results and Discussion

Results are presented for diamond (D) inclusions in a zinc sulfide (ZnS) matrix. A single spherical inclusion of radius $a = 2 \mu\text{m}$ is studied first. Subsequently investigations are extended to spheroids, the dimensions of which are chosen such that the smallest semi-axis measures $2 \mu\text{m}$. By doing so the same length scale is maintained for prolate and oblate spheroids. The interface parameter β is assumed to be constant on Γ_β corresponding to the case of a coating of constant thickness. Material properties are taken from ? and listed in Table 5.1. Spheroids with aspect ratios varying from 10^{-3} to 10^3 as well as cylinders

Table 5.1: Material properties of diamond inclusions (D) and of zinc sulfide matrix (ZnS) taken from ?.

Properties	D/ZnS
$K^{(i)}$	600 W/mK
$K^{(m)}$	17.4 W/mK
β	$\frac{1}{6} \times 10^8$ W/m ² K
a_{min}	2 μm

and discs are studied. Reduced conductivities, $\bar{K}_{ij}^{(ir)}$, are estimated, and the associated inclusion gradient fields are evaluated. Results are compared with those obtained from FE analyses as well as with Nan's EMA ?.

The FE models are built and solved with ANSYS 6.1 (ANSYS, Inc., Canonsburg, PA). Due to symmetry only one eighth of the inclusion volume and associated matrix volume needs to be modeled. The inclusion and the surrounding matrix material are meshed with 10-node tetrahedral elements, and at the outer perimeter the matrix block is extended with 15-node prisms, the resulting inclusion volume fraction being less than 0.5% in each case. The element edge length of the inclusion elements varies from approx. $1/7 a_2$ at the inclusion core to some $1/30 a_2$ at the interface as mesh refinement is carried out at the inclusion-matrix interface. The thermal interface is modeled with contact/target surface elements allowing for non-conformal meshes at the interfaces. Temperature boundary conditions corresponding to a uniform far field gradient of unit value are applied.

The FE results are evaluated in terms of standard deviations, $\sigma_i^{(i)}$, of the inclusion temper-

ature gradient field $T_{,i}^{(i)}$, which are given as

$$\sigma_i^{(i)} = \sqrt{\frac{1}{\sum_{(e)} V^{(e)}} \sum_{(e)} \left(\bar{T}_{,i}^{(i)} - T_{,i}^{(e)} \right)^2 V^{(e)}} \quad , \quad (5.33)$$

where $\bar{T}_{,i}^{(i)}$ is the average of the temperature gradient in the inclusion and $T_{,i}^{(e)}$ stands for the temperature gradient in element (e) of the inclusion, which has a volume of $V^{(e)}$. For cases where the confocality condition is violated, the standard deviations provide valuable information on the local fluctuations of the temperature gradient field within the inclusion.

Spherical Inclusions ($a_1 = a_2$)

For the case of spherical inclusions and a constant interface parameter β the confocality condition is satisfied, i.e. no averaging is required and the exact solution is obtained. The reduced inclusion conductivity is evaluated as $K^{(ir)} = 31.58$ W/mK and the reduced matrix conductivity is obtained as $K^{(mr)} = 8.51$ W/mK from Eqs. (5.23) and (5.24), respectively, for the material properties given in Table 5.1. Both reduced conductivity tensors remain isotropic. For the given material properties the critical particle radius equals $r_{cr} = 1.075$ μm , which is smaller the actual particle size, hence $K^{(ir)} > K^{(m)}$. In Fig. 5.5 the resulting temperature fields and associated temperature gradient fields of both the perfectly bonded configuration and the imperfectly bonded configuration are compared for the case of a uniform unit far field temperature gradient along the principal axes. The gradient fluctuations in the matrix material are much higher for the perfectly bonded case than for the imperfectly bonded case, due to the fact that the ratio of inclusion conductivity over matrix conductivity is much smaller for the latter case. In Fig. 5.6 the resulting temperature fields and associated temperature gradient fields of the two underlying auxiliary configurations are plotted.

Figure 5.7 shows the temperature distributions inside the inclusions, $T^{(i)}$ and $T^{(ir)}$ ($x_1 \leq 2$ μm), and in the matrix, $T^{(m)}$ and $T^{(mr)}$ ($x_1 \geq 2$ μm), along the x_1 -axis due to a uniform far field temperature gradient $T_{,1}^{(*)} = 1$ K/m. The solid line corresponds to the auxiliary configuration based on $K^{(ir)}$ and $K^{(m)}$, which leaves the matrix field unchanged, and the dashed line corresponds to the auxiliary configuration using $K^{(i)}$ and $K^{(mr)}$, which leaves the inclusion field unchanged. By restricting the results from the two configurations to their respective regions of validity the actual temperature fields inside and outside the inclusion are obtained. The temperature distribution along x_1 as predicted with the FE model (bullets) coincides with the analytical results. In Fig. 5.8 the behavior of the

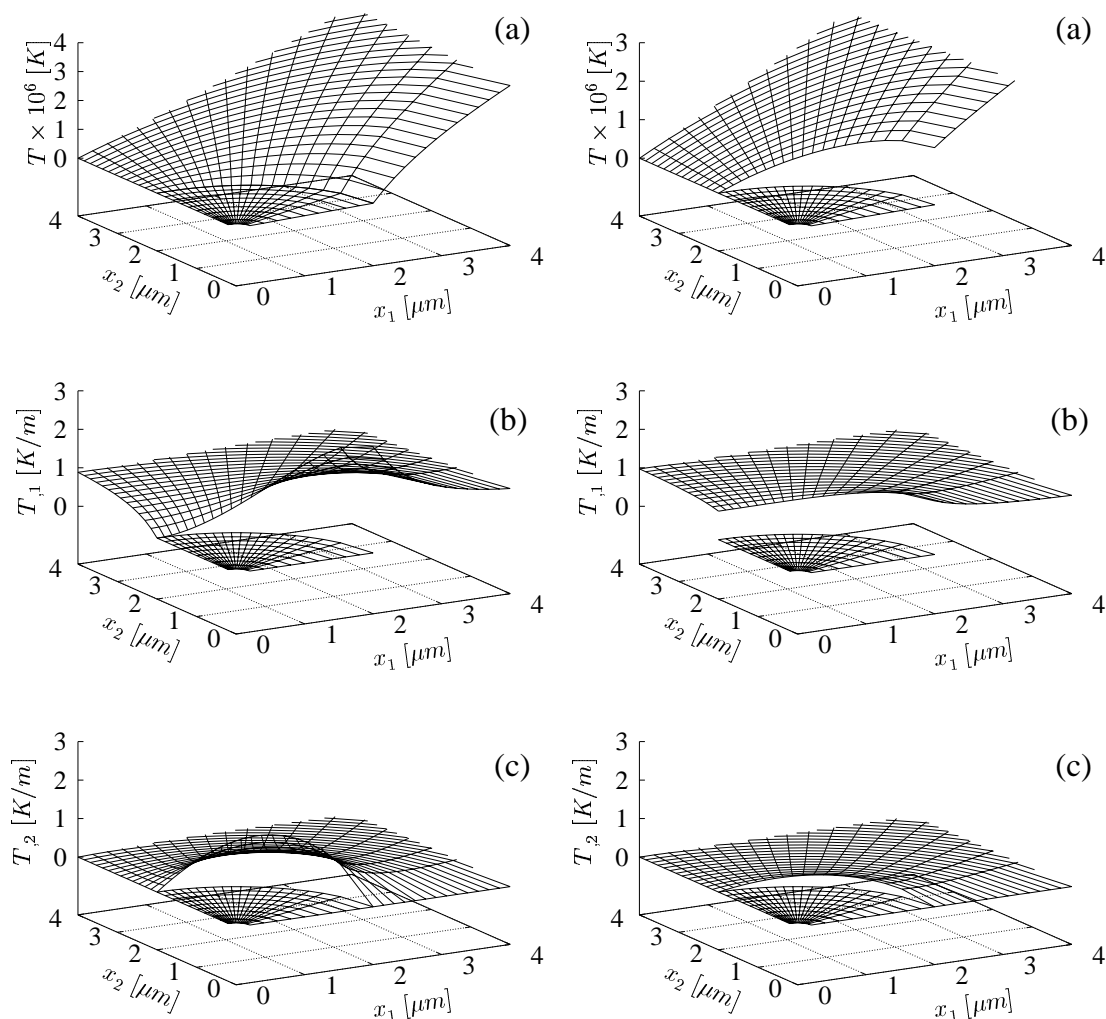


Figure 5.5: Temperature distributions (a) and the associated temperature gradients $T_{,1}$ (b) and $T_{,2}$ (c) in the x_1 - x_2 -plane for the investigated D/Zn-system for the case of a perfect thermal interface (left) and imperfect thermal interface (right) for a uniform far field gradient in x_1 -direction of unit value.

temperature gradients along x_1 is shown, their values being normalized with respect to the far field temperature gradient $T_{,1}^{(*)}$. In analogy to Fig. 5.7, $T_{,1}^{(m)}$ is indicated by a solid line and $T_{,1}^{(m_r)}$ by a dashed line in the matrix region. Both $T_{,1}^{(ir)}$ (solid line) and $T_{,1}^{(i)}$ (dashed line) can be seen to be constant within the inclusion and their normalized magnitudes correspond to the concentration factors ${}^0D_{11}^{(m,ir)}$ and ${}^0D_{11}^{(m_r,i)}$, respectively. The dilute concentration tensor for the replacement inclusion embedded in the original matrix material is ${}^0D_{ii}^{(m,ir)} = 0.786$ (no sum over i), which is about 20 times higher than that for the

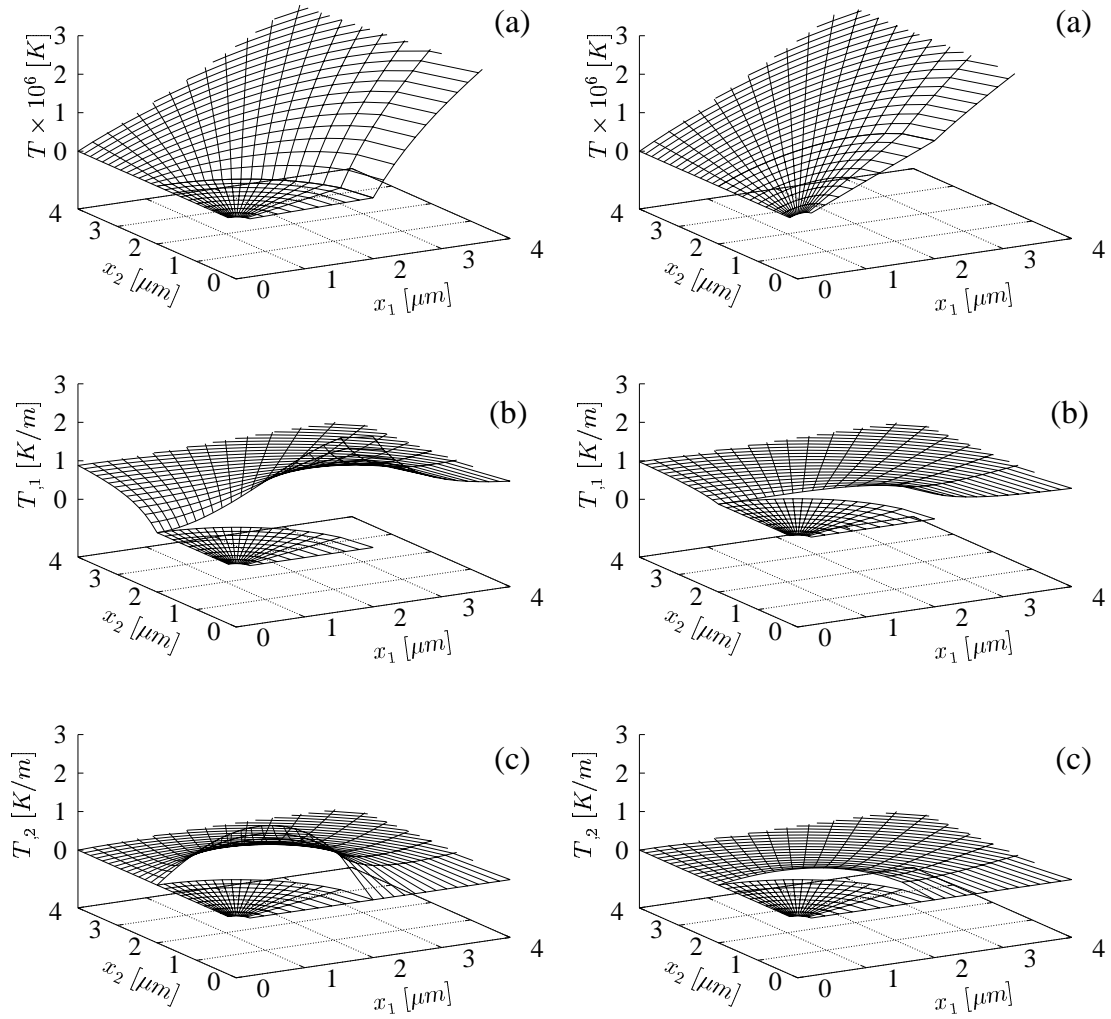


Figure 5.6: Temperature distributions (a) and the associated temperature gradients $T_{,1}$ (b) and $T_{,2}$ (c) in the x_1 - x_2 -plane for the investigated D/Zn-system for the case of auxiliary configuration $K^{(m_r,i)}$ (left) and the auxiliary configuration $K^{(m,i_r)}$ (right) for a uniform far field gradient in x_1 -direction of unit value.

actual inclusion. The nonzero components of the dilute concentration tensor for the actual inclusion are evaluated as ${}^0D_{ii}^{(m,i)} = 0.0414$ (no sum over i) from Eq. (5.30). Simulations with the FE model give a volume averaged gradient of $0.0414 T_{,1}^{(*)}$. The standard deviations of the temperature gradients in the aligned and normal directions are both of the order of $10^{-6} \times T_{,1}^{(*)}$, i.e. numerical zeros.

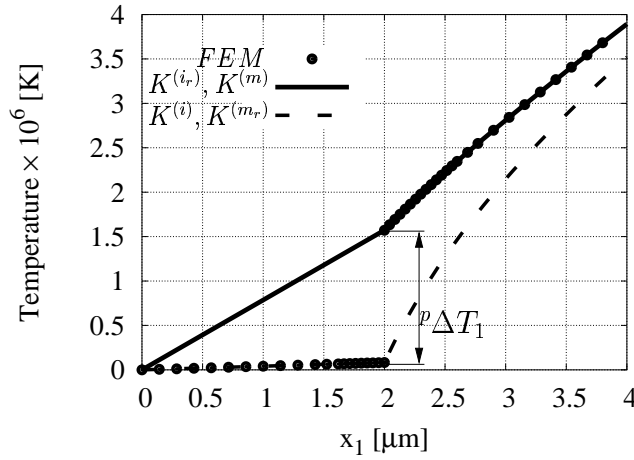


Figure 5.7: Temperature distributions along the x_1 -axis due to an applied far field gradient $T_{,1}^{(*)} = 1$ K/m in a single spherical diamond particle of radius $2 \mu\text{m}$ and the surrounding infinite zinc sulfide matrix in the presence of an interfacial thermal barrier of $\beta = \frac{1}{6} \times 10^8$ W/m²K. The solid and dashed lines show the temperature distributions corresponding to the two auxiliary configurations used by the proposed procedure and the bullets indicate the predictions of the FE model, which accounts for the interface resistance directly.

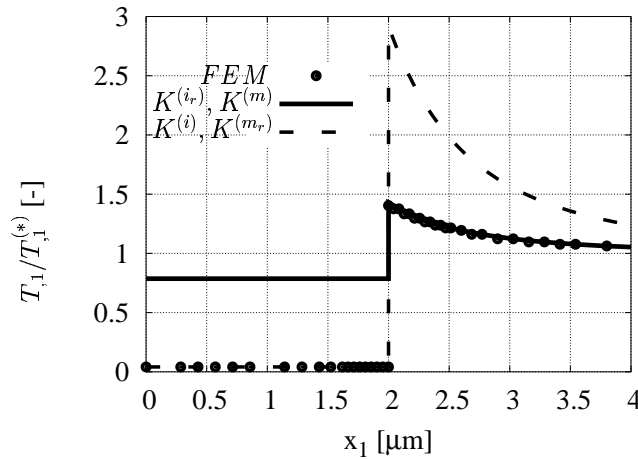


Figure 5.8: Normalized temperature gradients $T_{,1}^{(r)}/T_{,1}^{(*)}$ in a single diamond particle of radius $2 \mu\text{m}$ and in the surrounding infinite zinc-sulfide matrix in the presence of an interfacial thermal barrier of $\beta = \frac{1}{6} \times 10^8$ W/m²K. The solid and dashed lines show the temperature gradients corresponding to the two auxiliary configurations used by the proposed procedure and the bullets indicate the predictions of the FE model, which accounts for the interface resistance directly.

Spheroidal Inclusions ($a_1 \neq a_2$)

Figure 5.9(a) shows the influence of the aspect ratio on the reduced averaged conductivities of the replacement inclusions, $\bar{K}_{ij}^{(ir)}$, for a uniform interface parameter β and the material parameters given in Table 5.1. The solid line corresponds to the longitudinal conductivities, $\bar{K}_{11}^{(ir)}$, which increase as the aspect ratio increases (increasing interface conductance βa_1). For aspect ratios larger than 100 the reduced longitudinal conductivities almost equal the original inclusion conductivity of $K^{(i)} = 600$ W/mK. The dashed line shows the averaged transverse conductivities, $\bar{K}_{22}^{(ir)}$, which increase as the aspect ratio decreases (increasing interface conductance βa_2) and approach $K_{ij}^{(i)}$ for infinitely thin discs.

Uniform far field temperature gradients $T_{,i}^{(*)}$ of 1 K/m are applied and the resulting averaged temperature gradients in the perfectly bonded replacement inclusion are evaluated. In Fig. 5.9(b) the dependence on the aspect ratio is depicted for the normalized averaged thermal gradients $\bar{T}_{,1}^{(ir)}$ (bold solid line) and $\bar{T}_{,2}^{(ir)}$ (bold dashed line) under loading by unit temperature gradients in the x_1 - and x_2 -direction, respectively. For infinitely long cylindrical inclusions $\bar{T}_{,1}^{(ir)}$ tends towards $T_{,1}^{(*)}$, and $\bar{T}_{,2}^{(ir)}$ tends towards $T_{,2}^{(*)}$ for thin discs. The gradients in the actual inclusion, $\bar{T}_{,i}^{(i)}$, can be evaluated from Eq. (5.13) and are also plotted in Fig. 5.9(b) as thin lines. Both curves show mirror symmetric tendencies with respect to an aspect ratio of 1 which are also present for $\bar{K}_{ij}^{(ir)}$ and ${}^0S_{ij}$. The difference of the temperature gradients in the actual and the replacement inclusions (indicated by two arrows in Fig. 5.9(b)) together with the inclusions' dimensions is a measure for the temperature mismatch ΔT along the interface. The associated averaged fluxes, \bar{q}_1 and \bar{q}_2 , of both the actual inclusion and the replacement inclusion are shown in Fig. 5.9(c). Using Fourier's law the associated averaged inclusion flux fields can be reconstructed by the information given in Fig. 5.9(a) and Fig. 5.9(b) in two ways, $\bar{q}_i^{(ir)} = \bar{K}_{ii}^{(ir)} \bar{T}_{,i}^{(ir)} = \bar{K}_{ii}^{(i)} \bar{T}_{,i}^{(i)} = \bar{q}_i^{(i)}$ (no sum on i). Accordingly, as $\bar{K}_{ii}^{(i)}$ is constant the averaged fluxes shown in Fig. 5.9(c) are obtained by simply scaling $\bar{T}_{,i}^{(i)}$ in Fig. 5.9(b) by 600 W/mK.

When comparing geometrically identical inclusions, high inclusion conductivities generally give rise to small inclusion temperature gradients and vice versa. In contrast, with increasing averaged reduced conductivities, $\bar{K}_{ii}^{(ir)}$, the associated inclusion temperature gradients, $\bar{T}_{,i}^{(i)}$, increase as well. This is due to the influence of the aspect ratio on ${}^0S_{ij}$ which counteracts the influence of $\bar{K}_{ii}^{(ir)}$ as given in Eq. (5.23).

The components of dilute concentration tensors evaluated with Nan's EMA ?, from the FE model, and from the present method are compared in Table 5.2 for a number of aspect ratios. In addition the underlying reduced inclusion conductivities are given for the analytical methods and the standard deviations of the inclusion temperature field, $\sigma_i^{(i)}$, are

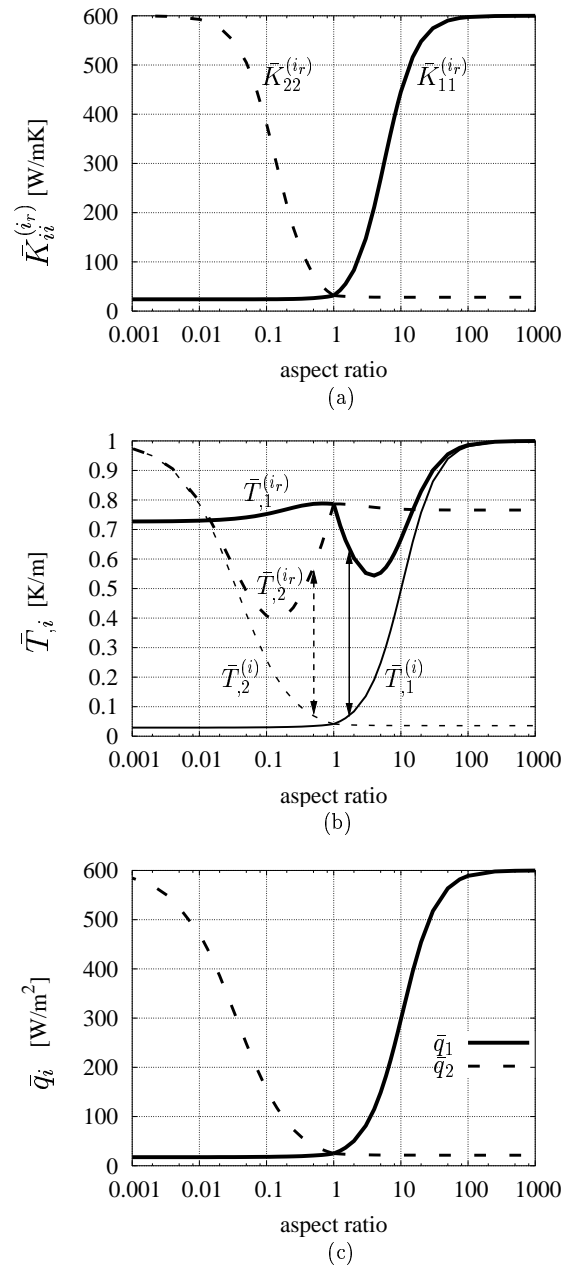


Figure 5.9: (a) Dependence of the reduced conductivities on the aspect ratio of spheroidal diamond inclusions (small semi-axis $2 \mu\text{m}$, uniform interface parameter $\beta = \frac{1}{6} \times 10^8 \text{ W/m}^2\text{K}$) embedded in a zinc sulfide matrix. The solid line shows the reduced longitudinal conductivity and the dashed line the reduced transverse conductivity. (b) Corresponding gradient fields in the actual inclusions, $(\bar{T}_{,i}^{(i)})$, and the replacement inclusions, $(\bar{T}_{,i}^{(i_r)})$, for a uniform far-field temperature gradient of unit value. (c) Corresponding inclusion flux fields, which are equal in the actual and the replacement inclusions.

Table 5.2: Comparison of the results obtained by the present method, by the FE models, and by Nan's EMA ? for a D/ZnS system with the material properties given in Table 5.1.

		present method		FE		EMA	
$\frac{a_1}{a_2}$	i	${}^0\bar{D}_{ii}^{(i)}$	$\bar{K}_{ii}^{(i_r)}$	${}^0\bar{D}_{ii}^{(i)}$	$\sigma_i^{(i)}$	${}^0\bar{D}_{ii}^{(i)}$	$\bar{K}_{ii}^{(i_r)}$
		[—]	[W/mK]	[—]	[—]	[—]	[W/mK]
0	1	0.029	31.6	—	—	0.029	31.6
	2	1	600	—	—	1	600
$\frac{1}{5}$	1	0.0312	24.4	0.0310	0.0027	0.0324	30.1
	2	0.1486	216.4	0.1472	0.0077	0.1261	144.8
$\frac{1}{2}$	1	0.0346	26.3	0.0344	0.0018	0.0362	30.0
	2	0.0691	72.5	0.0688	0.0021	0.0649	63.1
1	1	0.0414	31.6	0.0414	2.9×10^{-6}	0.0414	31.6
2	1	0.0838	83.4	0.0835	0.0039	0.0754	68.1
	2	0.0379	29.1	0.0379	0.0015	0.0388	30.6
5	1	0.2480	268.9	0.2467	0.0168	0.2018	186.9
	2	0.0364	28.2	0.0362	0.0026	0.0375	30.5
10	1	0.4954	445.7	0.4960	0.0302	0.4114	339.6
	2	0.0360	28.1	0.0358	0.0027	0.0373	30.7
∞	1	1	600	1	0.02×10^{-6}	1	600
	2	0.0374	31.6	0.0374	2.5×10^{-6}	0.0374	31.6

listed for the FE results. Excellent agreement is found between the results of the proposed method and the predictions of the FE model. In contrast Nan's EMA underestimates the temperature gradients induced by a uniform far field gradient parallel to the direction of the longer semi-axis and overestimates the induced gradients when $T_i^{(*)}$ is applied along the direction of the shorter semi-axis. Marked differences are found for the corresponding reduced inclusion conductivities as well. Only for the special cases of spheres, discs, and cylinders do the results of the EMA agree with those of the present method and the FE model.

For spheres and cylinders, where the gradient field within the inclusion is uniform for constant interface parameters, the standard deviations, Eq. (5.33), are less than 5×10^{-6} in terms of the applied far field thermal gradient, again indicating the satisfactory quality

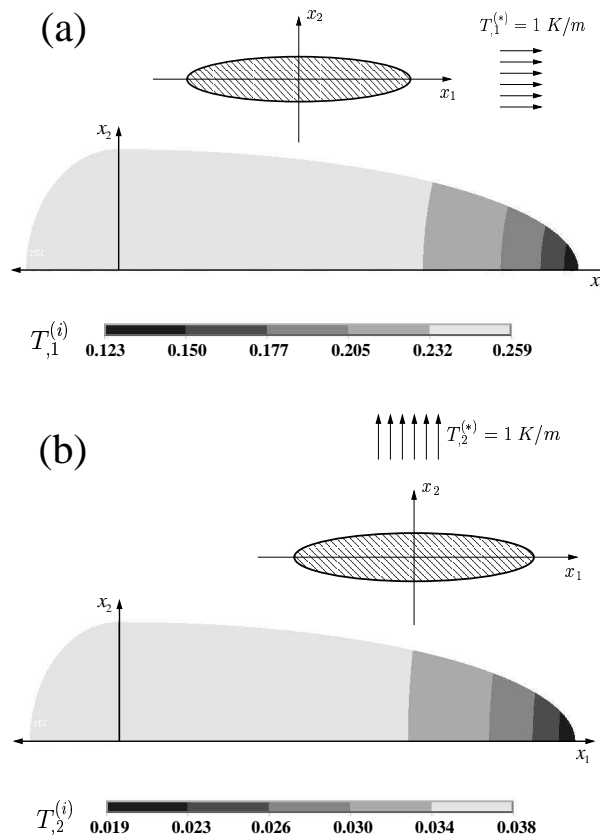


Figure 5.10: Contour plots of the temperature gradients within a spheroidal diamond inclusion ($K^{(i)} = 600 \text{ W/mK}$, aspect ratio 5) embedded in an infinite zinc sulfide matrix ($K^{(m)} = 17.4 \text{ W/mK}$) with an interfacial thermal resistance of $\beta = \frac{1}{6} \times 10^8 \text{ W/m}^2\text{K}$. (a) Axial temperature gradient $T_{,1}^{(i)}$ due to a unit far field gradient along x_1 , (b) Transverse temperature gradient $T_{,2}^{(i)}$ due to a unit far field gradient along x_2 .

of the FE mesh. For general spheroids where a constant interface parameter violates the confocality condition, the standard deviations $\sigma_i^{(i)}$ listed in Table 5.2 reach up to a few percent of the corresponding mean value of $T_{,i}^{(i)}$.

Figure 5.10(a) shows a contour plot of the inclusion gradient field $T_{,1}^{(i)}$ due to a unit far field temperature gradient $T_{,1}^{(*)}$ as calculated with the FE model and a corresponding result for a transverse unit far field gradient $T_{,2}^{(*)}$ is presented in Fig. 5.10(b). The aspect ratio of the spheroid shown is 5. A marked dependence of the inclusion temperature gradient fields on x_1 can be observed. It is noteworthy that both plots show variations of the respective temperature gradients along x_1 , the longer semi-axis. The gradients $T_{,1}^{(i)}$ due to $T_{,1}^{(*)}$ of unit

value, Fig. 5.10(a), are about an order of magnitude larger than the transverse gradients $T_{,2}^{(i)}$ due to $T_{,2}^{(*)}$ of unit value, Fig. 5.10(b).

In general the temperature gradients will always show variations along the longer semi-axis for constant interface parameters, with the minima located at the corresponding poles. Note that for confocal configurations the interface parameter is largest at the poles of the long semi-axis (${}^p\beta_{\max}$) and smallest at the poles of the short semi-axis (${}^p\beta_{\min}$) for both prolate and oblate inclusion shapes. Assuming ${}^p\beta_{\min} < \beta < {}^p\beta_{\max}$ a constant interface parameter β will accordingly reduce the heat flux in the regions of the poles of the longer semi-axis when compared to the heat flux which would result from the confocal variation and therefore cause a local gradient minimum there. Similar reasoning can be used to show that a local gradient maximum will be present in the regions of the poles of the shorter semi-axis for the case of a constant interface parameter.

As the proposed method allows for estimating minimum and maximum gradients and their location just inside Γ , a comparison with the FE results is carried out for an inclusion of aspect ratio of 5 as shown in Fig. 5.10. Employing the averaging scheme, Eq. (5.32), it is found that when evaluating $\bar{K}_{11}^{(i_r)}$ the local principal interface parameters vary from β at $(a_1, 0)$ to $\frac{a_1}{a_2}\beta$ at $(0, a_2)$ and when evaluating $\bar{K}_{22}^{(i_r)}$ the local principal interface parameters range between β at $(0, a_2)$ and $\frac{a_2}{a_1}\beta$ at $(a_1, 0)$. In Table 5.3 these minimum and maximum local principal interface parameters and their respective coordinates on Γ_β are given together with the corresponding reduced conductivities and dilute concentration tensors obtained with the present method. The proposed scheme correctly predicts the locations

Table 5.3: Comparison of minimum and maximum gradients as obtained with the proposed theory and the FE model for a spheroidal diamond inclusion of aspect ratio 5 with a constant interface parameter β for a unit temperature gradient $T_{,i}^{(*)}$.

	present method			FE	
i	${}^p\beta_{i,\text{loc}}$ for (x_1, x_2)	$K_{ii,\text{loc}}^{(i_r)}$	${}^0D_{ii,\text{loc}}^{(i)}$	${}^0D_{ii}^{(i)}$	
	[W/m ² K]	([m],[m])	[W/mK]	[—]	
1	β	$(a_1, 0)$	130.5	0.1595	0.1227
	$5 \times \beta$	$(0, a_2)$	348.8	0.2818	0.2594
2	$\frac{1}{5} \times \beta$	$(a_1, 0)$	6.59	0.0156	0.0186
	β	$(0, a_2)$	31.58	0.038	0.0383

of minimum and maximum temperature gradients. While good agreement is found for the estimated values of minimum and maximum temperature gradients in the transverse direction, the present theory somewhat overestimates the minimum and maximum gradients in longitudinal direction. This is due to larger variations of ${}^p\beta_{i,\text{loc}}$ (or the thickness of the corresponding coating) at the poles at $\pm a_1$ which violates the confocality condition more strongly than is the case at the poles at $\pm a_2$.

If the interface conductance is increased for a given inclusion size (which is equivalent to increasing the absolute inclusion size while not changing β) the reduced conductivities increase as well. The gain in $K_{11}^{(i_r)}$ is most pronounced for small aspect ratios and reduces to zero as the aspect ratio is increased ($K_{11}^{(i_r)}$ approaches $K_{11}^{(i)}$). Similar observations hold for the gain of $K_{22}^{(i_r)}$ which is very small for small aspect ratios but grows as the aspect ratio increases.

5.2 Non-ellipsoidal Inhomogeneities

In this section a numerical technique is proposed which allows to replace imperfectly bonded inclusions of arbitrary shape by perfectly bonded, but less conductive inclusions. The procedure is very much in the spirit of the analytical replacement operation for imperfectly bonded spheroids as outlined in the previous section (see also ?).

5.2.1 Introduction

In general, no analytical solutions are available for single inclusion problems, if the inclusion geometries are non-ellipsoidal, the conductivities are temperature dependent, or if imperfect thermal interfaces are present. In such cases numerical techniques must be employed for solving the underlying boundary value problems.

Work relating to this type of problem can be found in literature for the mechanical behavior of matrix inclusion systems. Adley and Taggart ? investigated solitary spheroidal inclusions in an elasto-plastic matrix material, introducing dilute incremental strain concentration tensors. Gilormini and Michel ? evaluated concentration tensors for the deviatoric stress of dilutely dispersed spheres embedded in a viscous power-law matrix. Bradshaw, Fisher and Brinson ? computed dilute elastic strain concentration tensors of single infinitely long sinusoidal fibers and subsequently employed a Mori-Tanaka scheme for non dilute estimates. To the author's knowledge no corresponding work has been published for problems obeying the Laplace Equation, i.e. heat conduction, electrical conduction, magnetic permeability, and dielectric permeability.

5.2.2 Imperfectly Bonded Inclusions

An imperfectly bonded inclusion embedded in an infinite matrix material of isotropic conductivity is considered. The temperature field is taken to satisfy the Laplace equation in the whole domain, implying steady state conditions, temperature-independent conductivities as well as the absence of heat sources (see Section 4.1).

An interfacial thermal resistance may be present between matrix and inclusion, see Fig. 5.11. The temperature discontinuity at the interface Γ_β is tied to the flux across the interface according to Eq. (5.20), the continuity of the flux being maintained.

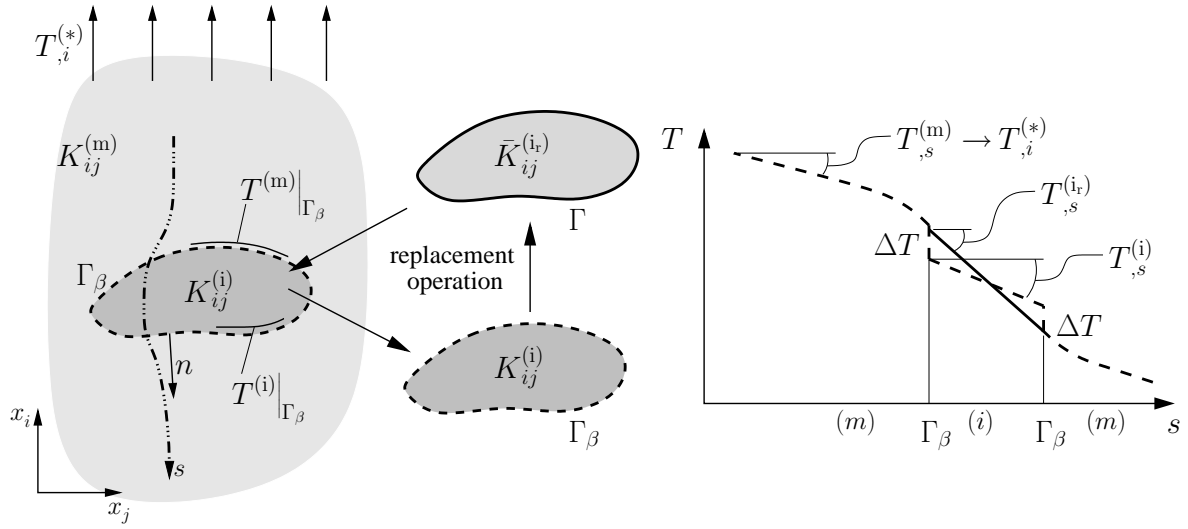


Figure 5.11: Sketch of an imperfectly bonded inclusion (conductivity $K_{ij}^{(i)}$) embedded in an infinite isotropic matrix material (conductivity $K^{(m)}\delta_{ij}$) and of the replacement operation that introduces a perfectly bonded inclusion (reduced conductivity $\bar{K}_{ij}^{(ir)}$) which attracts the same averaged flux field as the imperfectly bonded inclusion (left). The temperature along a path of heatflow is depicted showing characteristic temperature jumps at the interface Γ_β (right).

The *phase* averaged temperature gradient of the inclusion as defined by Eq. (2.1) reads

$$\bar{T}_{,i}^{(i)} = \frac{1}{V^{(i)}} \int_{V^{(i)}} T_{,i}^{(i)}(\vec{x}) dV = \frac{1}{V^{(i)}} \int_{\Gamma} T^{(i)}|_{\Gamma} n_i d\Gamma \quad , \quad (5.34)$$

where $V^{(i)}$ is the volume of the inclusion and the bar indicates a volume averaged quantity. Furthermore in Eq. (5.34) the divergence theorem is used to express the volume averaged temperature gradient in terms of the temperature distribution $T|_{\Gamma}$ at the interface Γ , with n_i being the unit normal vector on Γ pointing into the matrix phase.

The *phase* average of the heat flux in the inclusion, $\bar{q}_i^{(i)}$, can be expressed in analogy to Eq. (2.2) as

$$\bar{q}_i^{(i)} = \frac{1}{V^{(i)}} \int_{V^{(i)}} q_i^{(i)}(\vec{x}) dV = \frac{1}{V^{(i)}} \int_{\Gamma} q_j n_j x_i d\Gamma \quad , \quad (5.35)$$

and it is linked to the phase averaged temperature gradient by the inclusion conductivity $K_{ij}^{(i)}$ according to Fourier's law, Eq. (4.2).

Due to the temperature jump ΔT at the interface the volume averaged temperature gradient, $\bar{T}_{,i}^{(i)}$, is different from the ‘‘apparent’’ averaged temperature gradient, $\bar{T}_{,i}^{(ir)}$, which

accounts for the interfacial temperature discontinuities and is given as

$$\bar{T}_{,i}^{(i_r)} = \bar{T}_{,i}^{(i)} + \frac{1}{V^{(i)}} \int_{\Gamma} \left(T^{(m)}|_{\Gamma_{\beta}} - T^{(i)}|_{\Gamma_{\beta}} \right) n_i \, d\Gamma \quad . \quad (5.36)$$

Equation (5.36) is equivalent to the expression derived by Benveniste and Miloh ? for the apparent temperature gradient of a composite body with imperfectly bonded constituents. Comparing Eq. (5.36) with Eq. (5.34) shows that the apparent averaged temperature gradient of the replacement inclusion is fully determined by the interfacial temperatures of the matrix, $T^{(m)}|_{\Gamma_{\beta}}$, i.e.

$$\bar{T}_{,i}^{(i_r)} = \frac{1}{V^{(i)}} \int_{\Gamma} T^{(m)}|_{\Gamma_{\beta}} n_i \, d\Gamma \quad . \quad (5.37)$$

Note that $\bar{q}_i^{(i_r)}$ equals $\bar{q}_i^{(i)}$, as the continuity of the fluxes across the interface is maintained and therefore their averages remain the same.

Once averaged temperature gradients $\bar{T}_{,i}^{(i)}$ and $\bar{T}_{,i}^{(i_r)}$ due to uniform far fields $T_{,j}^{(*)}$ are evaluated, dilute concentration tensors ${}^0\bar{D}_{ij}^{(i)}$ and ${}^0\bar{D}_{ij}^{(i_r)}$ can be introduced, linking the inclusion fields to the far fields, Eq. (4.30).

5.2.3 Apparent Conductivities

It is instructive to consider the temperature distribution along a “trajectory” of the heat flux, as schematically depicted in Fig. 5.11 by a dashed–dotted line. The dashed line in the generic temperature vs. position diagram indicates the actual temperature variation along s in the presence of imperfect interfaces. At large distances from the inclusion the local temperature gradient in the matrix approaches the far field gradient, $T_{,i}^{(*)}$. The temperature gaps at the interface Γ_{β} are clearly evident; according to Eq. (5.20) they are proportional to the flux across the interface. Within the inclusion, the temperature distribution that corresponds to the apparent gradient and accordingly includes the effects of the temperature jumps at the interfaces, is shown as a solid line. Figure 5.11 also provides a qualitative picture for the size effect mentioned in Section 5.1: With decreasing size of the inclusion the effects of interfacial temperature jumps on the apparent thermal gradient, $\bar{T}_{,i}^{(i_r)}$, increase until they totally overwhelm the inclusion’s contribution $\bar{T}_{,i}^{(i)}$.

The replacement operation is motivated by Eq. (5.20), which states that the heat flux is continuous across the interface. Accordingly, the volume averaged flux of the original inclusion and that of the replacement inclusion equal, $\bar{q}_i^{(i)} = \bar{q}_i^{(i_r)}$. This flux balance can be

recast by using Eqs. (4.2) and (5.13) to give

$$K_{ik}^{(i)} {}^0\bar{D}_{kj}^{(i)} = \bar{K}_{ik}^{(ir)} {}^0\bar{D}_{kj}^{(ir)} \quad , \quad (5.38)$$

compare also Eq. (5.21). The reduced conductivity can be treated like a phase averaged quantity and can be determined once ${}^0\bar{D}_{ij}^{(i)}$ and ${}^0\bar{D}_{ij}^{(ir)}$ have been evaluated. Note that Eq. (5.38) is based on volume averages, so that the perfectly bonded replacement inclusion usually does not give rise to exactly the same matrix temperatures at and close to the interface as does the imperfectly bonded inclusion.

5.2.4 Some Remarks

Approximations of the dilute concentration tensors, ${}^0\bar{D}_{ij}^{(i)}$ and ${}^0\bar{D}_{ij}^{(ir)}$, can be obtained by means of any method that provides estimates of the interfacial temperatures $T^{(m)}|_{\Gamma_\beta}$ and $T^{(i)}|_{\Gamma_\beta}$ and allows for modeling sufficiently large matrix volumes so the set up can be treated as “dilute” for practical purposes. Choices that fulfill the two requirements are typical engineering methods such as the FEM or Boundary Element Methods.

Note that the conductivity of the replacement inclusion can be unsymmetric in cases where the inclusion shape, the distribution of the interface parameter, and the (anisotropic) material behavior do not share the same axes of symmetry. Because physically meaningful conductivity tensors must be symmetric ?, the interpretation and role of the apparent conductivity of inhomogeneities with imperfect interfaces require some comment.

The root of the violation of the symmetry of $K_{ij}^{(i)}$ lies in Eq. (5.38), where the averaged flux in the actual inclusion, $\bar{q}_i^{(i)}$, is related to a possibly incompatible averaged gradient field $\bar{T}_{,i}^{(ir)}$ to give

$$\bar{q}_i^{(i)} = -\bar{K}_{ij}^{(ir)} \bar{T}_{,j}^{(ir)} \quad . \quad (5.39)$$

For Eq. (5.39) to be satisfied, an unsymmetric $\bar{K}_{ij}^{(ir)}$ may be required.

This behavior, however, does not contradict physically reasonable behavior because $\bar{K}_{ij}^{(ir)}$ is shorthand for the expression $K_{ik}^{(i)} {}^0\bar{D}_{kl}^{(i)} {}^0\bar{D}_{lj}^{(ir)-1}$, compare Eq. (5.38), and describes heat transport processes that may be more complex than heat diffusion through a homogeneous solid. Note that — even though $\bar{K}_{ij}^{(ir)}$ in general is not symmetric — symmetry relations of general nature, which are discussed in the following section, still are satisfied.

5.3 Symmetry Relations

Phase averaged temperature gradient concentration tensors are not necessarily symmetric, i.e. $\bar{D}_{ij} \neq \bar{D}_{ji}$ in general. By arguing along the same lines as in ? it can be proven, however, that the expressions $(K_{ij}^{(i)} - K_{ij}^{(m)})^0 \bar{D}_{jk}^{(i)}$ for perfectly bonded inclusions and $(K_{ij}^{(ir)} - K_{ij}^{(m)})^0 \bar{D}_{jk}^{(ir)}$ for perfectly bonded replacement inclusions must always be symmetric, provided the corresponding dilute concentration tensors are exact.

For the proof a heterogeneous body of volume V of conductivity $K_{ij}(x_i)$ and imperfectly bonded constituents which is sequentially subjected to two different temperature fields on its external surface Γ denoted by $T^{(*)}|_{\Gamma}$ and $\acute{T}^{(*)}|_{\Gamma}$, respectively, is considered. The exact temperature distributions within the body are denoted by $T(x_i)$ and $\acute{T}(x_i)$, and the associated local fields are denoted by $T_{,i}(x_i)$, $\acute{T}_{,i}(x_i)$ and $q_i(x_i)$, $\acute{q}_i(x_i)$.

The reciprocal theorem (see ? for elasticity) states that

$$\int_V q_i(\vec{x}) \acute{T}_{,i}(\vec{x}) dV = \int_V \acute{q}_i(\vec{x}) T_{,i}(\vec{x}) dV \quad , \quad (5.40)$$

and by using Fourier's law (Eq. (4.2)) can be recast into

$$\int_V K_{ij}(\vec{x}) T_{,j}(\vec{x}) \acute{T}_{,i}(\vec{x}) dV = \int_V K_{ij}(\vec{x}) \acute{T}_{,j}(\vec{x}) T_{,i}(\vec{x}) dV \quad . \quad (5.41)$$

Equation (5.41) shows that the reciprocal theorem only holds for symmetric conductivities¹ i.e. $K_{ij}(\vec{x}) = K_{ji}(\vec{x})$.

If, and only if, the boundary conditions are *homogeneous* Eq. (5.40) can be expressed in terms of phase averaged quantities ?, yielding

$$q_i^{(*)} \acute{T}_{,i}^{(*)} = \acute{q}_i^{(*)} T_{,i}^{(*)} \quad . \quad (5.42)$$

The volume averaged fluxes and the total averaged temperature gradients (including contributions due to interfacial temperature gaps) can be split into phase averaged contributions ?

$$q_i^{(*)} = (1 - \xi) \bar{q}_i^{(m)} + \xi \bar{q}_i^{(i)} \quad , \quad (5.43)$$

$$T_{,i}^{(*)} = (1 - \xi) \bar{T}_{,i}^{(m)} + \xi \bar{T}_{,i}^{(i)} + \frac{1}{V} \int_{\Gamma} \Delta T|_{\Gamma\beta} n_i d\Gamma \quad , \quad (5.44)$$

$$= (1 - \xi) \bar{T}_{,i}^{(m)} + \xi \bar{T}_{,i}^{(ir)} \quad , \quad (5.45)$$

¹If a_i and b_i are two first rank tensors, then $K_{ij} a_i b_j = K_{ij} a_j b_i$ is only fulfilled, if $K_{ij} = K_{ji}$.

Equation (5.43) allows to recast Eq. (5.42) into the following form

$$\left[(1 - \xi) \bar{q}_i^{(m)} + \xi \bar{q}_i^{(i)} \right] \hat{T}_{,i}^{(*)} = \left[(1 - \xi) \hat{q}_i^{(m)} + \xi \hat{q}_i^{(i)} \right] T_{,i}^{(*)} \quad , \quad (5.46)$$

and expressing the phase averaged fluxes by the respective conductivities and gradients (Fourier's law) gives

$$- \left[(1 - \xi) K_{ij}^{(m)} \bar{T}_{,j}^{(m)} + \xi K_{ij}^{(i)} \bar{T}_{,j}^{(i)} \right] \hat{T}_{,i}^{(*)} = - \left[(1 - \xi) K_{ij}^{(m)} \hat{T}_{,j}^{(m)} + \xi K_{ij}^{(i)} \hat{T}_{,j}^{(i)} \right] T_{,i}^{(*)} \quad (5.47)$$

Finally, the mean field relations (Eq. (5.45)) are used again, by replacing $(1 - \xi) \bar{T}_{,i}^{(m)}$ with $T_{,i}^{(*)} - \xi \bar{T}_{,i}^{(i_r)}$. Additionally $\bar{T}_{,i}^{(i)}$ and $\bar{T}_{,i}^{(i_r)}$ are replaced by ${}^0\bar{D}_{ij}^{(i)} T_{,j}^{(*)}$ and ${}^0\bar{D}_{ij}^{(i_r)} T_{,j}^{(*)}$, respectively. The following relation is then obtained for the left hand side of Eq. (5.47)

$$-K_{ij}^{(m)} \hat{T}_{,i}^{(*)} T_{,j}^{(*)} - \xi \left(K_{ij}^{(i)} {}^0\bar{D}_{jk}^{(i)} - K_{ij}^{(m)} {}^0\bar{D}_{jk}^{(i_r)} \right) T_{,k}^{(*)} \hat{T}_{,i}^{(*)} \quad (5.48)$$

and for the right hand side of Eq. (5.47)

$$-K_{ij}^{(m)} T_{,i}^{(*)} \hat{T}_{,j}^{(*)} - \xi \left(K_{ij}^{(i)} {}^0\bar{D}_{jk}^{(i)} - K_{ij}^{(m)} {}^0\bar{D}_{jk}^{(i_r)} \right) \hat{T}_{,k}^{(*)} T_{,i}^{(*)} \quad (5.49)$$

Comparing the right hand terms of Eqs. (5.48) and (5.49) reveals that the tensorial expression $(K_{ik}^{(i)} {}^0\bar{D}_{kj}^{(i)} - K_{ik}^{(m)} {}^0\bar{D}_{kj}^{(i_r)})$ must be diagonally symmetric. For the case of perfectly bonded constituents ${}^0\bar{D}_{ij}^{(i_r)}$ equals ${}^0\bar{D}_{ij}^{(i)}$ and the symmetry condition reduces to $(K_{ik}^{(i)} - K_{ik}^{(m)}) {}^0\bar{D}_{kj}^{(i)}$, which for the elastic case is derived in ?. For the case of imperfectly bonded constituents the symmetry condition can be reduced to $(\bar{K}_{ik}^{(i_r)} - K_{ik}^{(m)}) {}^0\bar{D}_{kj}^{(i_r)}$, using Eq. (5.38).

Chapter 6

Some Results for Single Inclusion Problems

Even though the ellipsoid is a versatile geometry, covering the range from thin discs to long cylinders, for many configurations the approximation of actual inclusions by means of ellipsoidal inclusion shapes is not satisfactory. For the investigated carbon–copper composite a typical fiber has a circular cross–section of constant size and is perfectly straight and chopping as well as fiber breaking during the hot pressing process leaves end faces at right angles to the fiber axis (Figs. 3.1 and 3.4). Because of the moderate fiber aspect ratios (Fig. 3.3) cylinders describe the actual fiber shape much better than spheroids of the same aspect ratio.

In this chapter single, transversally isotropic cylinders embedded in an isotropic matrix material of infinite extent are considered. Averaged dilute concentration tensors are evaluated for the case of perfectly bonded cylinders. A parametric study is carried out on the influence of the cylinders' aspect ratios and the conductivities of the configuration. The results are provided in terms of shape factor functions, indicating the deviation of the averaged concentration tensor of a cylinder from the concentration tensor of a spheroidal inclusion that has the same aspect ratio (a_1/a_2), volume, and conductive properties. The latter is referred to as the “corresponding spheroid”. For the case of imperfectly bonded cylinders, averaged reduced conductivities and the corresponding averaged dilute concentration tensors (see Section 5.2) are estimated for the specific case of carbon fibers in a copper matrix (see Chapter 3 for material data).

6.1 Perfectly Bonded Cylinders

A single cylinder in an infinite matrix subjected to homogeneous far field gradients is considered. Finding the local temperature fields, $T^{(i)}(x_i)$ and $T^{(m)}(x_i)$, and the associated microfields poses a sophisticated boundary value problem. It requires solving three second order differential equations of coupled non constant coefficients, for which Bessel functions are needed. No exact analytical solutions have been given yet. Approximate solutions are derived in [?] for a far field gradient applied along the cylinder axis. That solution applies only for the specific case of isotropic cylinders embedded in matrix materials of lower conductivity, furthermore a fit parameter is required.

In the following the FEM is used to solve the three dimensional boundary value problem from above and a parametric study is carried out. Cylinder with aspect ratios of 1, 2, 5, 10, and 15 are investigated. The studied ratios of axial fiber conductivity over matrix conductivity, $K_{11}^{(i)}/K^{(m)}$, range from 0.01 to 100. Three different ratios of axial fiber conductivity over transverse fiber conductivity are studied, isotropic fibers ($K_{11}^{(i)} = K_{22}^{(i)}$), $K_{11}^{(i)}/K_{22}^{(i)} = 10$, and $K_{11}^{(i)}/K_{22}^{(i)} = 100$. The chosen parameters cover a wide range of technically relevant composite materials. If results are desired of a configuration that does not match any of the investigated set of parameters, interpolation can be used.

6.1.1 Shape Factor Tensor

The results are given in terms of a cylinder–spheroid shape factor tensor, \bar{e}_{ij}^c , which is defined as

$$\bar{T}_{,i}^{(ic)} = \bar{e}_{ij}^c T_{,j}^{(is)} \quad , \quad (6.1)$$

where $\bar{T}_{,i}^{(ic)}$ and $\bar{T}_{,i}^{(is)}$ are the phase averaged temperature gradient fields due to an applied far field gradient $T_{,i}^{(*)}$ in cylinders and corresponding spheroids, respectively. The off-diagonal terms of this shape factor tensor are zero, i.e. $\bar{e}_{ij}^c = 0$ for $i \neq j$. From Eq. (6.1) the relationship between the averaged dilute concentration tensor of a cylindrical inclusion, ${}^0\bar{D}_{ij}^{(ic)}$, and that of a corresponding spheroid, ${}^0D_{ij}^{(is)}$, can be written as

$${}^0\bar{D}_{ij}^{(ic)} = \bar{e}_{ik}^c {}^0D_{kj}^{(is)} \quad , \quad (6.2)$$

where ${}^0D_{ij}^{(is)}$ is given by Eq. (5.4). For the case of a perfect thermal interface the inclusion size does not influence the concentration tensors and the fiber geometry enters \bar{e}_{ii}^c only via the fiber aspect ratio. Note also that only the "contrast" between the conductivities of

inclusion and matrix, $K_{ij}^{(i)}/K_{ij}^{(m)}$ (no sum on i and j), influences the concentration tensors, but the absolute values of the conductivities do not.

6.1.2 Results and Discussion

The studied configurations are axisymmetric and therefore the shape factor tensors have transversally isotropic symmetry, i.e. $\bar{e}_{11}^c \neq \bar{e}_{22}^c = \bar{e}_{33}^c$. The evaluated entries of the shape factor tensors are presented graphically in Fig. 6.1. The three graphs on the left column of Fig. 6.1 show the axial shape factors, \bar{e}_{11}^c , for the three investigated cases of transversal isotropy of the inclusion material. The graphs on the right hand side in Fig. 6.1 pertain to the corresponding radial shape factors, \bar{e}_{22}^c .

Axial Shape Factor

The behavior of the axial shape factor, \bar{e}_{11}^c , when plotted as functions of the conduction contrast $K_{11}^{(i)}/K^{(m)}$ can be divided in two distinctive regions (left column, Fig. 6.1). If the axial conductivity of the inclusion $K_{11}^{(i)}$ is smaller than the matrix conductivity the averaged temperature gradients of cylinders are larger than those of the corresponding spheroids, $\bar{T}_{,1}^{(i_c)} > T_{,1}^{(i_s)}$. The shape factors in this range are less than 1.1 for all investigated cases and only a minor dependence of the shape factors on the fiber's anisotropy described by $K_{11}^{(i)}/K_{22}^{(i)}$ is observed. It is worth noting that the largest deviation of the axial temperature gradient of cylinder and corresponding spheroid is observed for an aspect ratio of approximately $a_1/a_2 = 2$.

If the axial conductivity of the fiber exceeds the matrix conductivity, $K_{11}^{(i)} > K^{(m)}$, a pronounced dependence of the axial shape factor on the aspect ratio a_1/a_2 , on the anisotropy of the inclusion, $K_{11}^{(i)}/K_{22}^{(i)}$, and on the conductive contrast is evident. This behavior of the axial shape factor can be interpreted in terms of two counteracting effects (Fig. 6.2). The end faces of the cylinder are oriented perpendicularly to the applied far field gradient, $T_{,1}^{(*)}$, and therefore capture a larger heat flux than do corresponding spheroids. Especially for small aspect ratios this end face effect dominates and the axial temperature gradients in the cylinders are larger than those of in the corresponding spheroids. With increasing aspect ratio the relative area of the end face (in terms of total surface area) decreases. Accordingly the importance of the end face effect decreases, too, while at the same time the heat exchange via the side faces becomes more important. In the case of cylinders the heat which is entering/leaving via the side faces must be transported radially towards

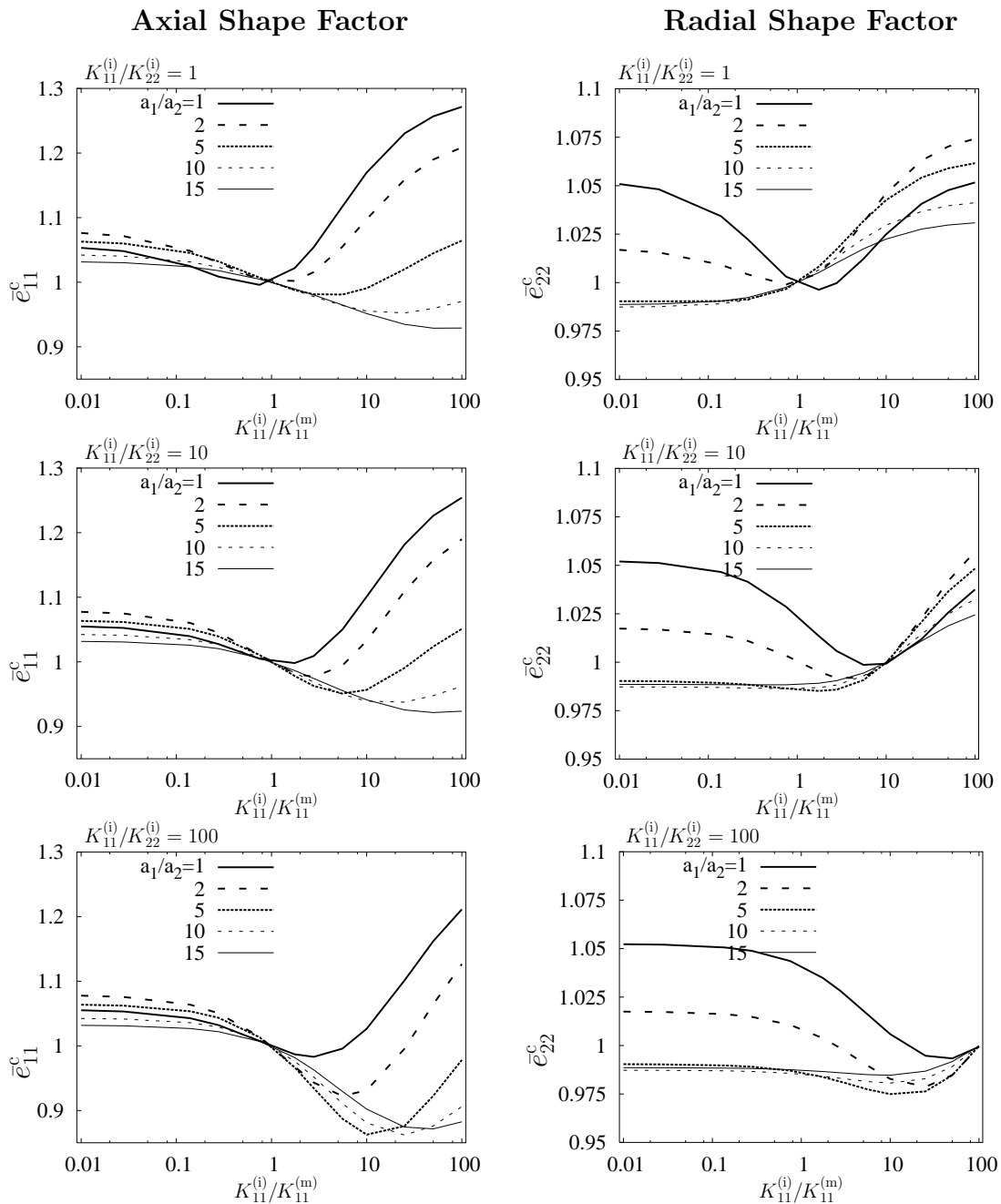


Figure 6.1: Axial shape factor \bar{e}_{11}^c (left) and radial shape factor \bar{e}_{22}^c (right) for cylindrical fibers of conduction anisotropies $K_{11}^{(i)}/K_{22}^{(i)} = 1, 10, \text{ and } 100$ plotted over the conductive contrast $K_{11}^{(i)}/K_{11}^{(m)}$. The curves are parameterized with respect to the fiber aspect ratio a_1/a_2 , which takes the values of 1, 2, 5, and 10.

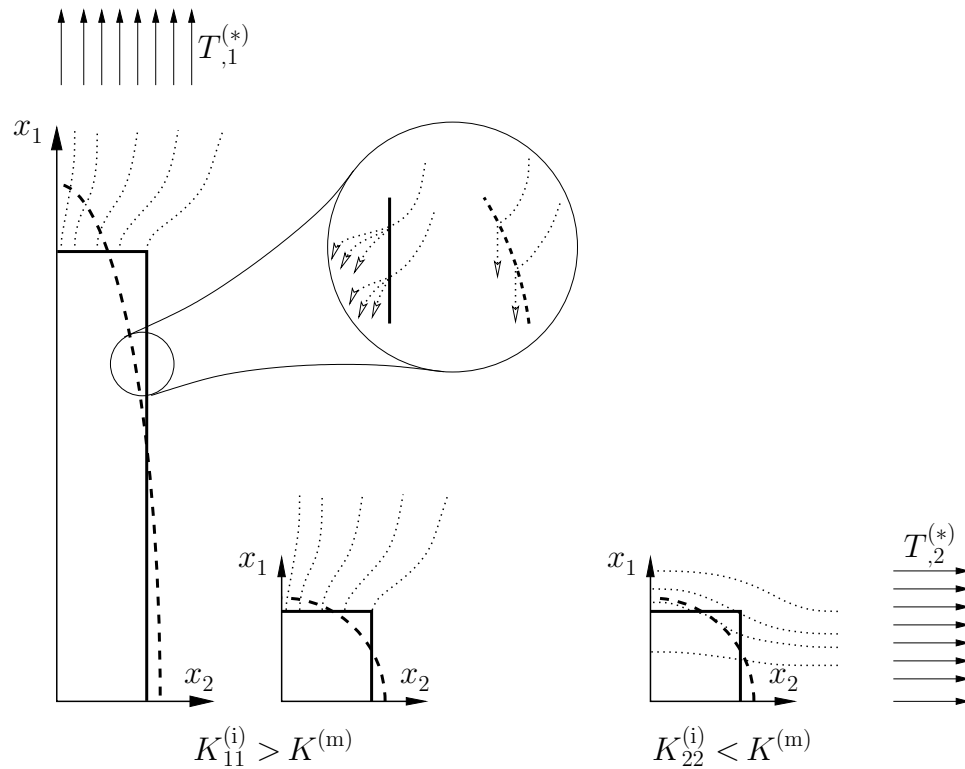


Figure 6.2: Sketch of two cylinders with $K_{11}^{(i)} > K^{(m)}$ subjected to an axial far field gradient indicating that their end faces capture a larger heat flux than the ends of a spheroids of equal volume, aspect ratio, and conduction properties (left). Sketch of a cylinder with $K_{22}^{(i)} < K^{(m)}$ subjected to a transverse far field gradient indicating that heat can leave the resistive cylinder through the end face (right).

the inclusion core/side face in order to exploit the whole axial cross section for flowing axially inside the fiber (Fig. 6.2). Accordingly, small transverse inclusion conductivities yield small averaged axial gradients when compared to corresponding spheroids. Note that for spheroidal inclusion geometries the transversal conductivity has no influence on axial temperature gradients ? as the Eshelby property holds.

Radial Shape Factors

The deviations between averaged temperature fields of cylinders and those of corresponding spheroids for applied far field gradients in transverse direction, $T_{,2}^{(*)}$, are less pronounced compared to the axial case (right column, Fig. 6.1). If the transverse conductivity of a cylinder, $K_{22}^{(i)}$, is lower than that of the matrix material there is almost no dependence of the

radial shape factors, \bar{e}_{22}^s , on the aspect ratio for aspect ratios greater than five. However for smaller aspect ratios, a marked dependence is observed. Once again, two mechanisms can be invoked for an explanation. Heat entering the transversely poorly conducting cylinders through the side face can leave the cylinder through the end face to reach the less resistive matrix material. The influence of this effect, again, goes in hand with the fraction of the end face of the total surface. Due to this mechanism composites reinforced by cylindrical discs will exhibit superior conductive performance when compared to a composite made up of corresponding spheroids. For intermediate aspect ratios larger gradients are induced in resistive cylinders than in corresponding spheroids. This is due to a shape driven end face effect as the needle-like end face regions of spheroids lead to lower resistivities compared to cylinders. If the aspect ratio is increased further, end face effects become less dominant and the radial shape factors function approaches unity from below.

Some Remarks on the Shape Factor Tensor

Shape factors greater than unity indicate that cylinders “attract more heat” than corresponding spheroids, i.e. $\bar{T}_{,i}^{(i_c)} > T_{,i}^{(i_s)}$, and accordingly cylinders show better conductive performance than corresponding spheroids. However, comparing two geometrically identical inclusions of different conductivity, $K_{ij}^{(i_1)} > K_{ij}^{(i_2)}$, shows that larger gradients are induced in the inclusion of lower conductivity, i.e. $\bar{T}_{,i}^{(i_2)} > \bar{T}_{,i}^{(i_1)}$. Nevertheless, inclusion i_1 performs better than inclusion i_2 .

This apparent paradox can be easily resolved by noting that for assessing and comparing various inclusions with respect to heat conduction the concentration tensors and conductivities may not be studied isolated. The product $D_{ik}^{(i)} K_{kj}^{(i)}$ determines the conductive properties of inclusions with respect to each other (compare also Eq. (4.22)).

Finite Element Results

In Figs. 6.3 to 6.5 the results pertaining to $K_{11}^{(i)}/K_{22}^{(i)} = 1, 10, \text{ and } 100$ are collected. The plots give insight into how spheroids behave (compare Eq. (5.4)) for the chosen range of parameters. Additionally the results of the unit cell calculations and the shape factors are provided. The results are organized in three sets corresponding to the three investigated ratios of $K_{11}^{(i)}/K_{22}^{(i)}$ (top left of each diagram) and each set consists of five diagrams relating to the five discrete aspect ratios (top right of each diagram). The horizontal axis shows the conductive contrast $K_{11}^{(i)}/K^{(m)}$. The vertical axis on the left relates to averaged inclusion

gradients due to far field gradients of unit value and the vertical axis on the right relates to the shape factors.

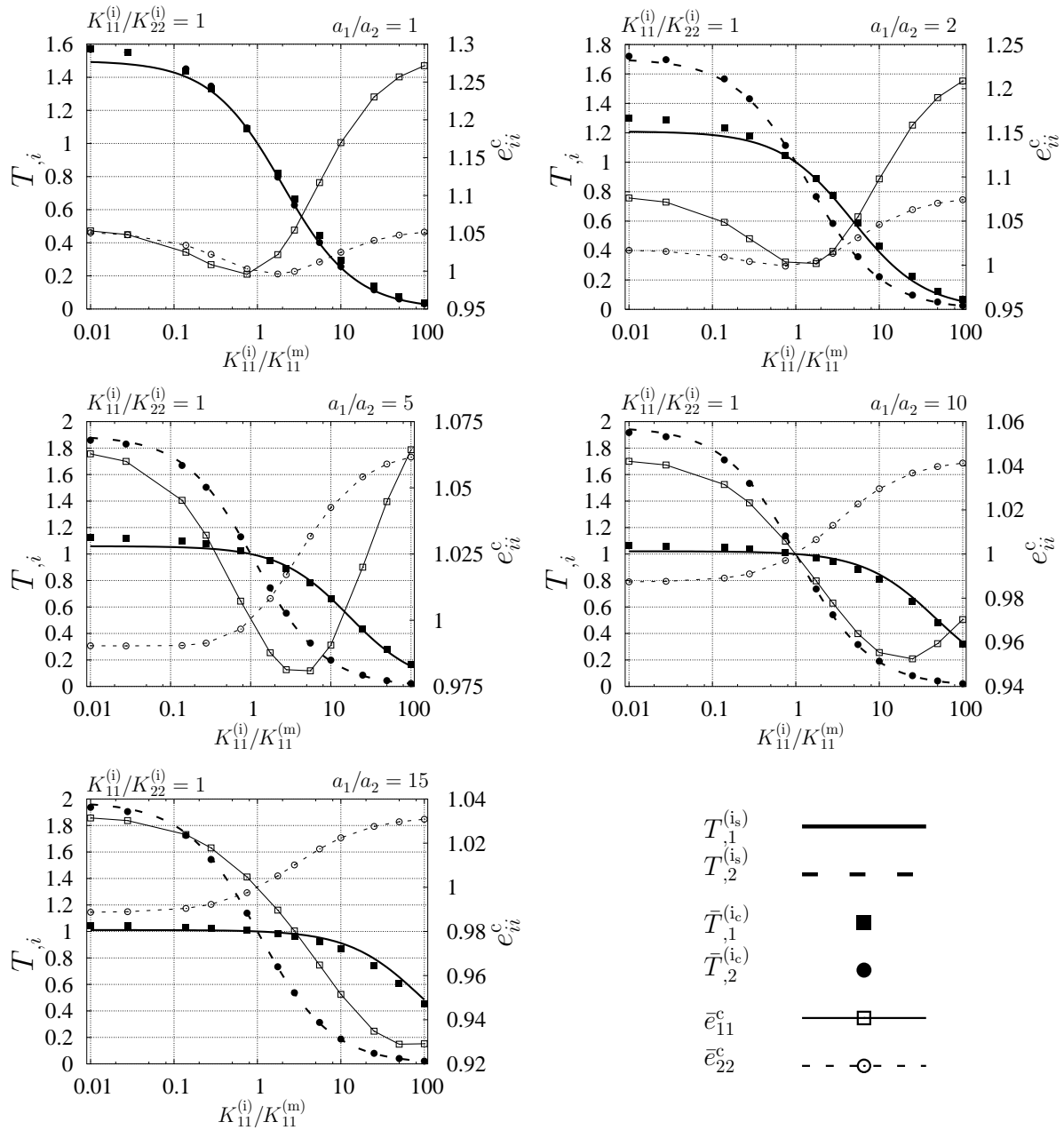


Figure 6.3: Collected results of averaged inclusion gradients of cylinders and corresponding spheroids due applied far field gradients of unit value along x_1 and x_2 (bold lines and filled symbols) and corresponding shape factors (thin lines and non-filled symbols) for $K_{11}^{(i)}/K_{22}^{(i)} = 1$.

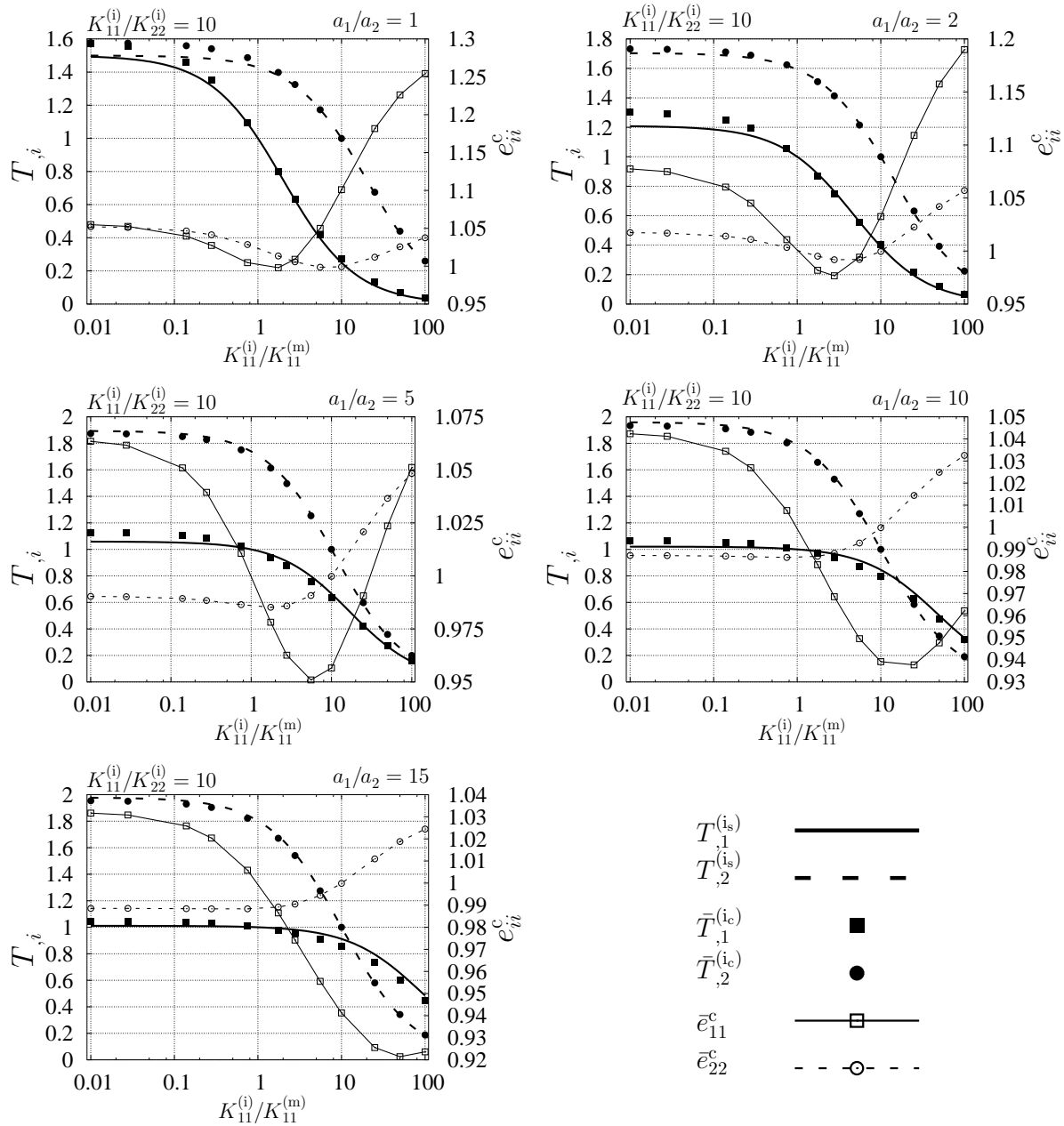


Figure 6.4: Collected results of averaged inclusion gradients of cylinders and corresponding spheroids due applied far field gradients of unit value along x_1 and x_2 (bold lines and filled symbols) and corresponding shape factors (thin lines and non-filled symbols) for $K_{11}^{(i)}/K_{22}^{(i)} = 10$.

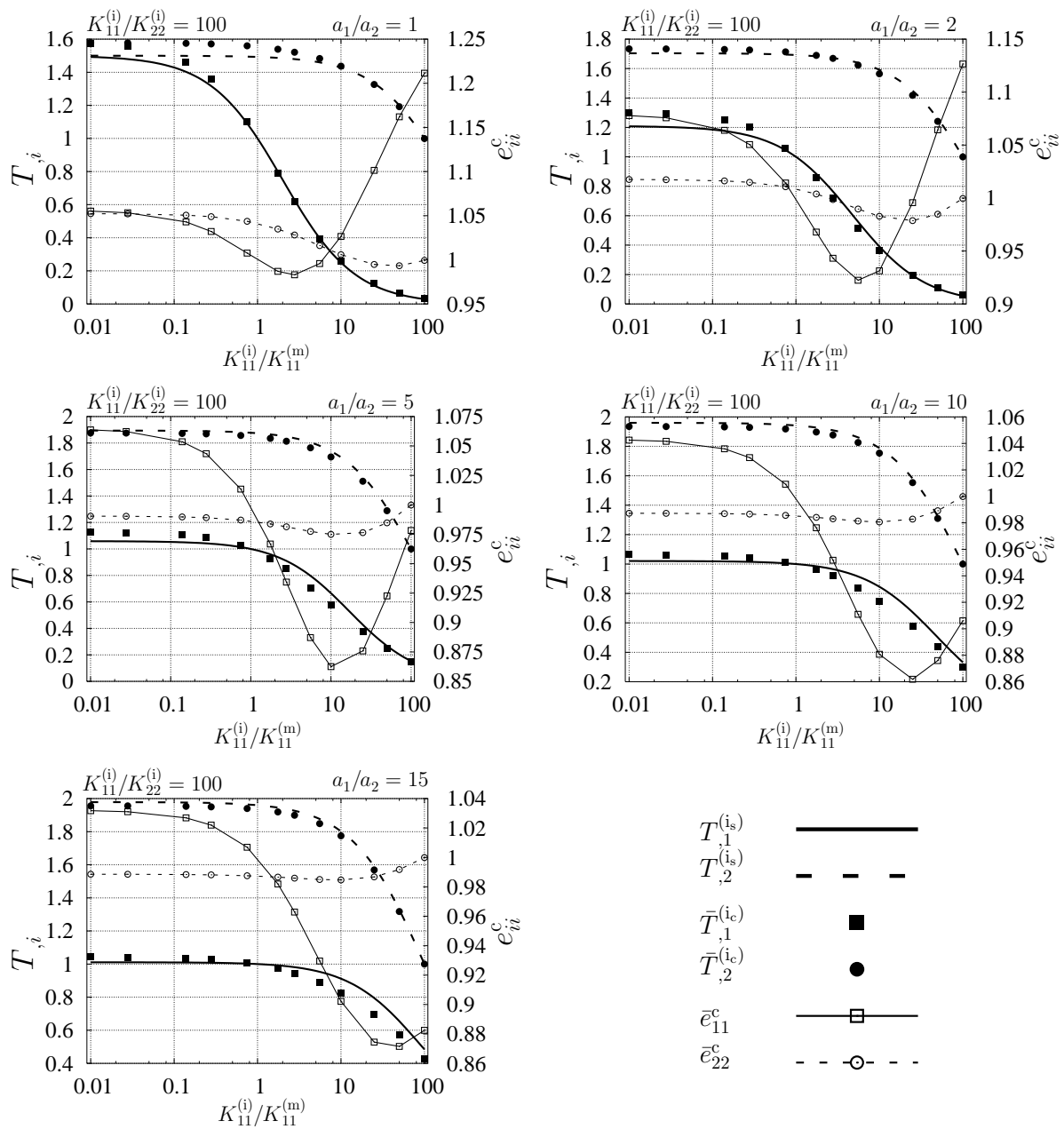


Figure 6.5: Collected results of averaged inclusion gradients of cylinders and corresponding spheroids due applied far field gradients of unit value along x_1 and x_2 (bold lines and filled symbols) and corresponding shape factors (thin lines and non-filled symbols) for $K_{11}^{(i)}/K_{22}^{(i)} = 100$.

6.2 Imperfectly Bonded Cylinders

In this section single, imperfectly bonded fibers of cylindrical shape embedded in an isotropic matrix of (practically) infinite extent are studied. Different cases of interfacial degradation are accounted for, see Table 3.4. Additionally, results pertaining to dilute spheroids as obtained with the analytical replacement operation (Section 5.1) are provided.

6.2.1 “Dilute” Unit Cell Model

As the principal axes of the fiber material and of the distributions of the interface parameter coincide with the rotational axis of the cylinders the modeling expense reduces significantly because symmetry planes with special properties can be identified, see Section 4.3. Only one eighth of the inclusion volume and associated matrix volume needs to be modeled. Due to the transversal isotropy of the modeled carbon fibers it is sufficient to investigate the resulting temperature distributions along the axial direction, x_1 , and one transverse direction, x_2 or x_3 . The size of the unit cell is chosen such that $L_i > 15 \times a_i$, the cylinder volume fraction being less than 0.2%. The inclusion material and the surrounding matrix material are meshed with ten node tetrahedral elements. In the interfacial area mesh refinement is carried out so the element edge length is approximately $1/12 \times a_2$, further mesh refinement is carried out where end face and side face meet, the element length there is approximately $1/20 \times a_2$. The mesh of the matrix block is coarsened towards the outer perimeter. Along the interface the mesh is non-conformal, appropriate contact/target elements are used to capture the effects of the imperfect thermal interface as described in Eq. (5.20).

The numerical evaluation of the interfacial surface temperatures for obtaining the phase averaged inclusion temperature gradient, $\bar{T}_{,i}^{(i)}$, and the apparent temperature gradient, $\bar{T}_{,i}^{(ir)}$, according to Eqs. (5.34) and (5.37), respectively, turns out to be fairly simple for the case of cylinders. For uniform far fields along the axial direction, x_1 , the problem is axisymmetric, (Fig. 6.6b, left row). The temperatures on the side faces (Fig. 6.6b, bottom left) do not contribute to $\bar{T}_{,1}^{(i)}$ and $\bar{T}_{,1}^{(ir)}$. Note that ΔT_2 approaches zero as $x_1 \rightarrow 0$, because there is no radial heat flux in the symmetry plane, i.e. no heat passes through the side faces. The temperatures at the top face can be integrated directly as the normal vector is aligned with the far field gradient. Note that ΔT_1 is greatest on the symmetry axis x_1 (Fig. 6.6b, top left). For a uniform far field along the transverse direction, x_2 , the temperatures at the end face and the midplane need not be considered as these faces are parallel to the

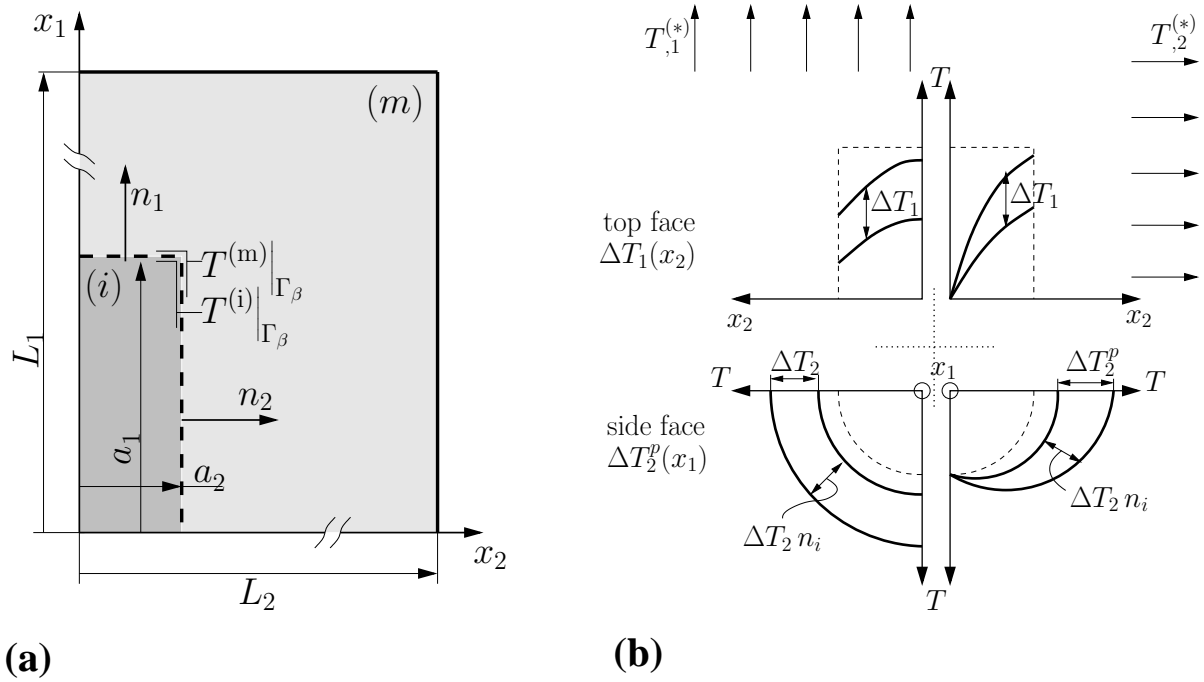


Figure 6.6: (a) Sketch of the employed symmetric unit cell with the interfacial temperatures $T^{(i)}|_{\Gamma_\beta}$ and $T^{(m)}|_{\Gamma_\beta}$ at the inclusion and matrix phase, respectively. (b) Sketch of the temperature gaps along the top face due to applied far field gradients along x_1 (top, left) and x_2 (top, right) and the side face due to applied far field gradients along x_1 (bottom, left) and x_2 (bottom, right).

far field gradient¹. Note that ΔT_1 approaches zero as $x_2 \rightarrow 0$ due to symmetry (Fig. 6.6b, top right). For the evaluation of $\bar{T}_{,2}^{(i)}$ and $\bar{T}_{,2}^{(ir)}$ a cosine variation of the temperatures is assumed, i.e.

$$T^{(r)}|_{\Gamma_\beta} = {}^p T^{(r)}|_{\Gamma_\beta} n_2 \quad , \quad (6.3)$$

with ${}^p T^{(r)}|_{\Gamma_\beta}$ being the temperatures at $(0 \leq x_1 \leq a_1, a_2, 0)$, see Fig. 6.6, bottom right. Direct evaluation of the averaged inclusion gradient field, $\bar{T}_{,2}^{(i)}$, by means of volume averaging showed no significant discrepancies from the above surface based evaluation procedure.

The temperature profile is approximated to be constant between two nodes, the constant temperature in between equalling the average of the two nodal temperatures. Due

¹Employing the divergence theorem for the top and bottom face yields $\bar{T}_{,1}^{(ir)} \neq 0$ and $\bar{T}_{,1}^{(i)} \neq 0$. This is due to the employed model geometry which misses the “second” half of the fiber with mirror-symmetrical gradient fields, that cancel the overall averages $\bar{T}_{,1}^{(i)}$ and $\bar{T}_{,1}^{(ir)}$.

to the relatively fine mesh in the end face–side face region this piecewise constant approximation of the temperature field gives sufficient accuracy, as was shown by a comparison of $\bar{T}_{,1}^{(i)}$ evaluated by means of volume averaging and the divergence theorem.

6.2.2 Results

Results are provided for carbon fibers embedded in copper. The corresponding material properties for carbon and copper are given in Chapter 3, Table 3.1 and Table 3.2, respectively. Six cases of different interfacial scenarios, *C1* to *C6*, are accounted for; these are defined in Table 3.4, Chapter 3. Cylinders with discrete aspect ratios of $a_1/a_2 = 2, 5, 10$, and 15 are investigated. Corresponding results for spheroidal inclusions are provided for $a_1/a_2 = 5$ and 10, as these aspect ratios are employed in unit cell investigations pertaining to non-dilute volume fractions (Chapter 8). Note that “pseudo” end faces have been allocated to the spheroids in order to model selective failure of the “end face” interface. They are chosen such that the ratio of end face area over side face area of both cylinders and spheroids are the same.

Table 6.1: Reduced conductivities, $\bar{K}_{ii}^{(i_r)}$, and corresponding dilute concentration tensors, ${}^0\bar{D}_{ii}^{(m,i_r)}$, of a carbon fiber ($a_1/a_2 = 2$) embedded in a copper matrix (see Tables 3.1 and 3.2 for material data) for different interfacial scenarios (Table 3.4).

	case	$K_{22}^{(i)} = 10$				$K_{22}^{(i)} = 100$			
		${}^0\bar{D}_{11}^{(m,i_r)}$	${}^0\bar{D}_{22}^{(m,i_r)}$	$\bar{K}_{11}^{(i_r)}$	$\bar{K}_{22}^{(i_r)}$	${}^0\bar{D}_{11}^{(m,i_r)}$	${}^0\bar{D}_{22}^{(m,i_r)}$	$\bar{K}_{11}^{(i_r)}$	$\bar{K}_{22}^{(i_r)}$
cylinders	$C1$	0.7219	1.6693	1000	10	0.7473	1.4142	1000	100
	$C2$	1.2483	1.6920	161.7	10	1.1735	1.4310	385.9	100
	$C3$	1.3035	1.7320	2.7	0.7	1.3035	1.7319	2.7	0.7
	$C4$	1.3050	1.7320	1.4	0.6	1.3035	1.7319	1.4	0.6
	$C5$	1.2873	1.7202	25.8	4.1	1.2872	1.7122	26.4	6.6
	$C6$	1.3013	1.7202	13.2	3.9	1.3010	1.7127	13.9	6.1

Table 6.2: Reduced conductivities, $\bar{K}_{ii}^{(i_r)}$, and corresponding dilute concentration tensors, ${}^0\bar{D}_{ii}^{(m,i_r)}$, of a carbon fiber ($a_1/a_2 = 5$) embedded in a copper matrix (see Tables 3.1 and 3.2 for material data) for different interfacial scenarios (Table 3.4).

	case	$K_{22}^{(i)} = 10$				$K_{22}^{(i)} = 100$			
		${}^0\bar{D}_{11}^{(m,i_r)}$	${}^0\bar{D}_{22}^{(m,i_r)}$	$\bar{K}_{11}^{(i_r)}$	$\bar{K}_{22}^{(i_r)}$	${}^0\bar{D}_{11}^{(m,i_r)}$	${}^0\bar{D}_{22}^{(m,i_r)}$	$\bar{K}_{11}^{(i_r)}$	$\bar{K}_{22}^{(i_r)}$
cylinders	$C1$	0.8502	1.8139	1000	10	0.8757	1.4959	1000	100
	$C2$	1.0855	1.8274	397.8	10	1.0494	1.5034	693.9	100
	$C3$	1.1253	1.8733	12.8	0.6	1.1253	1.8731	12.9	0.7
	$C4$	1.1265	1.8733	9.6	0.6	1.1266	1.8732	9.7	0.6
	$C5$	1.1092	1.8582	105.6	4.0	1.1088	1.8483	112.2	6.3
	$C6$	1.1205	1.8581	78.4	3.9	1.1199	1.8484	85.3	6.1
spheroids	$C1$	0.9097	1.8484	1000	10	0.9097	1.5173	1000	100
	$C2$	0.9131	1.8484	973.4	10	0.9131	1.5174	973.4	99.9
	$C3$	1.0572	1.8914	11.4	0.6	1.0572	1.8912	11.4	0.7
	$C4$	1.0572	1.8914	11.2	0.6	1.0572	1.8912	11.2	0.7
	$C5$	1.0413	1.8756	104.1	4.0	1.0413	1.8650	104.1	6.3
	$C6$	1.0415	1.8756	103	4.0	1.0415	1.8650	103	6.3

Table 6.3: Reduced conductivities, $\bar{K}_{ii}^{(i_r)}$, and corresponding dilute concentration tensors, ${}^0\bar{D}_{ii}^{(m,i_r)}$, of a carbon fiber ($a_1/a_2 = 10$) embedded in a copper matrix (see Tables 3.1 and 3.2 for material data) for different interfacial scenarios (Table 3.4).

	case	$K_{22}^{(i)} = 10$				$K_{22}^{(i)} = 100$			
		${}^0\bar{D}_{11}^{(m,i_r)}$	${}^0\bar{D}_{22}^{(m,i_r)}$	$\bar{K}_{11}^{(i_r)}$	$\bar{K}_{22}^{(i_r)}$	${}^0\bar{D}_{11}^{(m,i_r)}$	${}^0\bar{D}_{22}^{(m,i_r)}$	$\bar{K}_{11}^{(i_r)}$	$\bar{K}_{22}^{(i_r)}$
cylinders	$C1$	0.9189	1.8770	1000	10	0.9350	1.5295	1000	100
	$C2$	1.0376	1.8842	639.0	10	1.0214	1.5333	841.3	100
	$C3$	1.0622	1.9324	44.5	0.6	1.0622	1.9322	45.0	0.7
	$C4$	1.0634	1.9324	38.5	0.6	1.0633	1.9322	39.0	0.7
	$C5$	1.0482	1.9157	281.5	4.0	1.0479	1.9050	300.2	6.2
	$C6$	1.0567	1.9157	245.0	4.0	1.0561	1.9051	265.6	6.2
spheroids	$C1$	0.9652	1.9093	1000	10	0.9652	1.5475	1000	100
	$C2$	0.9654	1.9093	995.7	10	0.9654	1.5475	995.7	100
	$C3$	1.0182	1.9570	42.3	0.6	1.0182	1.9568	42.3	0.7
	$C4$	1.0182	1.9570	42.3	0.6	1.0182	1.9568	42.3	0.7
	$C5$	1.0033	1.9356	302.6	4.0	1.0033	1.9278	302.6	6.3
	$C6$	1.0033	1.9356	302.6	4.0	1.0033	1.9278	302.2	6.3

Table 6.4: Reduced conductivities, $\bar{K}_{ii}^{(i_r)}$, and corresponding dilute concentration tensors, ${}^0\bar{D}_{ii}^{(m,i_r)}$, of a carbon fiber ($a_1/a_2 = 15$) embedded in a copper matrix (see Tables 3.1 and 3.2 for material data) for different interfacial scenarios (Table 3.4).

	case	$K_{22}^{(i)} = 10$				$K_{22}^{(i)} = 100$			
		${}^0\bar{D}_{11}^{(m,i_r)}$	${}^0\bar{D}_{22}^{(m,i_r)}$	$\bar{K}_{11}^{(i_r)}$	$\bar{K}_{22}^{(i_r)}$	${}^0\bar{D}_{11}^{(m,i_r)}$	${}^0\bar{D}_{22}^{(m,i_r)}$	$\bar{K}_{11}^{(i_r)}$	$\bar{K}_{22}^{(i_r)}$
cylinders	$C1$	0.9450	1.8994	1000	10	0.956	1.5411	1000	100
	$C2$	1.0240	1.9041	752.3	10	1.0136	1.5437	893.2	100
	$C3$	1.0408	1.9531	91.0	0.6	1.0408	1.9529	92.1	0.7
	$C4$	1.0419	1.9531	82.9	0.6	1.0419	1.9529	83.9	0.7
	$C5$	1.0297	1.9359	438.0	4.0	1.0296	1.9249	460.0	6.2
	$C6$	1.0361	1.9359	403.7	4.0	1.0357	1.9249	429.4	6.2

In Fig. 6.7 temperature profiles due to applied far field gradients along x_1 (left) and x_2 (right) for a cylindrical carbon fiber ($a_1/a_2 = 5$, $K_{11}^{(i)} = 1000$ W/mK, $K_{22}^{(i)} = 100$ W/mK) embedded in a copper matrix ($K^{(m)} = 360$ W/mK) for scenarios $C1$, $C2$, $C5$ and $C6$ are plotted. Based on these curves the corresponding inclusion gradients $\bar{T}_{,i}^{(i)}$ and $\bar{T}_{,i}^{(r)}$ as well as the reduced conductivities are obtained (compare, Table 6.2). Note that for scenario $C1$ the interfacial matrix and inclusion temperatures coincide. For scenario $C2$ the side face temperatures coincide, while the end face temperatures gap apart, see Fig. 6.7 left and right, respectively.

In Fig. 6.8 contour plots of the inclusion gradients, $T_{,1}^{(i)}$, due to an applied far field gradient of unit value along x_1 are collected for a carbon fibers ($a_1/a_2 = 5$, $K_{11}^{(i)} = 1000$ W/mK, $K_{22}^{(i)} = 100$ W/mK) embedded in a copper matrix ($K^{(m)} = 360$ W/mK), that pertain to all six investigated scenarios of interfacial degradation. With increasing interface resistance (decreasing interface parameter β) the inclusion gradients, $T_{,1}^{(i)}$, decrease, as the

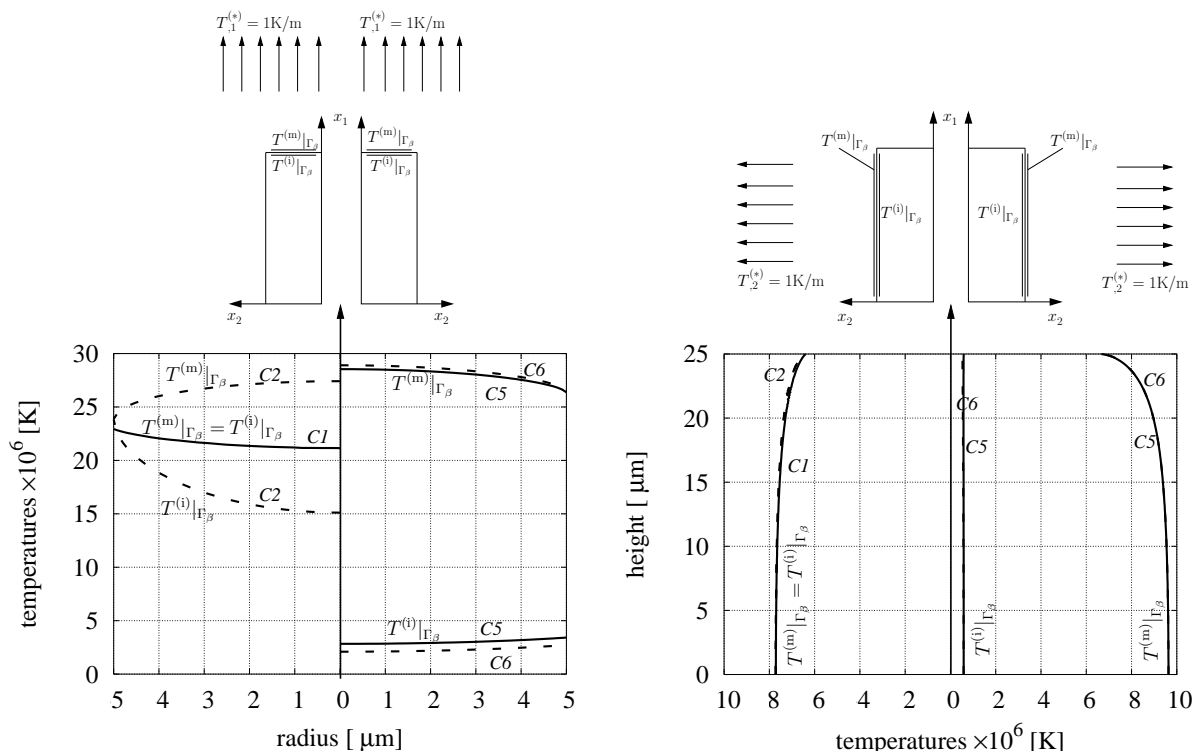


Figure 6.7: Temperature profiles on the end face (left) and side face (right) due to applied far field gradients of unit value along x_1 and x_2 , respectively, for a carbon fiber ($a_1/a_2 = 5$, $K_{11}^{(i)} = 1000$ W/mK, $K_{22}^{(i)} = 100$ W/mK) embedded in a copper matrix ($K^{(m)} = 360$ W/mK) for scenarios $C1$, $C2$, $C5$, and $C6$.

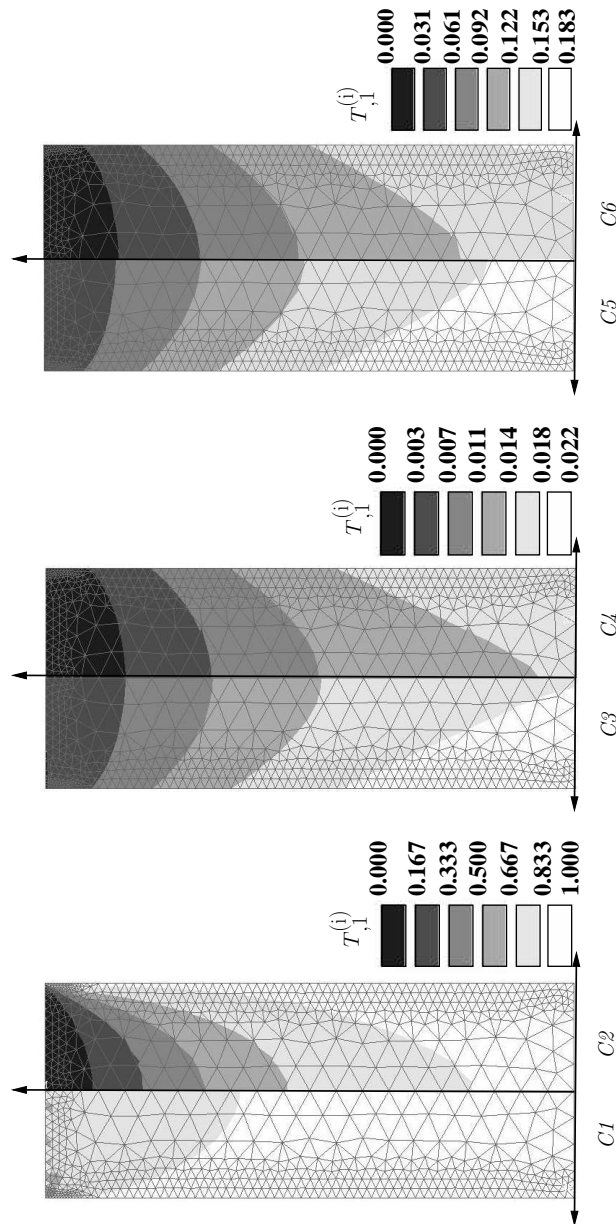


Figure 6.8: Inclusion temperature gradients, $T_{,1}^{(i)}$, due to an applied unit far field gradient $T_{,1}^{(*)}$ predicted for a carbon fiber ($a_1/a_2 = 5$, $K_{11}^{(i)} = 1000$ W/mK, $K_{22}^{(i)} = 100$ W/mK) embedded in a copper matrix ($K^{(m)} = 360$ W/mK) for the six investigated scenarios of interfacial degradation (Table 3.4).

flux passing through the interface is reduced. The corresponding gradients of the perfectly bonded replacement inclusion, $T_{,1}^{(ir)}$, increase (compare Table 6.2) at the same time.

Chapter 7

Results for Aligned Carbon Fibers

In this chapter numerical unit cell studies are presented which focus on aligned continuously reinforced carbon–copper composites and aligned short fiber reinforced carbon–copper composites.

In the case of aligned continuous fibers regular fiber arrangements as well as random fiber arrangements are investigated. Arrangements of aligned short fibers are studied with respect to the influence of the axial fiber offset and the degree of axial staggering on the effective conductivity. For both, continuous fibers and staggered short fibers, the influence of thermal barriers at the fiber–matrix interfaces on the effective conductivity is investigated by means of appropriate thermal interface elements.

For the special case of perfect thermal interfaces, variational techniques are available for predicting the effective transverse conductivity of continuously reinforced composites. HS bounds ? are classical variational bounds which can be linked to microgeometries that can be thought of as tightly packed, randomly placed composite cylinders of varying diameters (the cores of the composite cylinders consist of the reinforcement, and the matrix is placed in a concentric shell of the appropriate thickness to give the desired volume fraction). When the matrix conductivity is larger than the transverse fiber conductivity for two–phase materials the Mori–Tanaka predictions coincide with the upper HS bounds.

Tighter bounds on the effective conductivity of composites reinforced with continuous aligned fibers can be given in terms of three point (3P) bounds ???. Those used in the present study apply to materials in which the reinforcements take the form of randomly positioned aligned non–overlapping circular cylinders of equal radius.

All calculations are carried out for carbon–copper composites (see Chapter 3 for ma-

terial properties) with a fiber volume fraction $\xi^{(i)} = 0.4$. The short fibers are modelled as cylinders with an aspect ratio of 10. The unit cell calculations were carried out with the finite element program ANSYS 5.7 (ANSYS, Inc., Canonsburg, PA). The matrix mesh is chosen to be finer than the fiber mesh taking into account the fact that the temperature gradients in the matrix are higher than those in the fibers. The global element length of the matrix mesh is one sixth of the fiber radius, while the fiber mesh size is one fifth of the fiber radius.

The fibers are assumed to be aligned with x_1 .

7.1 Aligned Continuous Fibers

The investigated microgeometries of unidirectional, continuous fibers embedded in a matrix comprise square, hexagonal and rectangular arrangements and are referred to as regular arrangements, see Fig. 7.1. Clearly these regular arrangements do not fully represent "real" composites. Improved models can be obtained with multi-fiber unit cells in which fiber positions are selected randomly or taken from micrographs. In the present study a unit cell with pseudo-random fiber positions is used (Fig. 7.2) which is based on the arrangement used in ? but with a slightly reduced fiber radius to meet the volume fraction requirement. The unit cell models for continuously fiber reinforced carbon-copper composites focus on the transverse behavior as the axial conductivity coincides with the upper Wiener bound, Eq. (2.9). Accordingly, for a two phase composite with continuous, aligned orthotropic fibers in an isotropic matrix material the effective axial thermal conductivity takes the form

$$K_{11}^{(*)} = (1 - \xi^{(i)})K^{(m)} + \xi^{(i)}K_{11}^{(i)} \quad . \quad (7.1)$$

In order to determine the effective transverse conductivity of composites reinforced with aligned continuous fibers it is sufficient to model a representative cross-section with two dimensional unit cells.

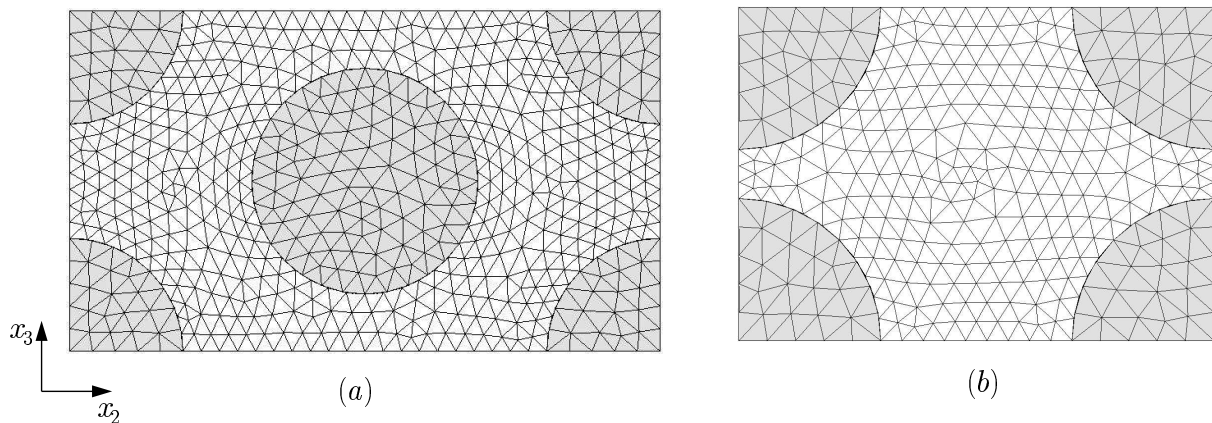


Figure 7.1: Two dimensional unit cell geometries of aligned continuously reinforced composites for hexagonal (a) and rectangular (b) arrangements.

Effective axial conductivity ($K_{11}^{(i)} > K^{(m)}$)

The effective axial conductivity is neither influenced by the interface parameter β nor by the fiber arrangement and can be calculated analytically with Eq. (7.1), yielding a conductivity of $K_{11}^{(*)} = 616$ W/mK in axial direction.

The resulting temperature gradients in the constituents are uniform (coupling of temperature gradients) and only the x_1 -component is nonzero, equaling the far field temperature gradient applied along the x_1 -axis, $T_{,1}^{(*)} = \Delta T_1/L_1$. The heat flux is different in matrix and fibers, but uniform within each constituent phase and linearly coupled to the temperature gradient by the respective phase conductivity.

Effective transverse conductivity ($K_{22}^{(i)}, K_{33}^{(i)} < K^{(m)}$)

Perfect Interface In a first step the effective transverse conductivity is studied for perfect thermal contact (Table 7.1). The random arrangement of 60 fibers obeys the 3P-bounds, which are violated by the square and hexagonal arrangements, which lack "randomness". However, the hexagonal and square arrangements obey the HS bounds and as the mesh is refined they approach the upper HS bound. The Wiener bounds are provided as well, with the upper and lower bound differing by more than 400 W/mK.

The hexagonal and the square arrangements show transversely isotropic effective conductivities¹ while the random arrangement shows an orthotropic behavior that differs minimally from transverse isotropy.

The hexagonal arrangement has a more balanced temperature gradient distribution than the square arrangement. The ratio of maximum local temperature gradient over the applied far field gradient of the square arrangement is approximately 5% higher than the corresponding ratio of the hexagonal arrangement.

The rectangular arrangements show orthotropic effective conductivities, the deviation from transverse isotropy increases as the in-plane aspect ratio of the unit cell model increases. As fibers move closer to each other with respect to the x_3 -direction, the effective conductivity in x_2 -direction $K_{22}^{(*)}$ is severely reduced because of the ever decreasing width of the "bridges" of highly conducting matrix material, which forces increasing parts of the overall heat flow to flow through poorly conducting fiber material. "Bridges" of matrix material which are aligned to the far field gradient are spots of local gradient (and flux) concentration (Fig. 7.2).

¹Note that the square arrangement exhibits orthotropic elastic behavior.

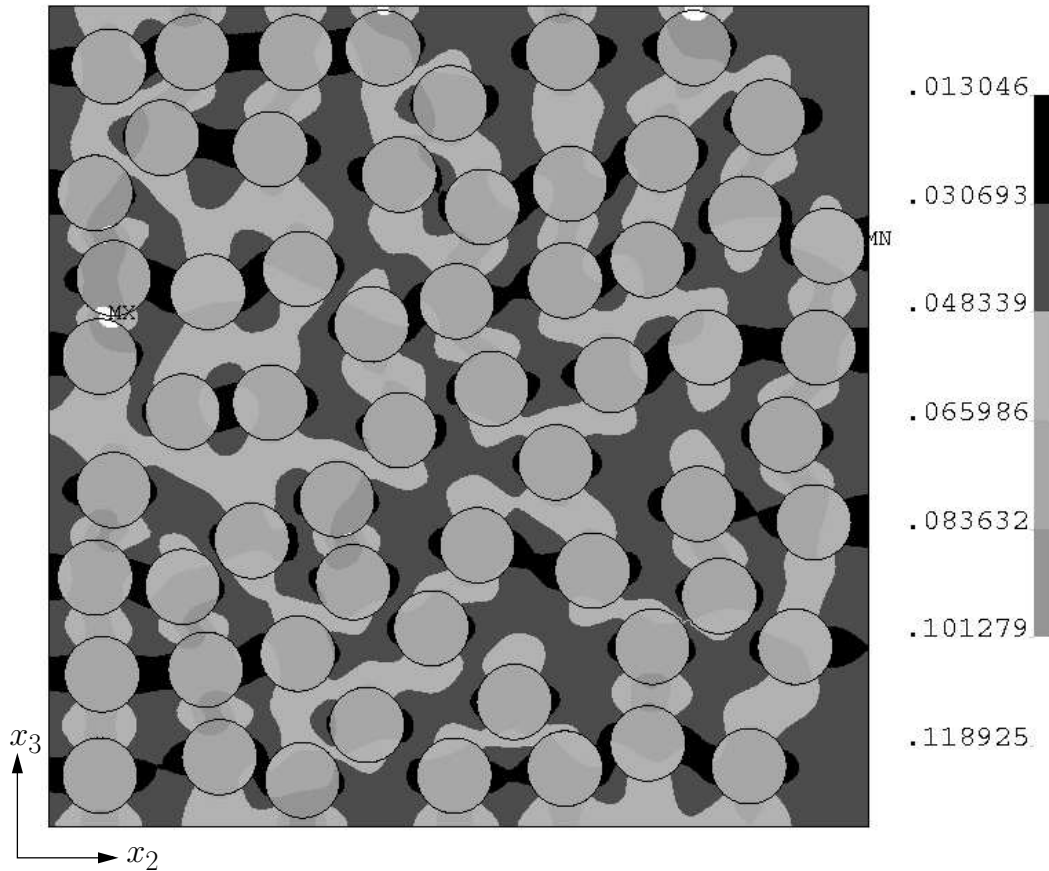


Figure 7.2: Predicted distribution of temperature gradients $T_{,2}$ for random arrangement of aligned continuous carbon fibers embedded in copper matrix under an applied far field gradient of $T_{,2}^{(*)} = 0.0562$ K/m and symmetry BCs.

Thermal Barrier Interface The influence of the thermal interface is studied for the square and a rectangular ($L_3/L_2 = 0.6$) arrangement. The interface conductance (βr_{fiber} , r_{fiber} being the fiber radius) is varied from 10^{-3} W/mK to 10^7 W/mK, covering the range of thermal interfaces from perfectly insulating interfaces to perfectly conducting interfaces. Figure 7.3 shows the effective transverse conductivities predicted by the unit cell approach as well as by a Mori–Tanaka theory for coated inclusions ?.

For small interface conductances the fibers are excluded from conducting heat. An increase of the thermal interface conductance increases the effective transverse conductivity of the composite because the fibers get more involved in the heat transfer. Only in the intermediate range of interface conductance from 10^1 W/mK to 10^4 W/mK can significant improvements in the effective conductivity be gained by improving the thermal interface.

Table 7.1: Analytical and numerical predictions for the effective transverse conductivities of aligned, continuously reinforced carbon–copper composites with perfect thermal contact

method	arrangement	$K_{22}^{(*)}$ [W/mK]	$K_{33}^{(*)}$ [W/mK]
Wiener upper bound		616	616
Wiener lower bound		176.47	176.47
HS upper bound		227.23	227.23
HS lower bound		202.63	202.63
3P upper bound		225.49	225.49
3P lower bound		221.93	221.93
Unit cell	hexagonal	227.22	227.22
	square $L_3/L_2=1$	226.96	226.96
	random (60 fibers)	225.46	225.44
	rectangular $L_3/L_2=0.9$	223.47	230.25
	rectangular $L_3/L_2=0.8$	219.1	233.79
	rectangular $L_3/L_2=0.7$	213.22	237.8
	rectangular $L_3/L_2=0.6$	204.43	242.52

For all interface conductances the unit cell predictions for the effective transverse conductivity of the square arrangement are slightly below the analytical Mori–Tanaka predictions, which keep the character of an upper bound independently of the interface conductance. The existence of a thermal interface has different impacts on the effective principal conductivities of the investigated rectangular arrangement. For rectangles that are narrower in x_3 –direction than in the x_2 –direction, the effective conductivity in x_3 –direction, $K_{33}^{(*)}$, is less sensitive to the interface conductance than the effective conductivity in x_2 –direction, $K_{22}^{(*)}$. A further reduction of the aspect ratio of the rectangle would further reduce the width of the bridges of matrix material in between the cylinders. In combination with an ideally insulating interface the effective conductivity in x_2 –direction would tend to zero as the bridges of matrix material disappear.

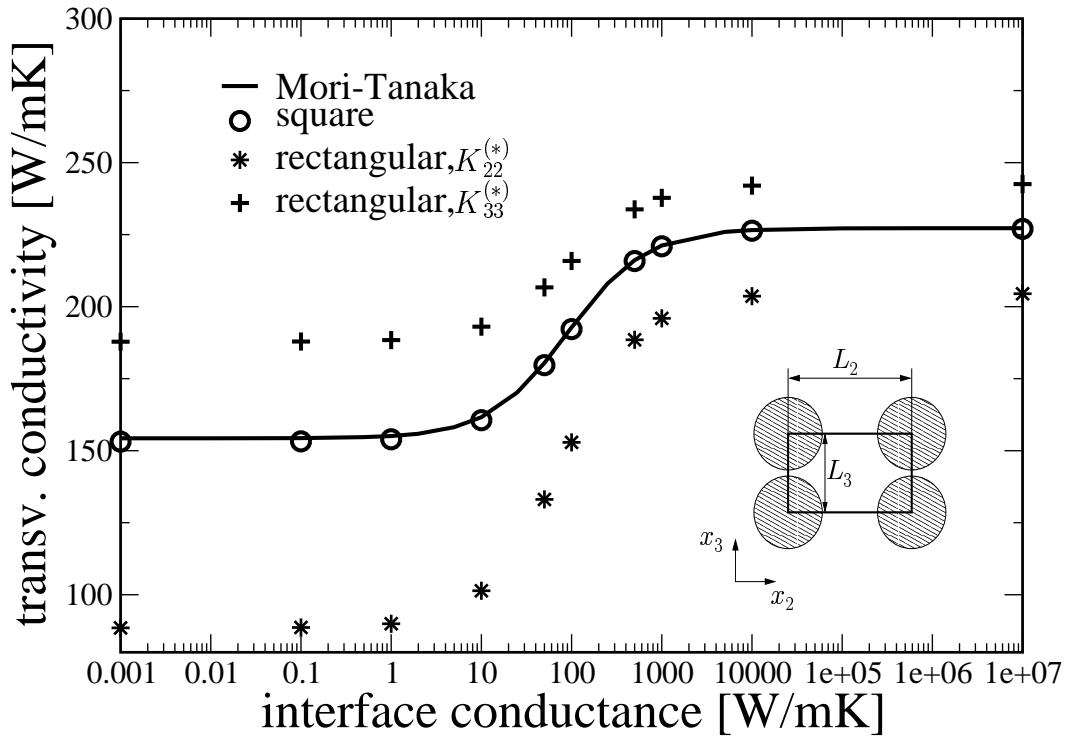


Figure 7.3: Predictions for the effective transverse conductivities of aligned continuously reinforced carbon–copper composites versus the effective interface conductance based on analytical and various unit cell approaches.

7.1.1 Summary – Aligned Continuous Fibers

For carbon–copper composites reinforced with aligned continuous fibers and ideal interfaces it was shown for the transverse effective conductivities, that the unit cell results for regular arrangements obey the HS bounds. A random unit cell consisting of 60 fibers was employed additionally and was shown to obey the tighter 3P–bounds. The Wiener bounds were provided as well, showing that they are too slack for practical use. A thermal interface barrier has a severe impact on the effective transverse conductivity while the effective axial conductivity is not affected. The investigation covered the range from perfectly insulating interfaces to perfectly conducting interfaces.

7.2 Aligned Staggered Short Fibers

7.2.1 Micro Arrangements

In addition to continuous fiber reinforced composites, periodic arrays of aligned short fibers in a matrix are investigated.

Fiber aspect ratio, fiber volume fraction and two geometry parameters are sufficient to set up the periodic micro topologies of staggered aligned short fibers ? which are investigated (Fig. 7.4). The fiber aspect ratio ($a_1/a_2 = 10$) and the fiber volume fraction ($\xi^{(i)} = 0.4$) are kept constant, leaving two dimensionless parameters, α and δ , to describe the considered periodic arrangements. The ratio of fiber-to-fiber offset in axial direction over fiber length, a_1 is denoted by α ,

$$\alpha = \frac{L_1 - a_1}{a_1} \quad , \quad (7.2)$$

where L_1 is the unit cell length in axial direction. As α decreases the fibers move axially closer together. The limiting case of $\alpha = 0$ represents continuous fibers.

The second geometry parameter δ defines the degree of stagger, which gives the axial offset of one fiber compared to its four closest neighbors in radial direction (s_{shift}).

$$\delta = \frac{2 s_{\text{shift}}}{L_1} \quad (7.3)$$

A nonstaggered arrangement is referred to as $\delta = 0$.

All unit cells show mirror-symmetries with regard to reflections along the x_2 - and x_3 -axis (transverse direction), while they tile the space by translation along the x_1 -axis (the axial direction), see Fig. 7.4. Accordingly mixed BCs are used, i.e. periodic BCs for the faces at $x_1 = 0$ and $x_1 = L_1$ (periodic faces) and symmetry BCs for the remaining four faces (symmetric faces).

Microtopologies using $\delta = 0$ and $\delta = 1$, exhibit mirror symmetry with regards to reflection along the x_3 axis as well.

The investigated microgeometries (excluding the special arrangements of δ equaling either zero or one and thus introducing a third set of symmetry-planes at $z = 0$, $z = \frac{1}{2}L_1$, and $z = L_1$) behave in such a way that under applied far field gradients along transverse directions a heat flux in axial direction is induced in the unit cell due to constraining the temperatures on the periodic faces. However, globally this heat flux is cancelled as a mirror-symmetric unit cell (obviously containing the same information on the microgeometry) under the same loading conditions would trigger off the same axial heat flux but

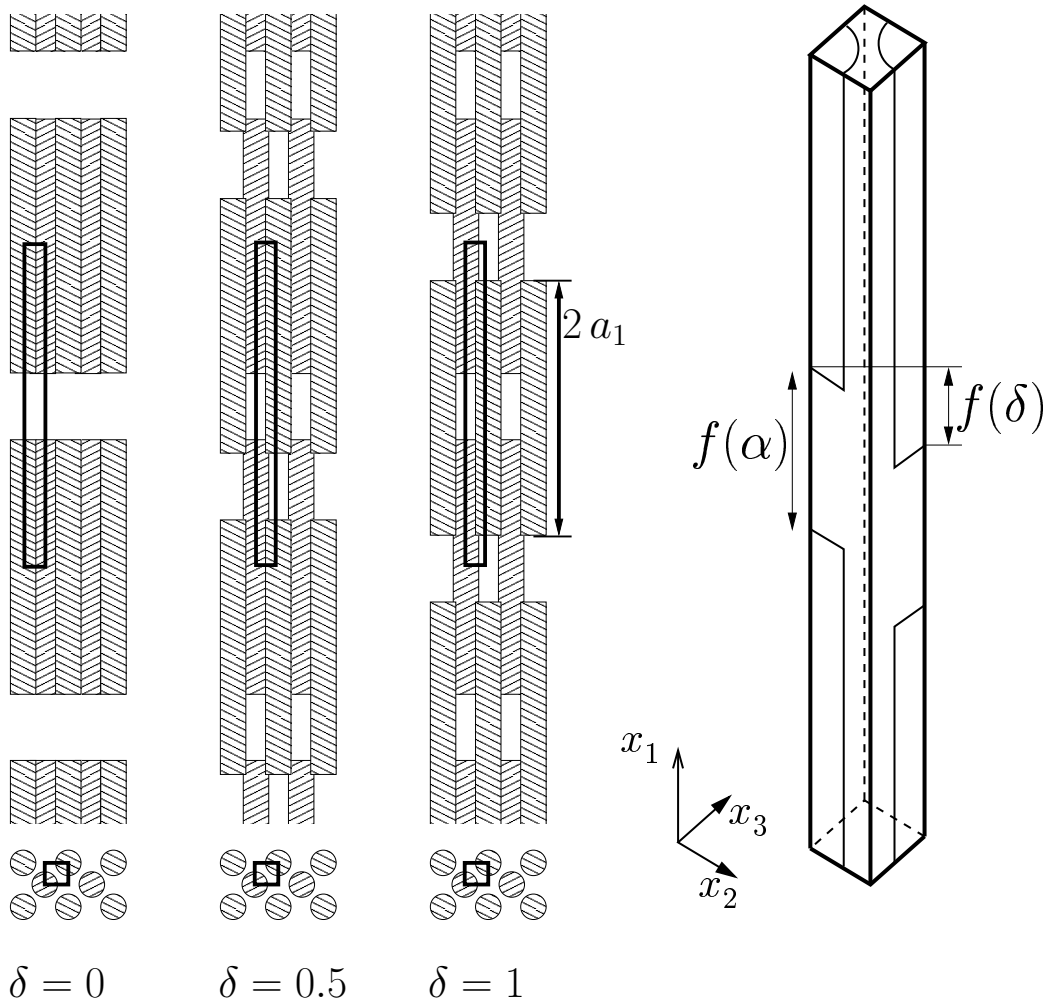


Figure 7.4: Different staggered and nonstaggered arrangements of aligned short fibers ($a_1/a_2=10$) for an axial fiber offset of $\alpha = 0.25$ (left). The geometry parameters δ and α , which can be chosen to meet a prescribed degree of staggering and axial fiber offset (right).

in opposite direction.

7.2.2 Results for Aligned Short Fiber Reinforced Carbon Copper Composites

Perfect interfaces The case of perfect thermal contact is investigated first. As an estimate a standard and a hybrid standard Mori–Tanaka model for aligned spheroidal (E–

Table 7.2: Analytical and numerical predictions for the effective conductivities of aligned, short fiber reinforced carbon–copper composites

geometry– parameters	perfect thermal interface, $C1$		failure of end face interface, $C2$	
	axial [W/mK]	transv. [W/mK]	axial [W/mK]	transv. [W/mK]
E–MT/a	610.58	227.97	608.93	227.97
H–MT/a	605.75	228.73	554.97	228.57
$\alpha = 0.01; \delta = 1$	612.21	226.98	562.74	226.96
$\alpha = 0.8; \delta = 1$	603.24	228.62	563.95	228.37
$\alpha = 0.01; \delta = 0$	612.08	227.02	549.80	227.00
$\alpha = 0.8; \delta = 0$	522.44	242.09	474.46	241.98

MT/a) and aligned cylindrical fibers (H–MT/a), respectively, are used. The aspect ratio of the fibers is 10. Corresponding dilute concentration tensors are listed in Section 6.2, Table 6.3. The resulting overall conductivity tensors are transversally isotropic, with an effective axial conductivity of 610.58 W/mK and 605.75 W/mK and an effective transverse conductivity of 227.97 W/mK and 228.57 W/mK for spheroidal and cylindrical inclusions, respectively (Table 7.2). Note that contrary to the unit cell method the Mori–Tanaka predictions can only account for inclusion orientations but not for specific positions of inclusions to each other. The predictions for spheroidal fibers are very close to those of aligned continuous carbon fibers ($\alpha = 0$), and the predictions for cylindrical fibers are only slightly below those of spheroidal inclusions of the same aspect ratio.

A non–staggered arrangement ($\delta = 0$) and a staggered arrangement ($\delta = 1$) are investigated as the fiber offset in axial direction is varied from $\alpha = 0.01$ to $\alpha = 0.8$. For very small fiber offsets the effective axial conductivity for both investigated arrangements is highest and approaches to the upper Wiener bound that pertains to continuously reinforced fibers, while the effective transverse conductivity is the lowest. As the fiber offset is increased the two sets of arrangements exhibit different behavior (Table 7.2, Fig. 7.5 and Fig. 7.6).

The effective axial conductivities of micro arrangements described by $\delta = 0$ decrease steadily as the fiber offset is increased due to the increasing regions of relatively poorly

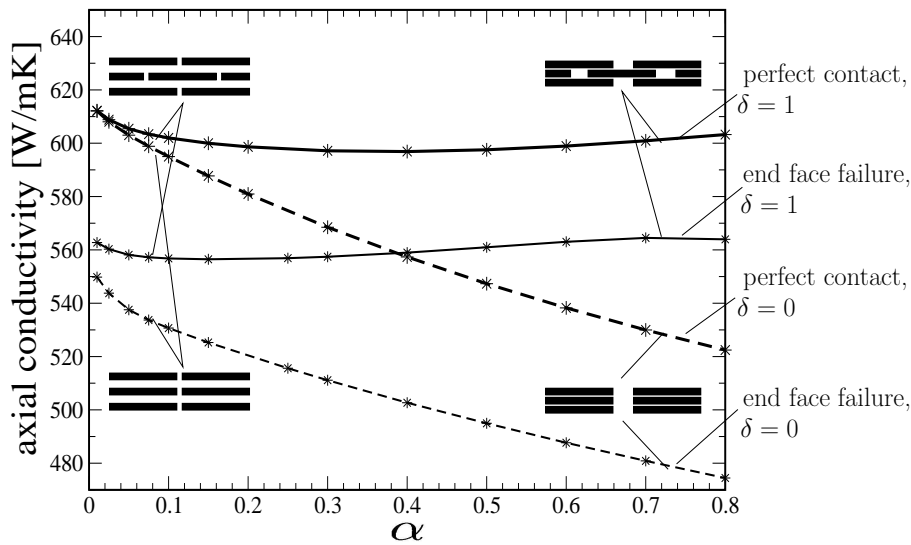


Figure 7.5: Predicted effective axial conductivities for non staggered ($\delta = 0$) and maximum staggered ($\delta = 1$) arrangements of aligned short fibers ($\xi^{(i)} = 0.4, a_1/a_2 = 10$) for different axial fiber offsets α ; perfect thermal contact and failure of the end face interface (perfectly insulating).

conductive matrix material (compared to the axial conductivity of the fibers) in between the blocks of fibers. The staggered microgeometries ($\delta = 1$) are much less affected by the axial fiber offset α and maintain a higher effective axial conductivity than microgeometries with $\delta = 0$. This better axial "performance" of staggered arrangements is due to the fact that relatively poorly conducting matrix regions are bridged by highly conducting fibers. A minimum of the effective axial conductivity is reached at $\alpha = 0.4$. For larger axial fiber offsets the effective axial conductivity increases again as the fibers move closer to each other in radial direction to meet the volume fraction requirement, simultaneously reducing the resistance for heat flowing through the fiber side faces into the next fiber.

Similar mechanisms govern the transverse effective behavior (note again that in the transverse direction the matrix is the highly conductivity material), but the differences between the effective conductivities of the two investigated microgeometries pertaining to $\delta = 0$ and $\delta = 1$ is less pronounced (Fig. 7.6).

Failed End Face Interfaces The influence of decohesion or lack of contact of the interfaces at the fibers' end faces, i.e. perfectly insulating interfaces, is also investigated. The effective axial conductivity is reduced severely while the effective transverse conduct-

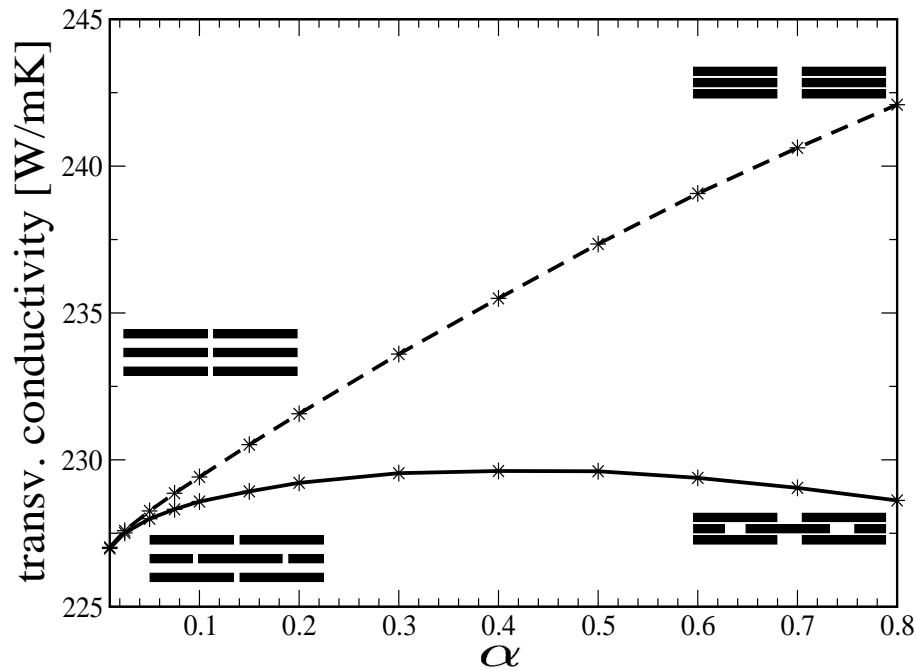


Figure 7.6: Predicted effective transverse conductivities for non-staggered ($\delta = 0$, dashed line) and maximum staggered ($\delta = 1$, solid line) arrangements of aligned short fibers ($\xi^{(i)} = 0.4$, $a_1/a_2 = 10$) for different axial fiber offsets α ; perfect thermal contact.

ivity is less affected (Table 7.2, Fig. 7.5). Considering the effective axial conductivity the staggered arrangement again exhibits a much better performance than the nonstaggered arrangement. While failed end face interfaces reduce the effective axial conductivity by around 30 W/mK for staggered arrangements ($\delta = 1$), for the non staggered arrangements ($\delta = 0$) the reduction amounts to approximately 50 W/mK (Fig. 7.5). The Mori–Tanaka estimates predict a reduction of the effective axial conductivity of approximately 15 W/mK and 50 W/mK for spheroidal and cylindrical inclusions, respectively (Table 7.2). While the hybrid modeling approach based on cylindrical inclusions provides excellent predictions, the model based on spheroids underestimates the impact of the end face failure.

The effective transverse conductivity is reduced only slightly by the presence of the thermal barrier at the end faces (for all arrangements the reduction is less than 0.1%). The Mori–Tanaka results for the transverse behavior agree very well with the unit cell predictions.

Dependence on the Degree of Staggering The influence of the degree of staggering on the effective conductivities is investigated for the case of axial fiber offsets of $\alpha = 0.25$ for perfect thermal interfaces as well as for failure of the cylindrical interfaces and the end face interfaces, respectively. Figure 7.7 shows the results for the effective axial conductivity.

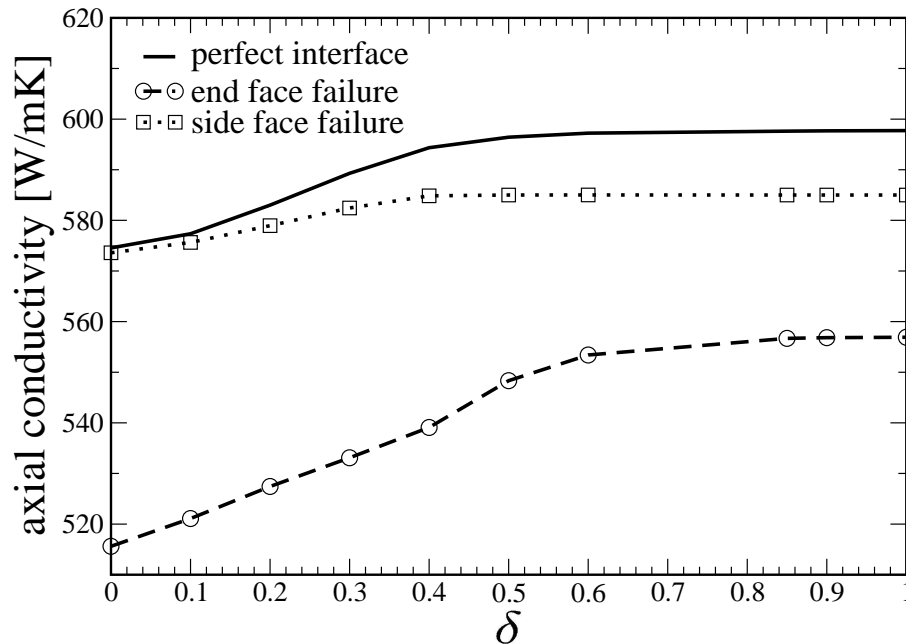


Figure 7.7: Predicted effective axial conductivity of aligned short fiber composites ($\xi^{(i)} = 0.4$, $a_1/a_2 = 10$) with an axial fiber offset of ($\alpha = 0.25$) as function of the degree of staggering and thermal interfaces. The curves correspond to perfect interfaces (solid line), failed end faces (dashed line), and failed side faces (dotted line), respectively.

Considering perfect thermal interfaces the dependence of the axial effective conductivity on the degree of staggering δ is larger in the range of small δ -values ($\delta < 0.4$). As the overlap between neighboring fibers is increased further ($\delta > 0.5$) no significant increase of effective conductivity is gained from further increasing the degree of staggering.

In general the failure of the end face interfaces (perfectly insulating end face interface) reduces the effective axial conductivity more severely than failure of the side face interfaces. Nonstaggered arrangements ($\delta = 0$) are almost independent of the interface conductance of the side face interface. The more staggered an arrangement is, the greater is the dependence of the effective axial conductivity on the side face interface conductance because heat flow through the fibers side faces into the next fiber is the basic mechanism that is responsible for

the better performance of staggered arrangements compared to nonstaggered arrangements. Due to this very mechanism a failure of the end face interface is better compensated by staggered arrangements.

7.2.3 Summary – Aligned Staggered Short Fibers

For carbon–copper composites reinforced with aligned staggered short fibers the effect of micro topology and of selective thermal failure of the end face and side face interfaces on the effective conductivities was studied. It was shown that there is a strong dependence of the micro topology on the effective conductivities. Staggered arrangements perform better in axial direction than do nonstaggered arrangements. For the transverse direction nonstaggered arrangements provide higher overall conductivities than staggered arrangements, but the differences are less pronounced than in the axial direction.

Highly idealized periodic micro arrangements were used that are not fully realistic. Nevertheless useful insight and information on the interdependence of the topological input parameters was gained. Note that the obtained estimates on the effective conductivity can be used as input for determining the effective conductivity of aggregated systems via self consistent methods ??.

When compared to three dimensional unit cells with randomly oriented fibers, the employed unit cells for aligned fibers can be set up relatively easy to meet requirements for high fiber volume fractions and they are not very demanding with regards to computational requirements. The present approach can easily be applied to other micro topologies.

Chapter 8

Results for Randomly Oriented Carbon Fibers

In this chapter carbon–copper composites are investigated that show spatially (three dimensional) random or (approximately) planar random fiber orientations. The main focus is on planar random fiber arrangements. The influence of microgeometrical descriptors on the effective conductivities is comprehensively studied. A unit cell approach as well as a hybrid Mori–Tanaka scheme are employed to obtain estimates on the effective conductivities. Results are compared with measurements.

8.1 Three Dimensional Random Fiber Arrangements

In this section carbon–copper composites with randomly oriented short fibers are investigated. Three types of methods are employed to obtain estimates on the effective conductivity. A multi–inclusion unit cell approach (UC) and an extended multiple discrete orientation Mori–Tanaka approach (MT/m) are used. The latter samples the same discrete fiber orientations as given by the unit cell. Additionally, an extended Mori–Tanaka approach conforming to an ideally random ODF is utilized, MT/3Dr.

Spheroidal and cylindrical fibers are considered in order to allow for studying the influence of fiber shape on the effective conductivity. Perfectly bonded as well as imperfectly bonded constituents are considered.

8.1.1 Generic Unit Cells

Generation of the Unit Cells

The arrangements are taken from [1]. They were generated with by Random Sequential Adsorption (RSA) algorithm, see e.g. [2]. The basic idea of RSA schemes is to sequentially add inclusions to the unit cell volume by generating candidate inclusions at random positions and of random orientation. A candidate inclusion is accepted, if it does not overlap with any previously accepted inclusion. The RSA scheme used for setting up the unit cells has been modified in order to account for user defined minimum distances between neighboring inclusions as well as to account for periodicity of the volume elements. Note that checking against violations of a specified minimum distance is a complex task for nonaligned spheroids and cylinders which can require considerable computational resources. More information on RSA algorithms can be found in [3].

Microgeometry and FE Meshes

Periodic arrangements of 15 fibers of spheroidal and cylindrical shape with an aspect ratio of five and an inclusion volume fraction of $\xi^{(i)} = 0.15$ are employed. In order to allow a direct assessment of fiber shape effects the spheroidal and cylindrical fibers occupy the same positions and have the same orientations. In Fig. 8.1 a matching pair of unit cells is shown. Note that these unit cells have been comprehensively studied in the mechanical context, see [4].

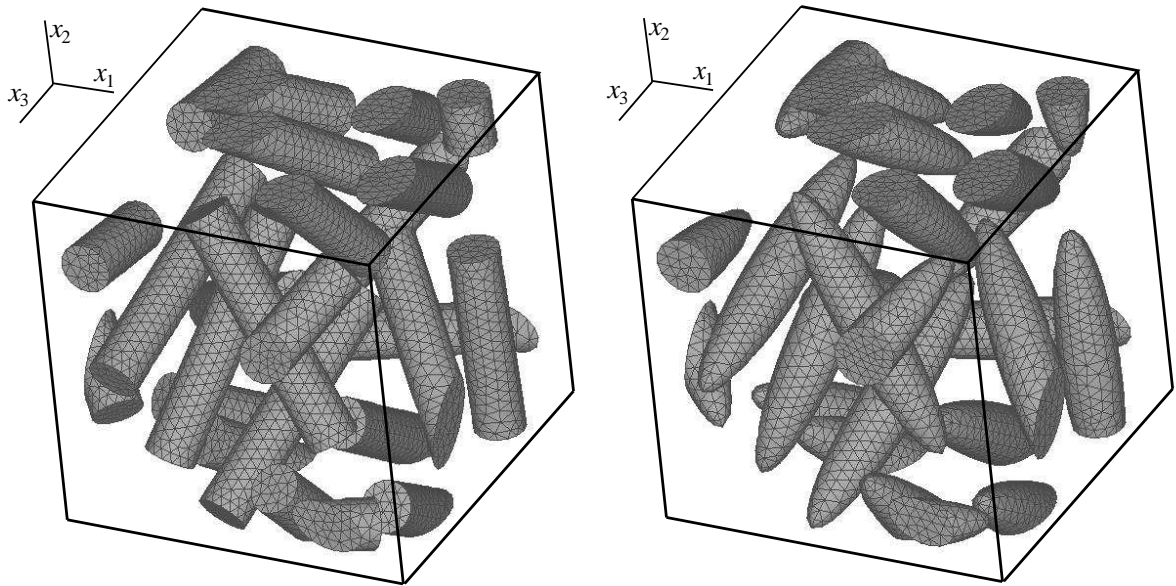


Figure 8.1: Periodic unit cells with randomly positioned and oriented inclusions of cylindrical shape (left) and spheroidal shape (right), both inclusion geometries conforming to an aspect ratio of $a_1/a_2 = 5$. The inclusion volume fraction is $\xi^{(i)} = 0.15$ in both cases.

The model geometry was meshed, and solved with ANSYS 7.0 (ANSYS, Inc., Canonsburg, PA). The matrix volume and inclusion volumes are meshed with approximately 300,000 and 40,000 ten-node tetrahedral elements, respectively, corresponding to an element edge length of approximately $0.35 a_2$, a_2 being the inclusion radius. Some 19,000 constraint equations are employed for constraining nodes on opposite faces of the cells such that compatible temperature profiles are enforced on opposing faces.

8.1.2 Results

The results presented pertain to carbon–copper composites. The heat conduction properties of the constituents are given in Chapter 3, transverse fiber conductivities of 100 W/mK being assumed. The studied cases of interfacial degradation comprise the scenarios *C1* and *C2* as well as *C5* and *C6*, see Table 3.4. The corresponding reduced conductivities and dilute concentration tensors as given in Table 6.2 are used in the Mori–Tanaka evaluations.

Inclusions of Cylindrical Shape

Homogenization Estimates on the effective conductivity of the investigated carbon–copper composite are listed in the top half of Table 8.1. The results are given in terms of principal conductivities, with $K_I^{(*)}$ and $K_{III}^{(*)}$ denoting the maximum and minimum principal conductivities, respectively.

Excellent agreement is found between the FE based unit cell predictions (UC) and the hybrid Mori–Tanaka results with corresponding discrete orientations, (H–MT/m). Note that this also holds true for the off–diagonal terms of the conductivity tensors as given in the “unit cell” coordinate system, i.e. the agreement of the orientation of $K^{(*)}$ is excellent as well.

This shows that the effective field approximation gives excellent results for moderate fiber volume fractions. Additionally, the results clearly support the concept of replacement operations as introduced in Section 5.2 for non–spheroidal fibers with imperfect interfaces. Orthotropic effective conductive behavior is observed, for the case *C1* the maximum and minimum principal conductivity differ by approximately 15%, and for case *C3* by some 5%. Considering cylinders with perfectly bonded side faces in combination with either perfectly conducting (*C1*) or perfectly insulating (*C2*) end faces, the latter gives rise to approximately 5% lower maximum principal conductivities. Comparing the scenarios *C5* and *C6* shows that the reduction of the effective conductivity due to end face failure is less than 1%. Debonding of the cylinders’ side faces reduces the effective conductivities by approximately 20%, which is significantly higher than the reduction due to debonded end faces.

The Mori–Tanaka predictions of the effective conductivities for perfectly randomly oriented cylindrical fibers (H–MT/3Dr, Table 8.1, right row) are always in between $K_I^{(*)}$ and $K_{III}^{(*)}$ and slightly below $K_{II}^{(*)}$ as predicted for the studied microgeometry with discrete fiber orientations. Note that the matrix conductivity of 360 W/mK is never exceeded, i.e. the

Table 8.1: Unit cell predictions (UC) and Mori–Tanaka estimates (MT/m, MT/3Dr) on the effective principal conductivities of a carbon–copper composite with randomly oriented cylindrical and spheroidal short fibers ($a_1/a_2 = 5$, $\xi = 0.15$) for the cases $C1$, $C2$, $C5$, and $C6$ of interfacial degradation.

		UC			MT/m			MT/3Dr
case		$K_I^{(*)}$	$K_{II}^{(*)}$	$K_{III}^{(*)}$	$K_I^{(*)}$	$K_{II}^{(*)}$	$K_{III}^{(*)}$	$K^{(*)}$
		[W/mK]	[W/mK]	[W/mK]	[W/mK]	[W/mK]	[W/mK]	[W/mK]
cylinders	$C1$	374.1	352.2	323.3	374.9	352.9	321.8	349.6
	$C2$	359.3	342.8	319.4	358.9	342.1	318.1	339.5
	$C5$	296.4	288.1	278.7	295.8	288.5	278.3	287.4
	$C6$	294.0	286.5	278.0	293.5	286.9	277.7	285.9
spheroids	$C1$	374.8	352.8	323.0	376.1	353.5	321.7	350.1
	$C2$	–	–	–	374.5	352.4	321.3	349.1
	$C5$	296.4	287.7	278.6	295.8	288.3	277.8	287.2
	$C6$	–	–	–	295.7	288.2	277.8	287.1

poor transverse conductivity of the fibers plays a dominant role.

Localization In Fig. 8.2 normalized averaged temperature gradients of the matrix phase, $\bar{T}_{,i}^{(m)}/T_{,i}^{(*)}$ (no sum over i), (as obtained with the UC and H–MT/m approaches) due to applied far fields along x_i are plotted. The ratio of $\bar{T}_{,i}^{(m)}/\bar{T}_{,i}^{(*)}$ (no sum over i) can be immediately identified as a diagonal component of the Mori–Tanaka concentration tensor of the matrix phase, $\bar{D}_{ii}^{(m)}$ (no sum over i), as defined in Eq. (4.34), Section 4.2.

The Mori–Tanaka scheme (Fig. 8.2, bars) approximates the temperature gradient field of the matrix phase as constant. The magnitudes of the normalized matrix temperature gradient fields vary by less than 5% between the studied cases of interfacial degradation. For perfectly randomly oriented cylinders (H–MT/3Dr) the averaged matrix gradients are $\bar{T}_{,i}^{(m)}/T_{,i}^{(*)} = 0.958$ and $\bar{T}_{,i}^{(m)}/T_{,i}^{(*)} = 0.917$ for scenarios $C1$ and $C5$, respectively. Failure of the end face interfaces reduces the matrix gradients insignificantly. The circles in Fig. 8.2 show the averaged temperature gradient of the matrix phase as obtained from the unit cell analyses. The vertical bars indicate the corresponding standard deviation. Excellent agreement between the Mori–Tanaka method and the unit cell approach is found for the averaged matrix temperature gradients. The standard deviation is noticeably higher for $C5$ and $C6$ than for $C1$ and $C2$.

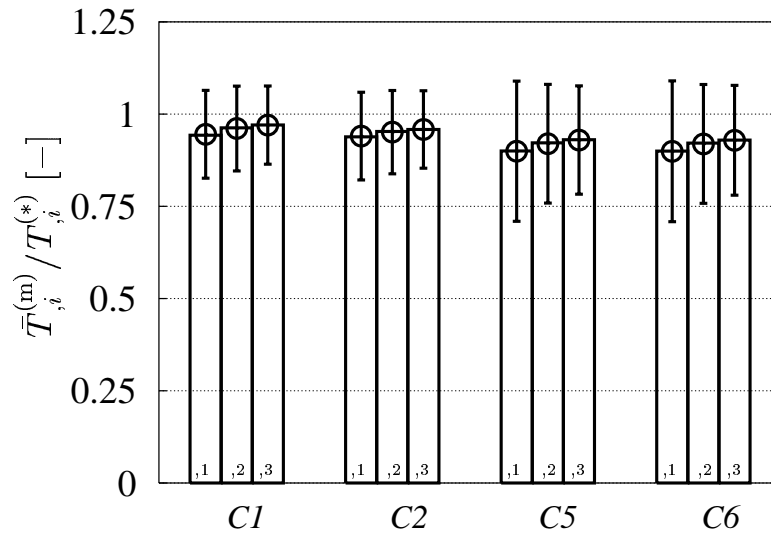


Figure 8.2: Normalized matrix temperature gradients due to applied far field gradients along x_i as predicted with the unit cell method (UC, circles with bars) and a hybrid Mori–Tanaka method with multiple discrete fiber orientation (H–MT/m, bars) for different scenarios of interfacial degradation for an C/Cu composite with randomly oriented short fibers ($\xi^{(i)} = 0.15$, $a_1/a_2 = 5$).

The magnitude of the matrix gradients decreases as the conductivity of the replacement inclusion phase is decreased (i.e. increasing interfacial thermal resistances). Note also that the diagonal terms of the matrix concentration tensor, $\bar{D}_{ii}^{(m)}$ (no sum over i) do not exceed unity, typically indicating that the inclusions are more resistive than the matrix. It is found that the maximum principal conductivity $K_I^{(*)}$ points in the direction of x_3 , this fact is also reflected in the matrix concentration tensor, $\bar{D}_{33}^{(m)}$ being the largest entry.

The averaged temperature gradients of individual cylindrical inclusions are studied for the case *C1* and *C5* for applied far field gradients along each unit cell axis. The angle θ subtended between the gradient forced upon the unit cell and the fibers' axes of rotation is sufficient to uniquely characterize the orientations of the fibers with respect to $T_i^{(*)}$ ¹. The solid circles in Fig. 8.3 show the estimates of the averaged inclusion fields as predicted with the hybrid multiple discrete orientations Mori–Tanaka scheme (H–MT/m) for case *C1*, the circles corresponding to the mean values obtained from the unit cell predictions

¹Each fiber is represented three times with its characteristic response to each of the three applied far field gradients.

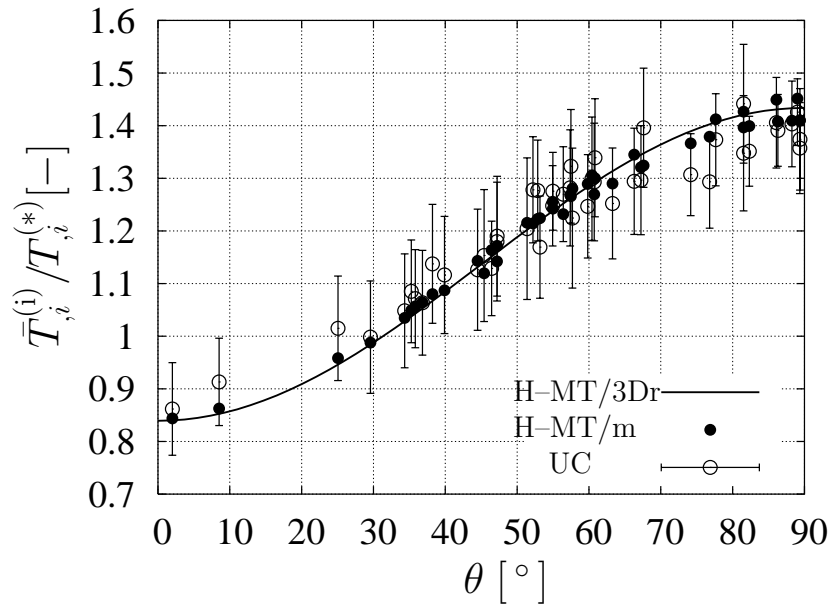


Figure 8.3: Hybrid, multiple discrete orientation Mori–Tanaka results (H–MT/m, solid circles) as well as unit cell results (UC, circles with bars) for the orientation dependence of the temperature gradients in fibers of an C/Cu composite with ideal interfaces subjected to far field temperature gradients of unit value. Mori–Tanaka results for perfectly randomly oriented fibers are shown as the solid line (H–MT/3Dr).

(UC) and the bars indicate the corresponding standard deviations. Good agreement is observed. For small angles θ the unit cell approach (UC) predicts slightly higher inclusion gradients than does the hybrid Mori–Tanaka approach (H–MT/m), and for $\theta > 50^\circ$ the unit cell predictions are slightly below the hybrid Mori–Tanaka predictions. The standard deviations of the temperature gradients within the individual fibers reach up to approximately 10% percent of the respective mean values.

Additionally the averaged inclusion gradients for perfectly randomly oriented cylindrical inclusions are plotted (solid line, H–MT/3Dr). The inclusion gradients associated with the latter microgeometry agree very well with those associated with the studied “pseudo-random” arrangement modelled with 15 discrete orientations (H–MT/m). This is due to the good agreement of the matrix concentration tensors associated with the two microgeometries.

Also a marked variation of $\bar{T}_i^{(i)}$ with the fiber orientation is evident. Inclusions oriented with the applied far field gradient exhibit small temperature gradients due to the high conductivity in axial direction and high inclusion gradients are induced in those which are

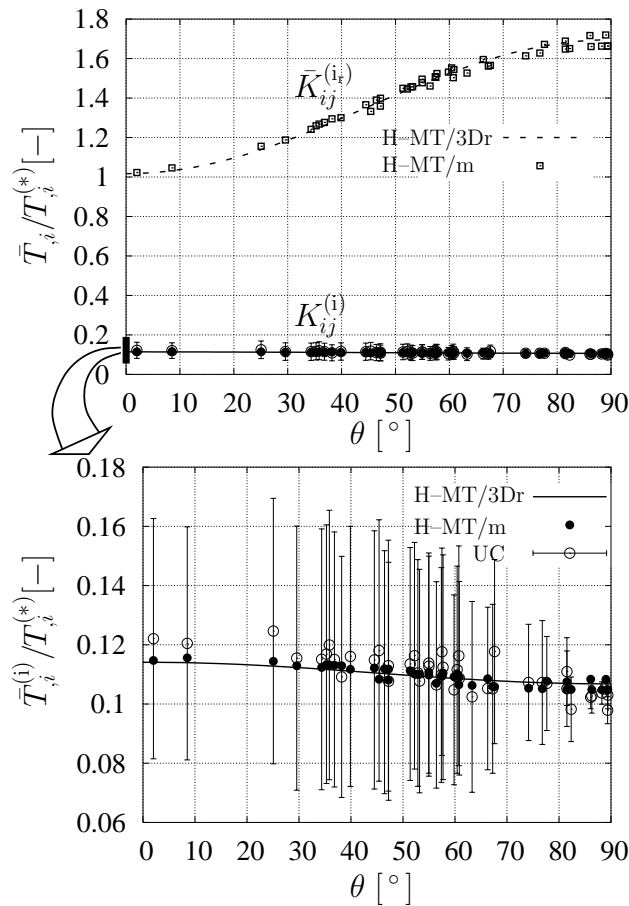


Figure 8.4: Hybrid, multiple discrete orientation Mori–Tanaka results (H–MT/m, solid circles) as well as unit cell results (UC, circles with bars) for the orientation dependence of the temperature gradients in fibers of an C/Cu composite with imperfect interfaces and the corresponding gradients in perfectly bonded replacement inclusions (squares) subjected to far field temperature gradients of unit value. Mori–Tanaka results for perfectly randomly oriented fibers are shown as a solid line (H–MT/3Dr).

oriented perpendicularly to the applied far field due to the low transverse conductivity compared to the matrix conductivity.

For scenario *C5* of interfacial degradation the corresponding inclusion averages are depicted in Figs. 8.4. The squares in the top half of Fig. 8.4 show the apparent inclusion gradients which are induced in the weakly conductive replacement cylinders. The dashed line shows the averaged gradients for perfectly randomly distributed cylinders. Good agreement is observed again. However, these results cannot be compared with predictions from the unit cell analysis. Equation (5.30) must be used to zoom in on the actual inclusion

fields. The solid circles in Fig. 8.4, top and bottom show the gradients in the imperfectly bonded inclusions. Again good agreement between the unit cell predictions (UC) and the hybrid multiple discrete orientation Mori–Tanaka predictions (H–MT/m) is observed.

The solid line in the bottom half of Fig.8.4 shows the actual temperature gradients for randomly oriented inclusions, H–MT/3Dr. The variation of the inclusion gradients with θ is much smaller for the imperfectly bonded cylinders, because the reduction of the temperature gradients due to imperfect interfaces is about 9 for fibers oriented parallel to the far field ($\theta = 0^\circ$) and approximately 15 for fibers oriented perpendicular to the applied far field ($\theta = 90^\circ$).

Plots of the temperature gradient for the scenarios *C1* and *C5* due to applied far field gradients of unit value along x_1 are shown in Fig. 8.5 and Fig. 8.6.

For the case of perfectly bonded constituents (*C1*, Fig. 8.5) the temperature gradients in the inclusions are of comparable magnitude to the matrix temperature gradients. Marked intra–inclusion fluctuations of the inclusion temperature gradients can be observed due to interaction of neighboring inclusions. With increasing misalignment of a given inclusion with respect to the applied far field gradient $T_{,1}^{(*)}$ the inclusion temperature gradients $T_{,1}^{(i)}$ increase.

For the case of imperfectly bonded constituents (*C5*, Fig. 8.6) the temperature gradients in the inclusions are about an order of magnitude smaller than the matrix temperature gradients. This is due to the presence of the interfacial thermal resistances which effectively “excludes” fibers from heat conduction and thus gives rise to small inclusion temperature gradients.

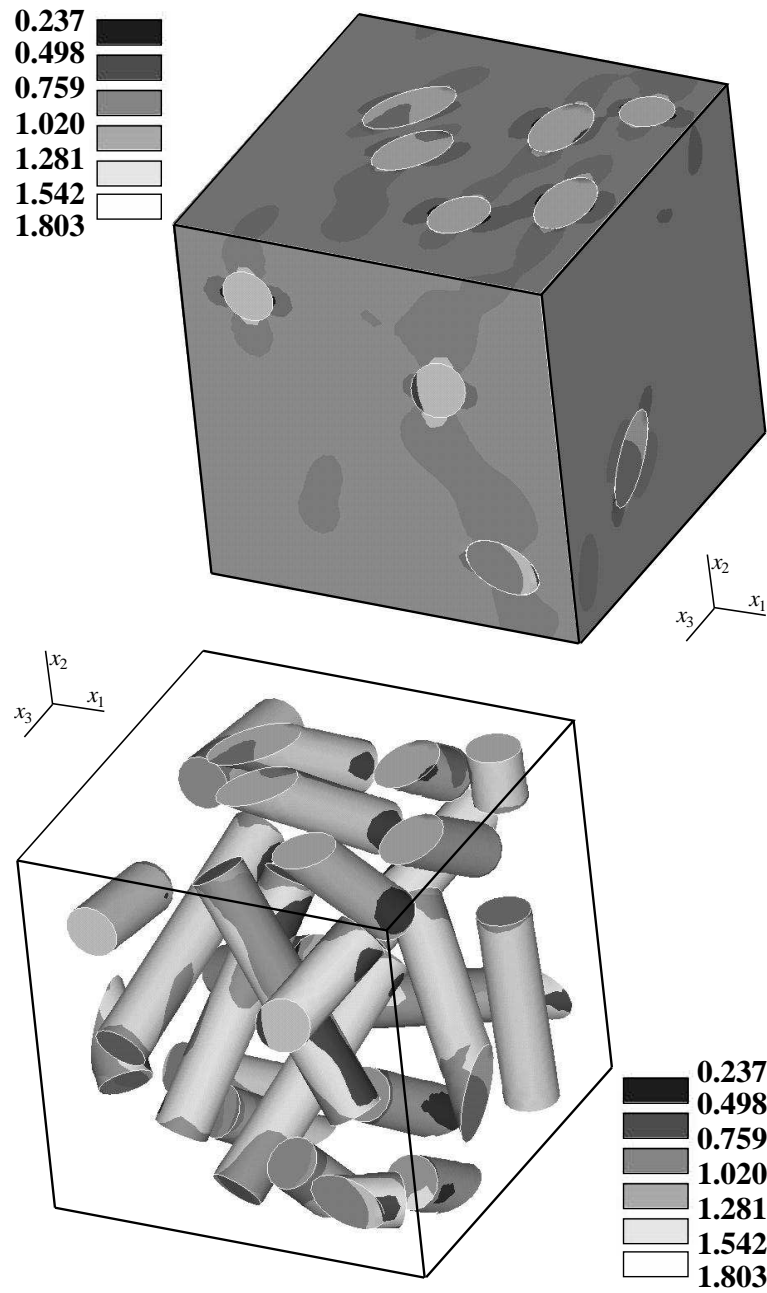


Figure 8.5: Predicted distribution of the temperature gradients in the matrix phase, $T_{,1}^{(m)}$ (top), and inclusion phase, $T_{,1}^{(i)}$ (top and bottom), due to an applied far field gradient $T_{,1}^{(*)} = 1$ K/m of a C/Cu composite ($\xi^{(i)} = 0.15$, $a_1/a_2 = 5$) with perfect thermal interfaces ($\beta \rightarrow \infty$).

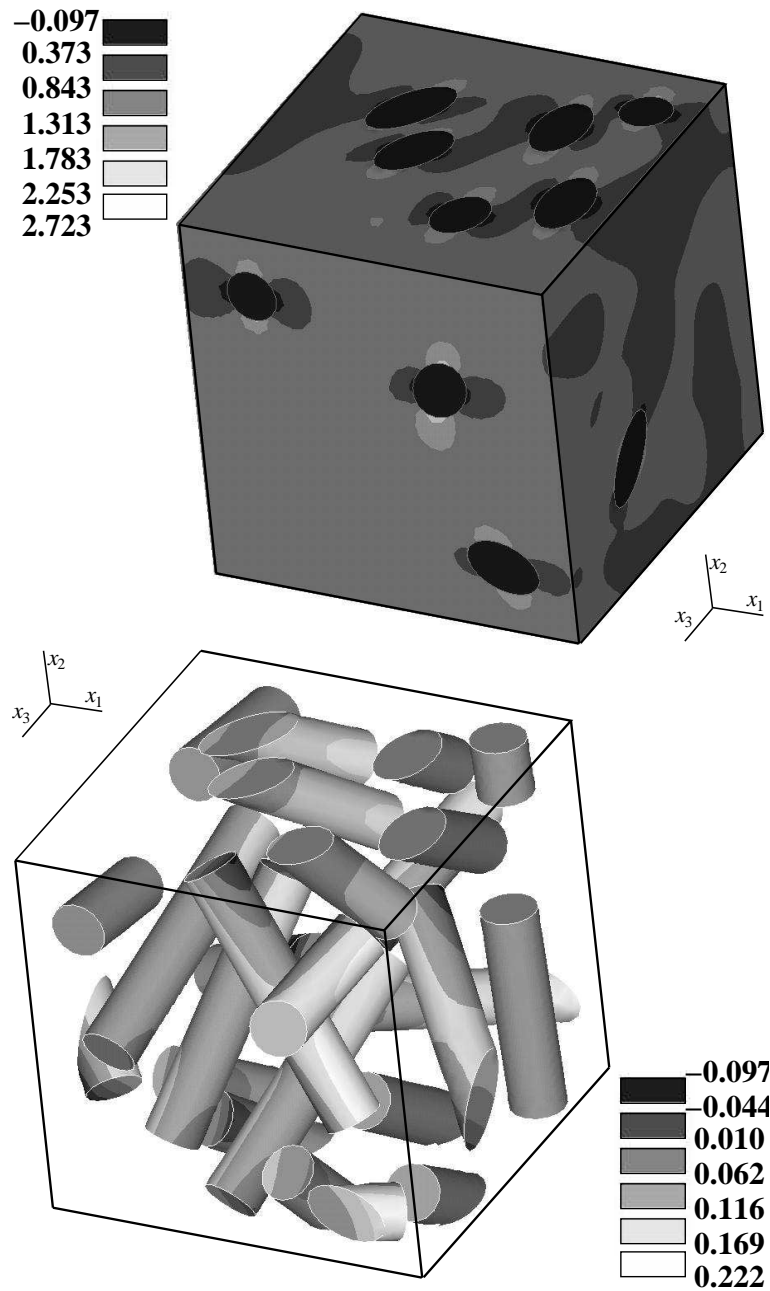


Figure 8.6: Predicted distribution of the temperature gradients in the matrix phase, $T_{,1}^{(m)}$ (top), and inclusion phase, $T_{,1}^{(i)}$ (top and bottom), due to an applied far field gradient $T_{,1}^{(*)} = 1$ K/m of a C/Cu composite ($\xi^{(i)} = 0.15$, $a_1/a_2 = 5$) with imperfect thermal interfaces ($\beta = 1.33 \times 10^6$, $a_2 = 5 \mu\text{m}$).

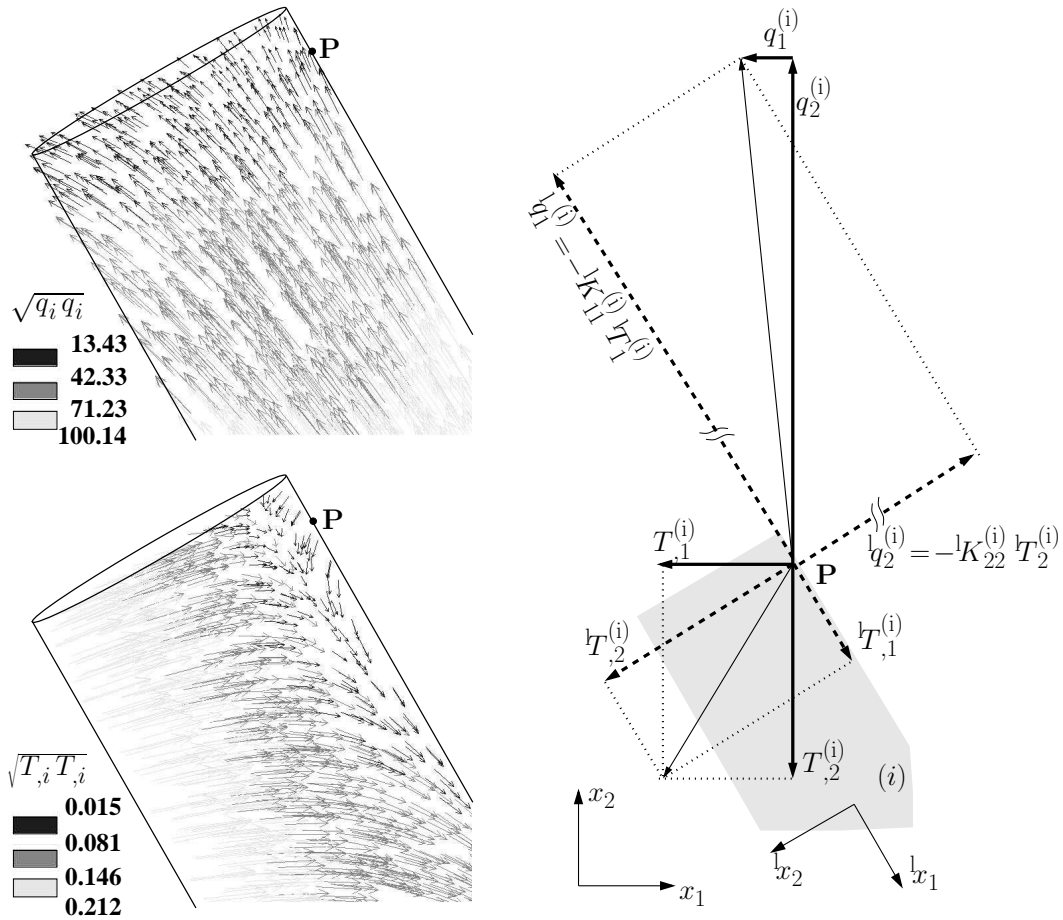


Figure 8.7: Vector plots of the flux field (top left) and temperature gradient field (bottom left) in the end face–side face region of a carbon fiber embedded in a copper matrix with oblique orientation to the applied far field gradient of unit value as predicted by a unit cell model. The temperature gradient vector and flux vector in the point P (located next to the interface in the transversally isotropic carbon fiber) in the global coordinate system and the local inclusion coordinate system are depicted with solid thick lines and dashed thick lines, respectively (right).

The existence of negative inclusion gradients $T_{,1}^{(i)} < 0$ (pointing in the opposite direction of the applied far field gradient) in the end face areas of fibers with oblique orientations with respect to the far field gradient is noteworthy. The left hand side of Fig. 8.7 shows two vector plots of a corresponding pair of temperature gradient and flux fields predicted for a fiber which is misaligned around 35° to $T_{,1}^{(*)}$ and is oriented parallel to the x_1 – x_2 –plane. On account of the latter characteristic x_3 –components can be neglected and for the analysis the problem can be treated in a two–dimensional context. While the flux

field satisfies $q_1^{(i)} < 0$ the related temperature gradient field $T_{,1}^{(i)}$ changes its sign. This apparent paradoxon can be resolved by taking into account the transversal isotropy of the inclusions. On the right hand side of Fig. 8.7 the state of the point P on the matrix–inclusion interface is plotted. The thick solid lines represent the components of the flux and temperature gradient with respect to the global coordinate system, whereas the thick dashed lines depict the corresponding flux and temperature gradient in the local inclusion coordinate system, ${}^1q_i^{(i)}$ and ${}^1T_{,i}^{(i)}$. The flux and temperature gradient can be easily correlated in the local inclusion coordinate system by employing Fourier’s law, revealing that for the studied case (${}^1K_{11}^{(i)}/{}^1K_{22}^{(i)} = 1000/100$) negative inclusion gradients along x_1 may indeed occur, while the inclusion flux field does not change its sign at any point. Note that an additional thermal failure of the end face interface can cause fluxes of inverted (positive) direction in the end face region of cylindrical fibers as well.

Inclusions of Spheroidal Shape

For the scenarios *C1* and *C5* unit cell estimates (UC) as well as multiple discrete orientation Mori–Tanaka estimates (E–MT/m) on the effective conductivity are obtained for spheroidal inclusions. In addition, the Mori–Tanaka procedure is utilized to estimate the effective conductivity for the scenarios *C2* and *C6* and spheroidal fibers. For that purpose “artificial” or “pseudo” end faces allocated to the spheroids. They are chosen such that the ratio of end face area over side face area of both cylinders and spheroids are the same. The averaging procedure as proposed in Section 5.1 is employed to obtain estimates on the reduced conductivities of the replacement inclusions.

Homogenization Excellent agreement between the unit cell predictions (UC) and the Mori–Tanaka predictions (E–MT/m) for the effective conductivity for scenarios *C1* and *C5* is observed, Table 8.1. It is also evident that for the above scenarios, which pertain to a uniform interface parameter, the influence of the inclusion shape (cylindrical or spheroidal) has no significant influence on the effective conductivities for the chosen material properties and aspect ratio.

The Mori–Tanaka predictions (E–MT/m) for the effective conductivity pertaining to the scenarios *C2* and *C6* are noticeably above the corresponding conductivities as obtained with cylinders (H–MT/m).

While spheroids capture the behavior of cylinders very well for the studied conductive properties of the constituents in combination with either perfect thermal interfaces or

uniform distribution of the interfacial thermal resistance, it turns out that spheroids with pseudo end faces are a poor model for the simulation of cylinders when a selective failure of the end face interfaces is to be modelled.

Localization The averaged matrix temperature gradient fields, $T_{,i}^{(m)}$, and standard deviation as resulting from spheroids and cylinders are almost identical, the difference being less than 1%.

8.2 Planar Random Fiber Arrangements

In this section carbon–copper composites with fibers that show random orientation in the x_2 – x_3 –plane plus some out–of–plane misalignment are investigated (“planar random fiber arrangements”). For this purpose two periodic unit cells of appropriate microstructure are studied.

For the case of perfect thermal interfaces the unit cell predictions (UC) for the effective conductivity are compared with estimates obtained with a hybrid multiple discrete orientation Mori–Tanaka scheme (H–MT/m). Inclusion gradient fields of individual inclusions are investigated with both approaches. Additionally, predictions from hybrid Mori–Tanaka schemes are provided for carbon–copper composites with perfectly planar randomly distributed fibers (H–MT/2Dr). For that specific fiber microarrangement six different cases of interfacial degradation (Table 3.4) as well as the influence of the transverse fiber conductivity are studied.

8.2.1 Generic Unit Cells

Generation of Unit Cells

The periodic fiber arrangements were generated with the simulation software PALMYRA (Materials Simulation GmbH, Zürich, Switzerland). A predefined number of fibers conforming to a chosen range of allowable orientations is initially arranged in a cuboidal base cell. The size of the latter is chosen sufficiently large in the beginning such that non–interpenetrating fiber arrangements can be set up by random insertion algorithms ?. Subsequently, by “shaking” the fibers and compressing the base cell the fiber volume fraction is steadily increased – a Monte Carlo algorithm ?? randomly moves the fibers within the cell as the latter’s size is decreased while checking for fulfilling a predefined minimum distance between neighboring fibers. Periodicity of the microstructure is maintained automatically as the volume fraction is increased steadily.

For generating planar random fiber arrangements, the base cell is compressed in one direction only, in an attempt to approximate the compaction process during hot pressing as realistically as possible within the limits of the chosen simulation tool. Simulations of breaking of the fibers during compaction are out of the scope of the present work. Accordingly, specific aspect ratio distributions must be defined *before* compressing the base cell. The maximum attainable volume fractions are moderate due to two key issues. On the

one hand a minimum fiber to fiber distance must be maintained so the element counts of the meshed microgeometry stay within reasonable limits. On the other hand aggregates of aligned fibers are typically required for attaining high volume fractions. Such arrangements are not used in the present study due to limitations in the number of fibers per unit cell that can be handled computationally. Some increase in the fiber volume fractions can be achieved with fibers of variable length compared to fibers of constant size. The closer the fiber aspect ratio is to unity the higher are the maximum attainable volume fractions for non aligned fibers. Note that in Palmyra “capped cylinders” (cylinders with hemispherical end caps) are used. For the present study, however, only the cylinder “bodies” are employed, which further reduces the attainable volume fractions.

Microgeometrical Characteristics

Two periodic unit cells with similar microgeometries were generated. They are referred to as CELL 1 and CELL 2, respectively. Both unit cells pertain to inclusion volume fractions of approximately 21%. The inclusions are cylinders of the same size with an aspect ratio $a_1/a_2 = 10$. CELL 1 and CELL 2 contain 48 fibers and 40 fibers, respectively.

In Table 8.2 the final dimensions of the unit cell cuboids of CELL 1 and CELL 2 are compared in terms of the fiber radii. The relative height (L_2/L_1) of CELL 2 is approximately 1.5 times that of CELL 1. The fiber volume fractions of CELL 1 and CELL 2 differ by less than one percent.

For assessment and comparison of the fiber orientation statistics the angles Ψ_1 and Ψ_2 (Appendix A) are assessed in a first step. Due to the symmetry properties of the fibers the in-plane angle Ψ_2 can be condensed into in-plane orientations ψ_2 , ranging from 0° to 180° . Out-of-plane deviations are described by $\psi_1 = |90^\circ - \Psi_1|$. Both in-plane orientations, ψ_2 , and out-of-plane deviations, ψ_1 , can be visualized in terms of histograms. For that

Table 8.2: Comparison of CELL 1 and CELL 2 with respect to the number of inclusion cylinders, the total inclusion volume fraction and the unit cell cuboid dimensions.

	CELL 1	CELL 2
number of fibers	48	40
$1 - \xi^{(m)}$	0.209	0.207
$L_1 \times L_2 \times L_3$	$11.70 a_2 \times 35.11 a_2 \times 35.11 a_2$	$14.50 a_2 \times 29.04 a_2 \times 28.99 a_2$

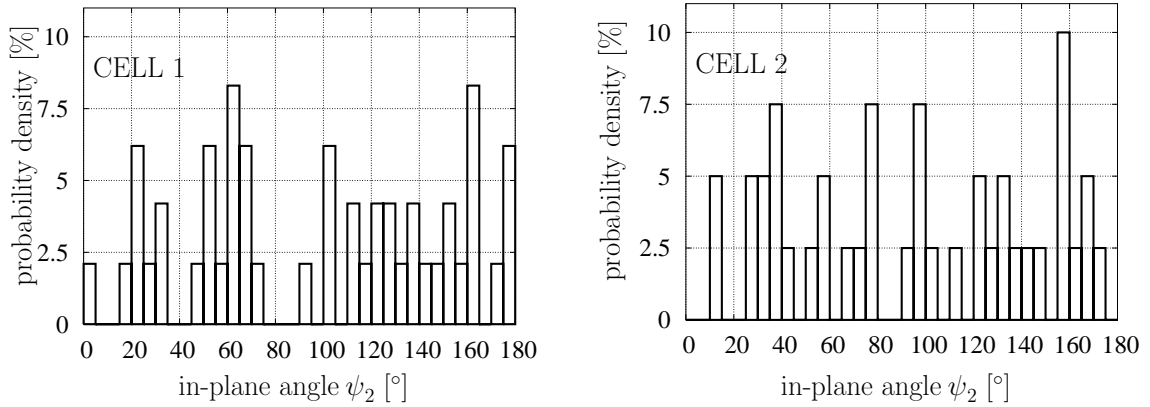


Figure 8.8: Probability density histograms of the in-plane orientations for the microgeometries CELL 1 (left) and CELL 2 (right).

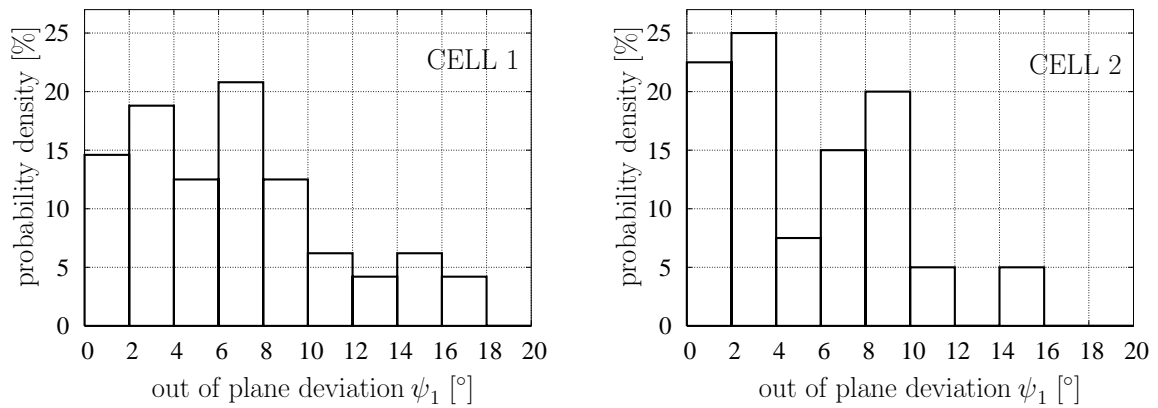


Figure 8.9: Probability density histograms of the out-of-plane deviations for the microgeometries CELL 1 (left) and CELL 2 (right).

purpose the angles ψ_i are partitioned into segments, $\Delta\psi_i$ and the percentage of the number of fibers being oriented within a segment in relation to the total amount of fibers is used to approximate the probability density.

Figure 8.8 shows the dependence of the fiber orientation probability densities on the in-plane orientation ψ_2 , the sampling width of the in-plane angle being $\Delta\psi_2 = 5^\circ$. The probability density distributions for the out-of-plane angles ψ_1 for both investigated microgeometries are displayed in Fig. 8.9, the sampling width being $\Delta\psi_1 = 2^\circ$.

Finite Element Meshes

The positions and orientations of the fibers were extracted from Palmyra and subsequently the unit cells were set up and meshed with 10 node tetrahedral elements using ANSYS 7.0 (ANSYS, Inc., Canonsburg, PA), the element counts for both unit cells reaching more than 1,000,000. CELL 1 and CELL 2 account for around 1,300,000 and 1,200,000 degrees of freedom, respectively, and more than 40,000 constraint equations are employed.

Figures 8.10 and 8.11 show element plots of both matrix and inclusion elements (top) and fiber elements only (bottom) for CELL 1 and CELL 2, respectively.

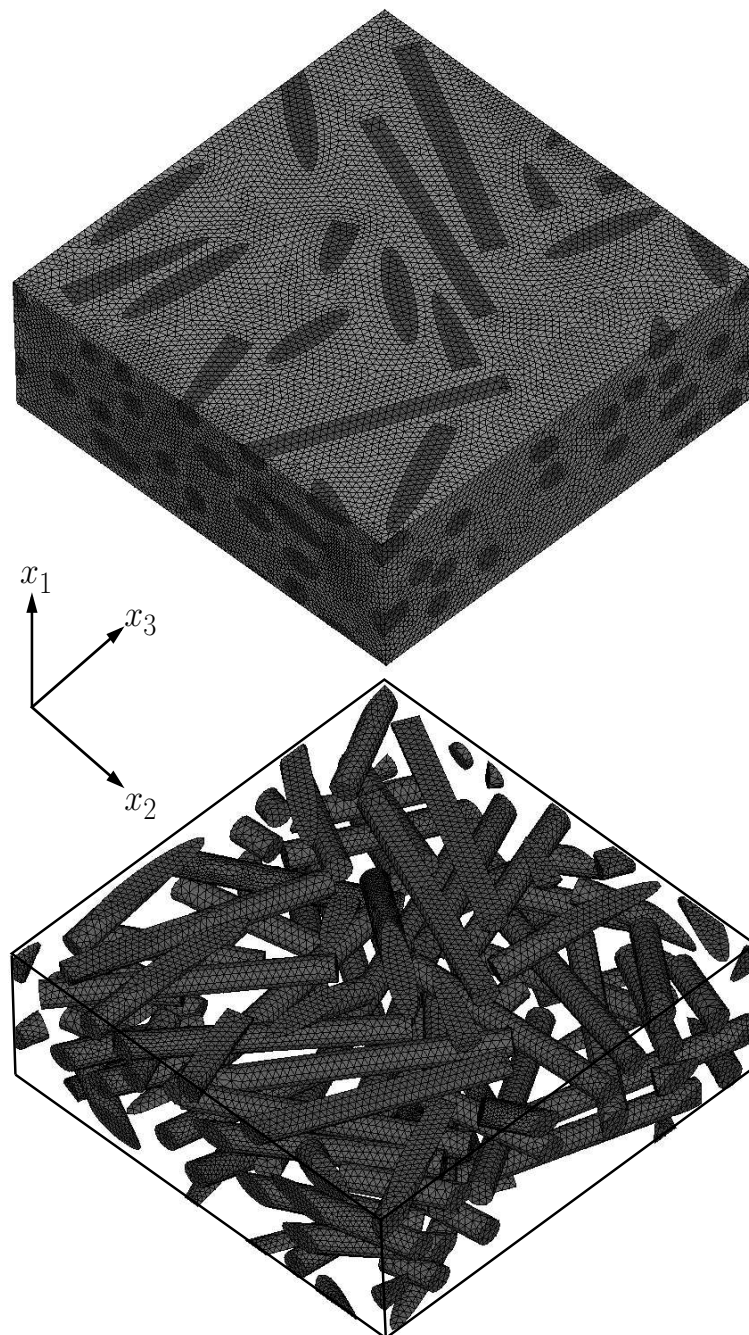


Figure 8.10: Periodic unit cell CELL 1 with a planar random fiber arrangement of 48 cylindrical short fibers ($a_1/a_2 = 10$). The fiber volume fraction is $\xi = 0.209$.

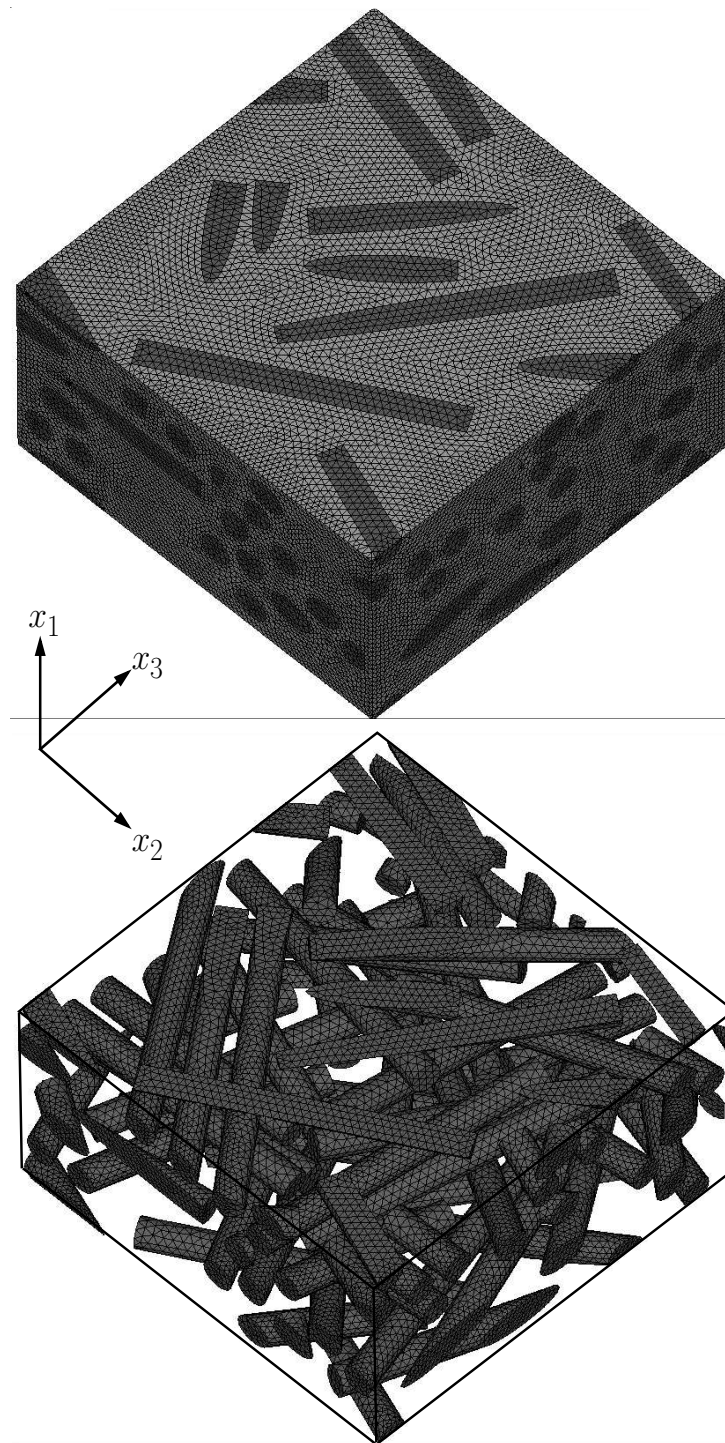


Figure 8.11: Periodic unit cell CELL 2 with a planar random fiber arrangement of 40 cylindrical short fibers ($a_1/a_2 = 10$). The fiber volume fraction is $\xi = 0.207$.

8.2.2 Results for Perfect Thermal Interfaces

The effective conductivities of the microgeometries CELL 1 and CELL 2 are estimated with a unit cell approach (UC) and a hybrid multiple discrete orientation Mori–Tanaka approach (H–MT/m) for the case of perfect thermal interfaces. The tensors of the effective conductivities are given with respect to the global Cartesian coordinate system as defined by the unit cell cuboids.

For CELL 1 the unit cell predictions and Mori–Tanaka predictions are evaluated as

$${}^{\text{UC}}K^{(*)} = \begin{pmatrix} 289.8 & 1.4 & -1.4 \\ 1.4 & 370.8 & 0.2 \\ -1.4 & 0.2 & 378.9 \end{pmatrix} \quad {}^{\text{MT/m}}K^{(*)} = \begin{pmatrix} 288.7 & 1.7 & -1.3 \\ 1.7 & 374.6 & 2.1 \\ -1.3 & 2.1 & 381.5 \end{pmatrix} \quad (8.1)$$

and for CELL 2 as

$${}^{\text{UC}}K^{(*)} = \begin{pmatrix} 289.1 & -3.2 & -0.2 \\ -3.2 & 378.8 & 2.2 \\ -0.2 & 2.2 & 375.1 \end{pmatrix} \quad {}^{\text{MT/m}}K^{(*)} = \begin{pmatrix} 288.3 & -3.3 & -0.1 \\ -3.3 & 379.9 & 1.0 \\ -0.1 & 1.0 & 377.0 \end{pmatrix} \quad (8.2)$$

respectively. Excellent agreement is found between the unit cell results and the results obtained with the hybrid multiple discrete orientation Mori–Tanaka method both of which sample the same fiber orientations as the unit cell. The unit cell predictions (UC) for the effective out-of-plane conductivities, $K_{11}^{(*)}$, are slightly higher than the predictions of the hybrid Mori–Tanaka method (H–MT/m) for both microgeometries. The in-plane conductivities, $K_{22}^{(*)}$ and $K_{33}^{(*)}$, differ by less than 2.5% and 1% for CELL 1 and CELL 2, respectively, indicating satisfactory approximations of planar random fiber orientation distributions. The fact that $K_{33}^{(*)} > K_{22}^{(*)}$ for CELL 1 and $K_{33}^{(*)} < K_{22}^{(*)}$ for CELL 2 can be directly understood in terms of the in-plane fiber orientation probability density histograms, Fig. 8.8, which indicate weak fiber populations around $\psi_2 = 90^\circ$ and $\psi_2 = 0^\circ/180^\circ$ for CELL 1 and CELL 2, respectively.

In Table 8.3 the principal components of the effective conductivities (the suffixes I and III correspond to the maximum and minimum principal conductivity, respectively) as given in Eqs. (8.1) and (8.2) are listed. Additionally, effective conductivities of a composite with a perfect planar random distribution of fibers (i.e. the orientation distribution in ψ_1 is a Dirac–delta) with the corresponding aspect ratio and volume fraction ($\xi = 0.208$) are provided, the predictions being obtained with a hybrid Mori–Tanaka approach (H–MT/2Dr). The latter case gives rise to the lowest effective out-of-plane conductivity, ${}^{\text{MT/2Dr}}K_{11}^{(*)}$, as the high axial fiber conductivity is not available in the out-of-plane direction.

Table 8.3: Unit cell results (UC) and hybrid Mori–Tanaka estimates (H–MT/m) for the effective principal conductivities of a carbon copper composite with microtopologies as given by CELL 1 and CELL 2, respectively (see Fig. 8.10 and Fig. 8.11). Hybrid Mori–Tanaka predictions (H–MT/2Dr) for a planar random distribution of fibers ($\xi = 0.208$) are given for comparison. For the material data see Tables 3.1 and 3.2, $K_{22}^{(i)} = 100$ W/mK.

method, topology	$K_{11}^{(*)} = K_{III}^{(*)}$ [W/mK]	$K_I^{(*)}$ [W/mK]	$K_{II}^{(*)}$ [W/mK]
UC, CELL 1	289.8	378.9	370.8
H–MT/m, CELL 1	288.6	382.1	374.0
UC, CELL 2	289.0	379.9	374.1
H–MT/m, CELL 2	288.2	380.3	376.7
H–MT/2Dr	285.5	379.9	379.9

The isotropic in–plane conductivity, on the other hand, is very high, almost reaching the maximum in–plane conductivity of the orthotropic “comparison–topologies” as described by CELL 1 and CELL 2.

The averaged temperature gradients of individual cylindrical fibers due to far field gradients along the unit cells’ axes are investigated as well. The angle θ subtended between the gradient forced upon the unit cell and the fiber axis is sufficient to uniquely characterize the orientation of a given fiber with respect to the applied far field gradient, $T_{,i}^{(*)}$. The circles in Figs. 8.12 and 8.13 show the estimates of the averaged inclusion fields $\bar{T}_{,i}^{(i)}$ due to $T_{,i}^{(*)}$ as obtained from the unit cell analyses, the bars indicating the respective standard deviations.

The dashed and solid lines correspond to the hybrid Mori–Tanaka estimates. The solid line relates to fibers with perfect planar random orientation distribution, H–MT/2Dr. Note that the corresponding results on the gradients induced in fibers with some out–of–plane deviation (Fig. 8.13) are typical “ghost–inclusion” gradients, as these fibers do not conform to the ODF of the inclusion phase. The dashed line shows induced inclusion gradients corresponding to the microgeometries CELL 1 and CELL 2, H–MT/m. Note that, while for a perfect planar random fiber ODF the inclusion gradients $T_{,1}^{(i)}$ are independent of Ψ_2 , they do depend on the in–plane angle Ψ_2 for orthotropic in–plane conductivities ($K_{22}^{(*)} \neq K_{33}^{(*)}$)².

²For the plot of $T_{,1}^{(i)}$ in Fig. 8.13 a constant in–plane angle of $\Psi_2 = 0^\circ$ is chosen.

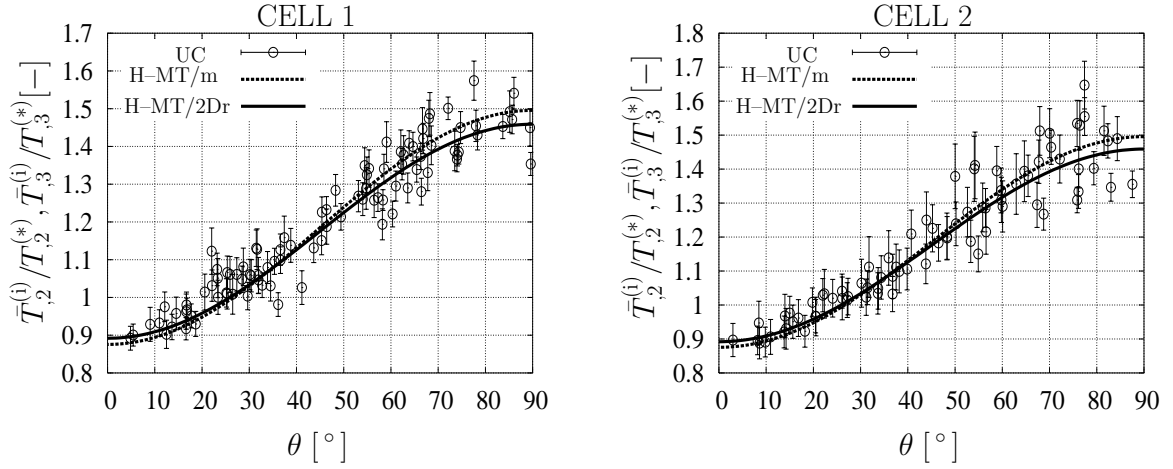


Figure 8.12: Unit cell predictions (circles) and corresponding hybrid Mori–Tanaka predictions (dashed line, H–MT/m) for CELL 1 (left) and CELL 2 (right) as well as hybrid Mori–Tanaka predictions for perfect planar random fiber arrangements (solid line, H–MT/2Dr) for the dependence of the normalized thermal gradients in the fibers, $\bar{T}_{2,2}^{(i)}/T_{2,2}^{(*)}$ and $\bar{T}_{3,3}^{(i)}/T_{3,3}^{(*)}$, on the in–plane orientation of the fibers.

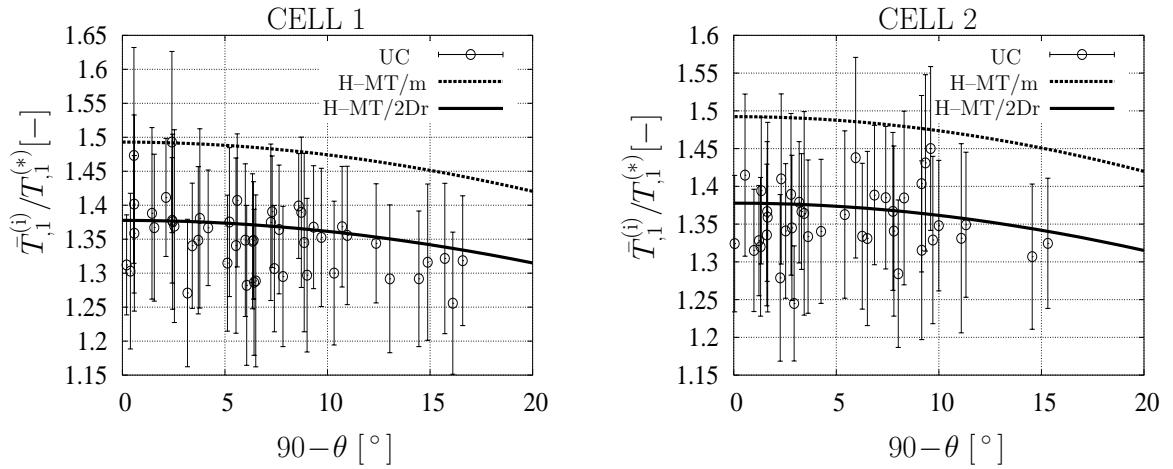


Figure 8.13: Unit cell predictions (circles) and corresponding hybrid Mori–Tanaka predictions (dashed line, H–MT/m) for CELL 1 (left) and CELL 2 (right) as well as hybrid Mori–Tanaka predictions for in–plane perfect random distributed fiber arrangements (solid line, H–MT/2Dr) for the dependence of the normalized thermal gradients in the fibers, $\bar{T}_{1,1}^{(i)}/T_{1,1}^{(*)}$, on the out–of–plane orientation of the fibers.

For CELL 1 and CELL 2, however, this dependence is negligible due to the near isotropy of the in-plane conductivities.

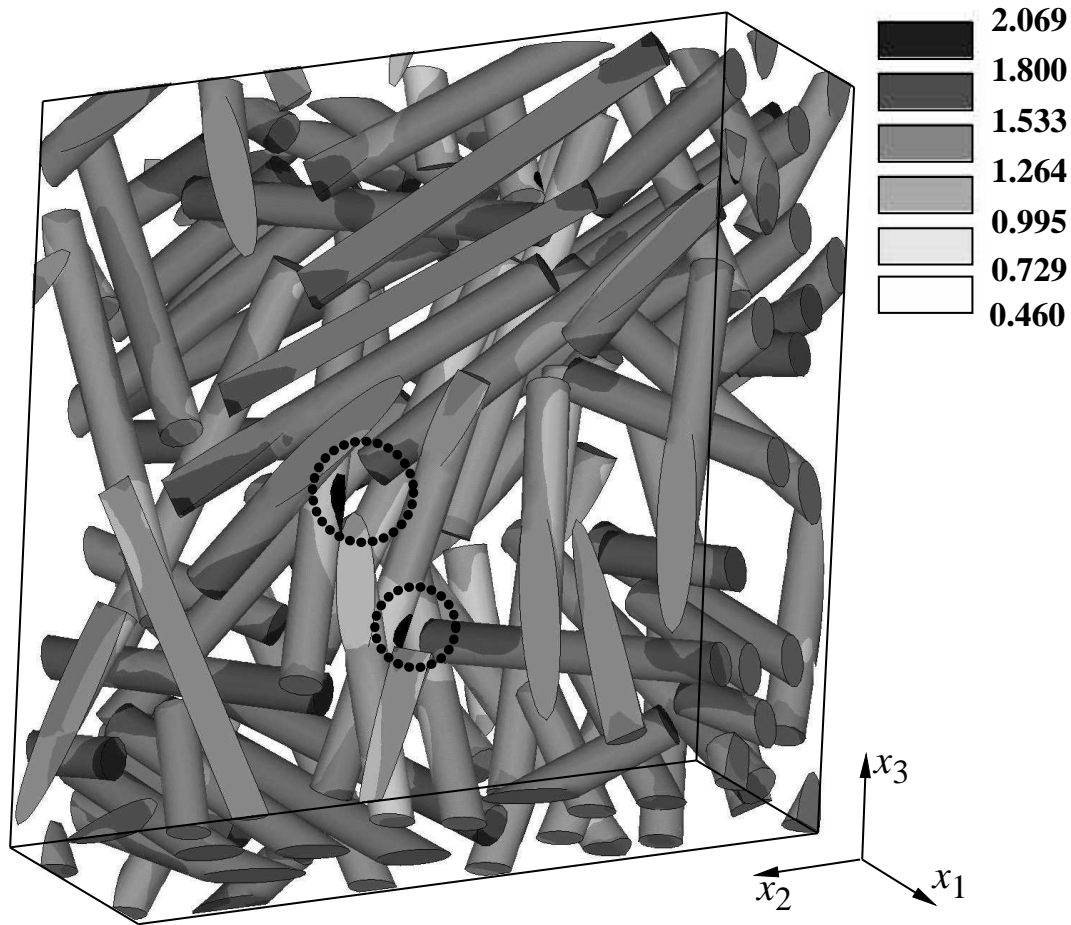


Figure 8.14: Unit cell predictions for the distributions of the temperature gradient field, $T_{,2}^{(i)}$ of the carbon fibers due to an applied far field gradient of $T_{,2}^{(*)} = 1.0$ K/m. (CELL 1, $\xi = 0.209$, 48 cylindrical short fibers, $a_1/a_2 = 10$)

Figure 8.14 shows the distribution of the temperature gradients in the fibers, $T_{,2}^{(i)}$, due to an applied far field gradient of $T_{,2}^{(*)} = 1.0$ K/m as predicted by the unit cell method for the arrangement CELL 1 and Fig. 8.15 shows the distributions of inclusion gradients $T_{,3}^{(i)}$ due to an applied far field gradient of $T_{,3}^{(*)} = 1.0$ K/m as predicted for the arrangement CELL 2. In both figures temperature gradient concentrations can be identified at locations where the ends of fibers that are (nearly) aligned with the far field gradient closely approach the side faces of fibers that are oriented (approximately) perpendicularly to the applied far field gradient. The reason for this effect is the transversal isotropy of the fibers. For the chosen conduction properties of carbon a given heat flux is tied to gradients that are ten times larger in the radial than in the axial fiber direction.

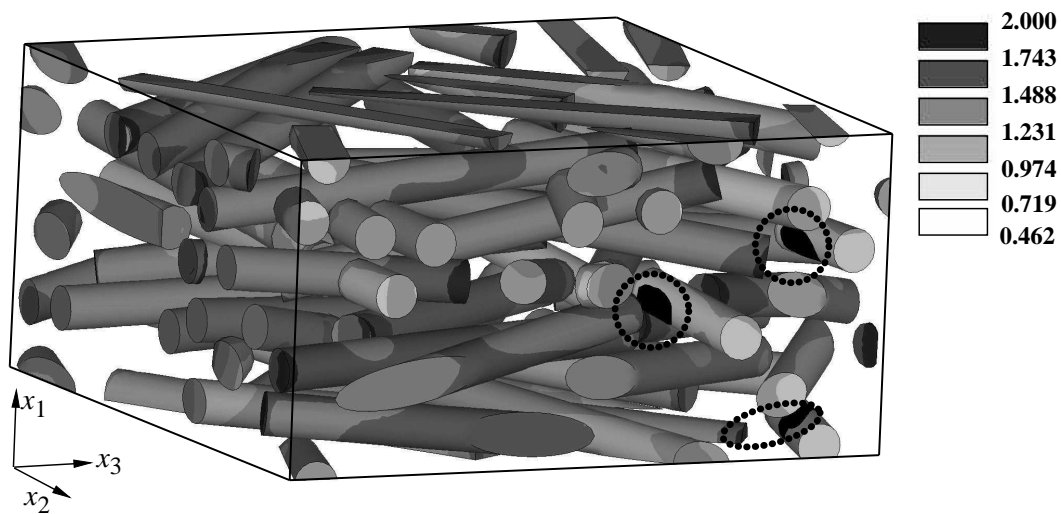


Figure 8.15: Unit cell predictions for the distributions of the temperature gradient field, $T_{,3}^{(i)}$ of the carbon fibers due to an applied far field gradient of $T_{,3}^{(*)} = 1.0$ K/m. (CELL 2, $\xi = 0.207$, 40 cylindrical short fibers, $a_1/a_2 = 10$)

8.2.3 Results for Imperfect Thermal Interfaces and Different Material Data for the Carbon Fibers

In this section investigations are extended to imperfect thermal interfaces. Additionally, the influence of the transverse fiber conductivity on the effective conductivity is studied. All calculations are carried out with the Mori–Tanaka approach and relate to carbon–copper composites with cylindrical fibers ($a_1/a_2 = 10$) that are assumed to be distributed perfectly randomly in the x_2 – x_3 –plane with no out–of–plane deviation (H–MT/2Dr). All calculations pertain to fiber volume fractions of $\xi = 0.208$. Transverse fiber conductivities of 10 W/mK and 100 W/mK are investigated.

The six investigated scenarios of interfacial degradation are referred to as *C1–C6*, the corresponding values of the interface parameter for the end faces and side faces being listed in Table 3.4. The reduced conductivities, $\bar{K}_{ij}^{(ir)}$, and the corresponding dilute concentration tensors, ${}^0\bar{D}_{ij}^{(ir)}$, are given in Table 6.3 for transverse fiber conductivities of 10 W/mK and 100 W/mK, respectively.

The predicted effective out–of–plane conductivities, $K_{11}^{(*)}$, and effective in–plane conductivities, $K_{22}^{(*)}$ and $K_{33}^{(*)}$, are listed in Table 8.4. Additionally the difference in the ef-

Table 8.4: Mori–Tanaka predictions (H–MT/2Dr) for the effective conductivities of C/Cu composites (cylindrical fibers, $a_1/a_2 = 10$, $\xi = 0.208$) with a perfect planar random fiber arrangements for different interfacial degradation scenarios and different transversal fiber conductivities. The two columns on the right hand side indicate the relative error R_{ii} of corresponding $K_{ii}^{(*)}$ ’s (based on either $K_{22}^{(i)} = 10$ or 100 W/mK), normalized with $K_{ii}^{(*)}$ as given by $K_{22}^{(i)} = 10$ W/mK.

scenario	$K_{22}^{(i)} = 10$ W/mK		$K_{22}^{(i)} = 100$ W/mK		R	
	$K_{11}^{(*)}$ [W/mK]	$K_{22}^{(*)} = K_{33}^{(*)}$ [W/mK]	$K_{11}^{(*)}$ [W/mK]	$K_{22}^{(*)} = K_{33}^{(*)}$ [W/mK]	R_{11} [–]	R_{22}, R_{33} [–]
<i>C1</i>	244.4	353.4	285.5	379.9	16.8%	7.5%
<i>C2</i>	244.1	324.9	285.4	369.1	16.9%	13.6%
<i>C3</i>	239.0	263.0	239.1	263.0	0.04%	0%
<i>C4</i>	239.0	262.3	239.1	262.4	0.04%	0.04%
<i>C5</i>	240.8	287.8	242.0	290.3	0.5%	0.9%
<i>C6</i>	240.8	284.1	242.0	286.9	0.5%	1.0%

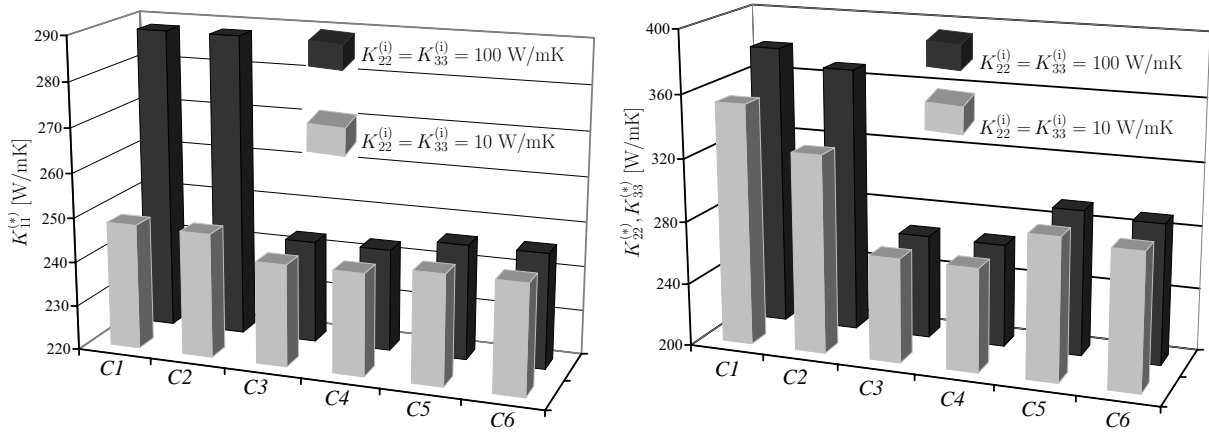


Figure 8.16: Predicted effective conductivities for a carbon–copper composite (cylindrical fibers, $a_1/a_2 = 10$, $\xi = 0.208$) with a perfect in–plane random fiber orientation distribution (no out–of–plane deviation) for different interfacial degradation scenarios and different transversal fiber conductivities. Out–of–plane conductivities are shown on the left, in–plane conductivities on the right.

fective conductivities arising from transversal inclusion conductivities of 100 W/mK and 10 W/mK with respect to the latter are provided. In Fig. 8.16 the effective conductivities are presented graphically in the form of bar diagrams.

A significant influence of the transversal fiber conductivity on the effective conductivity is only observed for the scenarios of perfectly bonded side faces, i.e. $C1$ and $C2$. For the remaining four scenarios the transversal fiber conductivity has little influence as the presence of the interfacial thermal resistance “hides” the fibers and no advantage can be gained from high transversal conductivities of the fibers. Selective debonding of the end face has essentially no influence on the effective out–of–plane conductivity.

Contrary, debonding of the end face is found to have some small, but noticeable influence on the effective in–plane conductivities, especially for the case of perfectly bonded side faces and low transversal fiber conductivities ($K_{22}^{(i)} = 10$ W/mK). The effective in–plane conductivities increase by some 10% when comparing scenarios $C3$, $C4$ and $C5$, $C6$, which relate to interface parameters as estimated for the electrochemical and the sputter coating technique, respectively.

8.3 The Influence of Microtopological Descriptors

In this section a sensitivity analysis of microtopological descriptors such as aspect ratio distribution, out-of plane misalignment, and fiber volume fraction on the effective conductivities of carbon-copper composites is carried out. The influence of interfacial thermal barriers and constituent conductivities is investigated as well and estimates on the effective conductivity are compared with measurements from literature.

Because the Mori-Tanaka estimates for randomly oriented short fibers with perfect and imperfect thermal interfaces could be shown to agree closely with unit cell predictions (see Sections 8.1 and 8.2) for moderate volume fractions, the Mori-Tanaka scheme is chosen for exploratory investigations pertaining to higher fiber volume fractions.

The bulk of the calculations is based on cylindrical fiber geometries, the cylinders having variable aspect ratios. Mainly, a hybrid multi phase Mori-Tanaka approach in combination with smooth ODFs pertaining to planar random fiber arrangements with no out-of-plane deviation (H-MT/2Dr) is employed. The studies on the effect of interfacial thermal resistance are based on spheroidal inclusion geometries, E-MT/2Dr.

8.3.1 Influence of Aspect Ratio Distributions

The fiber aspect ratio dependence of the effective conductivity of hot pressed carbon-copper composites is investigated for in-plane randomly oriented fibers, all fibers lying in the x_2 - x_3 -plane. The effective conductivities are transversally isotropic, $K_{11}^{(*)}$ denoting the out-of-plane effective conductivity and $K_{22}^{(*)}$ as well as $K_{33}^{(*)}$ the two in-plane effective conductivities, which are equal. The fiber volume fraction is set to $\xi^{(i)} = 0.5$. Cylindrical fiber shapes are assumed. Corresponding dilute concentration tensors and reduced conductivities are provided in Section 6.2 for the considered scenarios of interfacial degradation C1-C6 (Table 3.4). The conduction properties of the constituents are given in Chapter 3.

For each scenario of interfacial degradation three different composites are studied which differ only by their aspect ratio distributions. Fiber populations with constant aspect ratio of five and ten as well as one with an approximated Gaussian-like distribution of fiber aspect ratios are considered. For the latter a typical aspect ratio distribution is extracted from the experimental results shown in Fig. 3.3, Chapter 3, and approximated by five discrete aspect ratios which are given in Table 8.5. The relative volume fraction pertaining to each discrete aspect ratio is given by scaling the overall volume fraction $\xi^{(i)} = 0.5$ with the corresponding probabilities, the resulting aspect ratio distribution being listed in

Table 8.5: Aspect ratios and corresponding probabilities which approximate the aspect ratio distributions of the studied hot pressed carbon–copper composites.

a_1/a_2 [-]	2	5	7.5	10	15
probability [%]	3	30	35	27	5

Table 8.5.

In Fig. 8.17 the predicted effective out-of-plane conductivities, $K_{11}^{(*)}$, are plotted for transversal fiber conductivities of $K_{22}^{(i)}=10$ W/mK (left) and $K_{22}^{(i)}=100$ W/mK (right), respectively. The fiber aspect ratio distribution does not strongly influence the effective out-of-plane conductivity for the investigated cases, but some decrease of the effective out-of-plane conductivity with increasing fiber aspect ratio can be discerned. The predictions for the assumed Gauss-type distribution of aspect ratios lie between those obtained for the fixed aspect ratios of 5 and 10. Additional studies on planar randomly distributed cylindrical inclusions of a constant fiber aspect ratio of 7.5 showed that the corresponding effective out-of-plane conductivities differ by less than 1% from those obtained with the Gauss-type distribution. Note that small thermal interfacial resistances are required in order to take advantage of high transversal conductivities of carbon fibers. For the in-

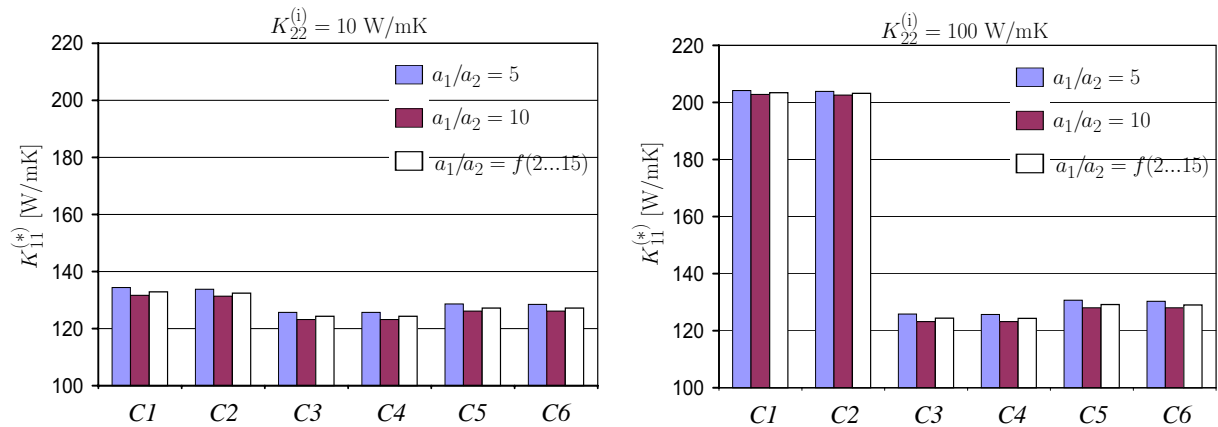


Figure 8.17: Influence of the fiber aspect ratio on the effective out-of-plane conductivity of a carbon–copper composite ($\xi^{(i)} = 0.5$ as predicted with a hybrid Mori–Tanaka method (H–MT/2Dr); planar random fiber arrangement with no out-of-plane deviation, conduction properties from Chapter 3) for transverse fiber conductivities of 10 W/mK (left) and 100 W/mK (right) and for different scenarios of interfacial degradation (Table 3.4).

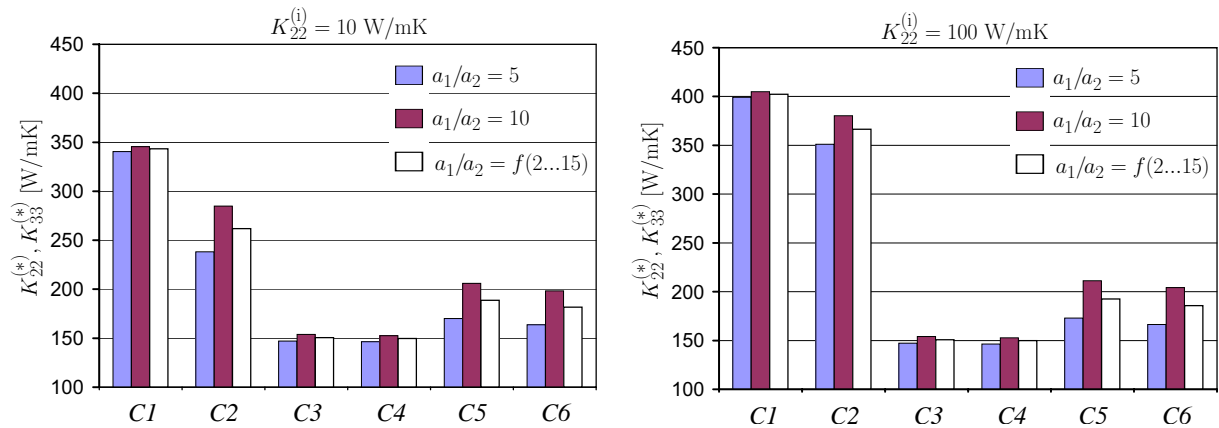


Figure 8.18: Influence of the fiber aspect ratio on the effective in-plane conductivity of a carbon-copper composite ($\xi^{(i)} = 0.5$ as predicted with a hybrid Mori-Tanaka method (H-MT/2Dr); planar random fiber arrangement with no out-of-plane deviation, conduction properties from Chapter 3) for transverse fiber conductivities of 10 W/mK (left) and 100 W/mK (right) and for different scenarios of interfacial degradation (Table 3.4).

investigated interfacial configurations $C3$ – $C6$ the interface conductance is so small that the fibers are effectively “hidden” and no advantage can be gained from using carbon fibers of superior conduction properties.

In Fig. 8.18 the effective in-plane conductivities, $K_{22}^{(*)}$ and $K_{33}^{(*)}$, are plotted for transversal fiber conductivities of $K_{22}^{(i)}=10 \text{ W/mK}$ (left) and $K_{22}^{(i)}=100 \text{ W/mK}$ (right), respectively. With increasing fiber aspect ratio the effective in-plane conductivity increases. For the case of perfect thermal interfaces ($C1$) the estimates on the effective in-plane conductivities for reinforcement geometries of constant aspect ratio of 5 and 10 differ by approximately 5 W/mK. However, in case of failure of the end face interfaces ($C2$) the predictions differ by some 50 W/mK and 30 W/mK for transverse fiber conductivities of 10 W/mK and 100 W/mK, respectively. Also, for the configurations $C5$ and $C6$ significant differences in the in-plane conductivities are observed for reinforcements of constant aspect ratios of 5 and 10. This effect is “conductivity driven” – the greater the aspect ratio is, the larger the corresponding reduced conductivities are. Especially, thermal failure of the end face interfaces can be compensated much better by fibers of increased aspect ratios. The effective conductivities as predicted for reinforcements conforming to the studied Gauss-type distribution of aspect ratios are in between the conductivities as obtained for reinforcements of constant aspect ratios 5 and 10. Additional studies on planar randomly distributed cylindrical inclusions of a constant aspect ratio of 7.5 showed that the

corresponding effective in-plane conductivities exceed those obtained for the Gauss-type distribution by less than 2%. Note that the matrix conductivity of 360 W/mK is only exceeded for perfectly bonded side faces, $C1$ and $C2$, in combination with high transverse inclusion conductivities of 100 W/mK.

8.3.2 Influence of Out-of-Plane Misalignment

The investigated hot pressed carbon-copper composites typically contain fibers that are randomly oriented in the in-plane direction (the plane normal to the pressing direction) with some out-of-plane misalignment. The effects of this out-of-plane misalignment on the effective conductivities are studied in the following. Cylindrical fiber geometries and a Gauss-type distribution of the aspect ratios following Table 8.5 are assumed. The estimates pertain to fiber volume fractions of $\xi^{(i)} = 0.5$ and are obtained with a hybrid Mori-Tanaka scheme the ODF being smooth, H-MT. Conduction properties of the constituents are given in Chapter 3, corresponding dilute concentration tensors and reduced conductivities are given in Section 6.2.

Figure 8.19 shows the effect of out-of-plane deviations of the fiber orientations on both the effective in-plane conductivities, $K_{22}^{(*)}$ and $K_{33}^{(*)}$ (solid lines), and the effective out-of-plane conductivities, $K_{11}^{(*)}$ (dashed lines), where ϕ denotes the truncation angle of a uniform probability density function, $\rho(\Psi_1)$. Out-of-plane misalignment influences the effective in-plane conductivities more than the effective out-of-plane conductivities. As the reduced conductivities decrease, i.e. the interfacial thermal resistances increase, the dependence of $K_{ij}^{(*)}$ on ϕ decreases significantly. Note that for $\phi = 0^\circ$ all fibers contain within the x_2 - x_3 -plane and the results for $K_{11}^{(*)}$ and $K_{22}^{(*)}$, $K_{33}^{(*)}$ coincide with the white bars as shown in Fig. 8.18 and Fig. 8.17, respectively (H-MT/2Dr). For $\phi = 90^\circ$ the out-of-plane and in-plane conductivities coincide and a three dimensional random fiber arrangement of isotropic overall conductivity is obtained (H-MT/3Dr).

The bulk of reinforcements of the investigated hot pressed carbon-copper composites does not exceed out-of-plane deviations of more than $\phi = 10^\circ$?, which leads to minor effects only. Accordingly, in the following all results presented pertain to perfectly planar random arrangements.

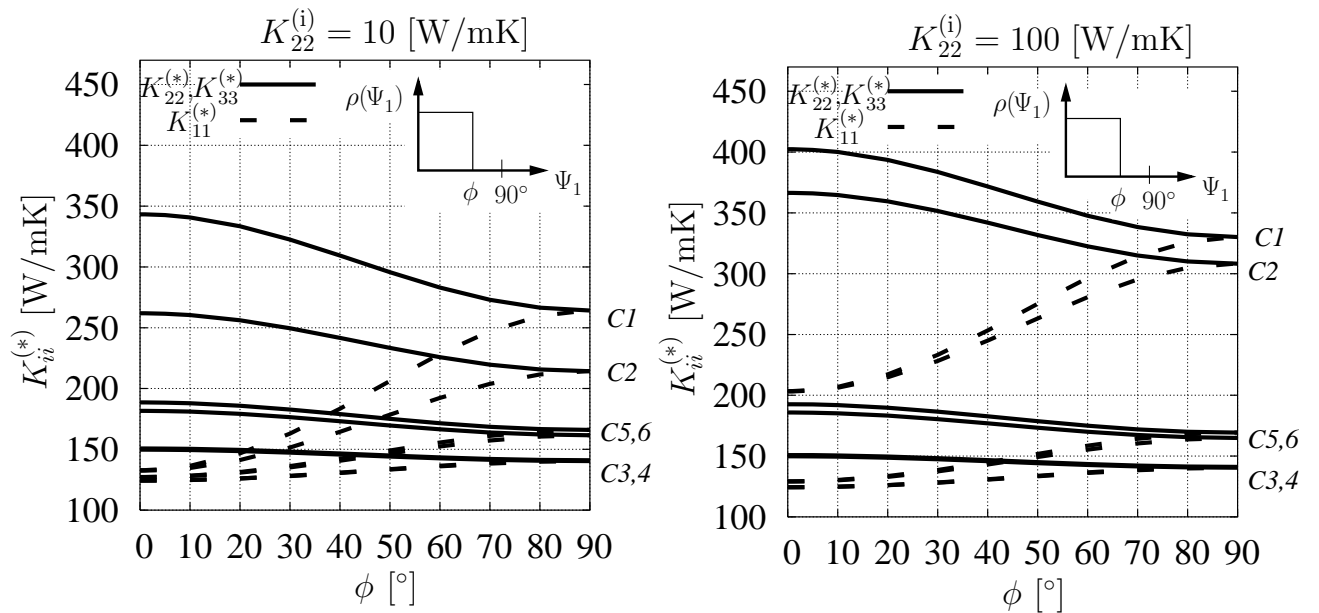


Figure 8.19: The dependence of the effective conductivity of a carbon copper composite ($\xi^{(i)} = 0.5$; Gauss-type aspect ratio distribution following Table 8.5; predicted with a hybrid Mori–Tanaka scheme (H–MT), cylindrical fibers, conduction properties of the constituents see Chapter 3) on the out-of-plane deviation ϕ of the fiber orientation angles for transverse fiber conductivities of 10 W/mK (left) and 100 W/mK (right).

8.3.3 Influence of Interfacial Thermal Resistance

The influence of the interfacial thermal resistance on the effective conductivity of a planar random fiber arrangement without out-of-plane deviation is studied. The interfacial thermal resistance is varied from perfectly insulating, $\beta \rightarrow 0$, to perfectly conducting, $\beta \rightarrow \infty$, and assumed to be distributed evenly on the surface of the inclusions (corresponding to a LC-type coating of constant thickness). Because for uniformly distributed thermal resistances the reduced conductivities and dilute concentration tensors for spheroidal and cylindrical inclusions agree closely (Section 5.2), inclusions of spheroidal shape are considered for now. This has the advantage that the analytical replacement operation as discussed in Section 5.1 can be invoked, which is less time consuming than the numerical, unit cell based replacement operation for cylinders.

The imperfectly bonded spheroids are assumed to have a constant aspect ratio $a_1/a_2 = 7.5$ and their “equatorial” radius equals $5 \mu\text{m}$. The inclusion volume fraction is fixed at $\xi = 0.5$. Axial inclusion conductivities of 1000 W/mK and 100 W/mK in combination with transverse inclusion conductivities of 100 W/mK and 10 W/mK are considered, giving rise to

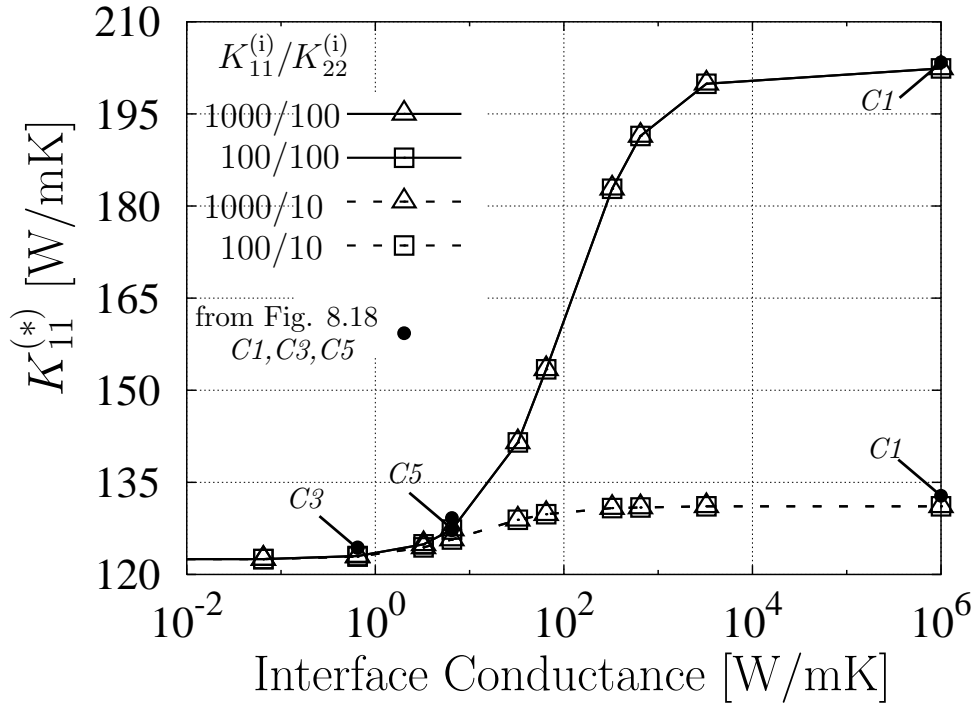


Figure 8.20: The influence of the interface conductance (βa_2) on the effective out-of-plane conductivity of a carbon-copper composite ($\xi^{(i)} = 0.5$; planar randomly oriented spheroidal fibers with no out-of-plane deviation, $a_2 = 5 \mu\text{m}$, $a_1/a_2 = 7.5$, $K^{(m)} = 360 \text{ W/mK}$) for axial fiber conductivities of 100 W/mK and 1000 W/mK and transverse fiber conductivities of 10 W/mK and 100 W/mK predicted with an extended Mori-Tanaka method (E-MT/2Dr). The solid circles correspond to predictions based on cylindrical fibers (H-MT/2Dr), see Fig. 8.18.

four different inclusion conduction types, each of which is considered. The matrix conductivity equals 360 W/mK.

The predicted effective out-of-plane conductivities, $K_{11}^{(*)}$, are plotted in Fig. 8.20 versus the interface conductance, βa_2 , as introduced in Eq. (5.23). The curves relating to the same transverse inclusion conductivities, 10 W/mK and 100 W/mK, coincide. The latter effect is due to two characteristics associated with the employed averaging procedure to obtain reduced conductivities and with orthotropic ellipsoidal inclusions in general. As explained in Section 5.1 the estimates on the reduced conductivity $\bar{K}_{ii}^{(ir)}$ (no sum over i) in a given direction i are only influenced by the size of the inclusion and its conductivity $K_{ii}^{(i)}$ (no sum over i) but is independent of the conductivities in the normal directions, $K_{jj}^{(i)}$ (no sum over j). Accordingly, equally sized inclusions with the same transverse conductivity and

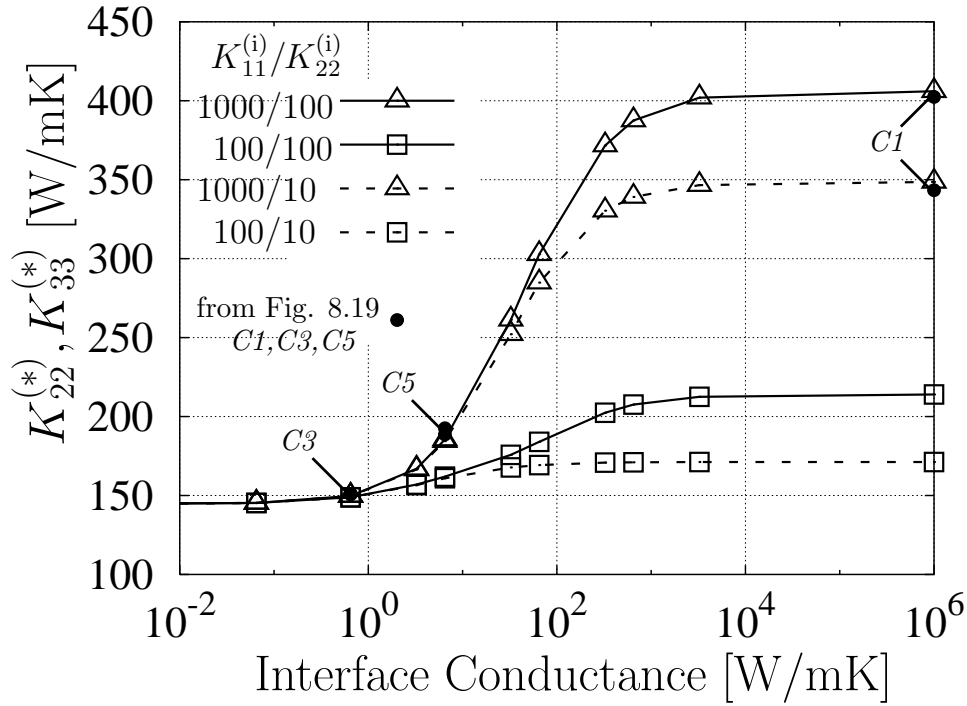


Figure 8.21: The influence of the interface conductance (βa_2) on the effective in-plane conductivity of a carbon-copper composite ($\xi^{(i)} = 0.5$; planar randomly oriented spheroidal fibers with no out-of-plane deviation, $a_2 = 5 \mu\text{m}$, $a_1/a_2 = 7.5$, $K^{(m)} = 360 \text{ W/mK}$) for axial fiber conductivities of 100 W/mK and 1000 W/mK and transverse fiber conductivities of 10 W/mK and 100 W/mK predicted with extended Mori-Tanaka method (E-MT/2Dr). The solid circles correspond to predictions based on cylindrical fibers (H-MT/2Dr), see Fig. 8.18.

distribution of the interface parameter will have the same reduced transverse conductivities, independent of their axial conductivities. Secondly, due to the perfect in-plane distribution of the spheroids (no out-of-plane deviation) and the Eshelby property of spheroids the effective out-of-plane conductivity, $K_{11}^{(*)}$, depends on the transverse conductivity of the replacement inclusion only.

A typical S-shape is observed ????. The measured values of the interface parameter β^{ec} and β^{sp} (see Section 3), together with a characteristic length of $a_2 = 5 \mu\text{m}$ yield interface conductances of 0.65 W/mK and 6.5 W/mK, respectively (corresponding to the scenarios C3 and C5 of interfacial degradation, see Table 3.4). A great potential for gaining higher effective out-of-plane conductivities via improving the interfacial thermal barriers is evident for transverse inclusion conductivities of 100 W/mK. The gain reduces as the transverse

inclusion conductivities decrease. The solid circles in Fig. 8.20 show the effective out-of-plane conductivities as predicted with a Gauss-type aspect ratio distribution (Table 8.5) of cylinders for the cases *C1*, *C3*, and *C5*. It shows that for the case of constant interface parameters a spheroidal approximation of cylindrical fibers provides excellent results.

The predicted effective in-plane conductivities, $K_{22}^{(*)}$ and $K_{33}^{(*)}$, are plotted in Fig. 8.21 versus the interface conductance. Again, a typical S-shape is observed. The reduced axial inclusion conductivity dominates the effective in-plane behavior of the composite, the transverse conductivity playing a secondary role, especially for small and intermediate interface conductances. Good agreement between the estimates based on spheroids and cylinders is found (bullets, Fig. 8.21). Reducing the thermal resistance of the carbon-copper interface can significantly increase the effective in-plane conductivity, especially for high axial inclusion conductivities.

8.3.4 Influence of Inclusion Volume Fraction

For planar randomly distributed cylindrical fibers (no out-of-plane deviation) and a Gauss-type distribution of the aspect ratios following Table 8.5 the influence of the fiber volume fraction on the effective out-of-plane conductivity $K_{11}^{(*)}$ (Fig. 8.22) and on the effective in-plane conductivities $K_{22}^{(*)}$ and $K_{33}^{(*)}$ (Fig. 8.23) is studied with a hybrid Mori-Tanaka method, H-MT/2Dr. The conduction properties of the constituents are given in Chapter 3. All six scenarios of interfacial degradation, *C1*–*C6* (Table 3.4), are considered.

The out-of-plane conductivity is practically independent of a possible failure of the end face interface, so that the curves for *C1* and *C2*, *C3* and *C4*, as well as for *C5* and *C6*, coincide (see Fig. 8.22). For the case of thermal perfect side faces (scenarios *C1* and *C2*) transverse inclusion conductivities of 10 W/mK (Fig. 8.22, left) and 100 W/mK (Fig. 8.22, right) give rise to significantly different predictions. For the considered values of β corresponding to scenarios *C3*–*C6* the out-of-plane conductivities are practically independent of the transversal inclusion conductivity, i.e. no advantage can be drawn from high transversal inclusion conductivities in the presence of high interfacial resistances.

Similar observations hold for the effective in-plane conductivities. Except for scenarios *C1* and *C2* the transverse inclusion conductivity has no influence on the effective conductivities for the studied interface parameters β and inclusion dimensions. A significant reduction of the effective in-plane conductivities due to selective failure of the end face interfaces is only observed for the case of perfectly bonded side faces. Some slight reduction

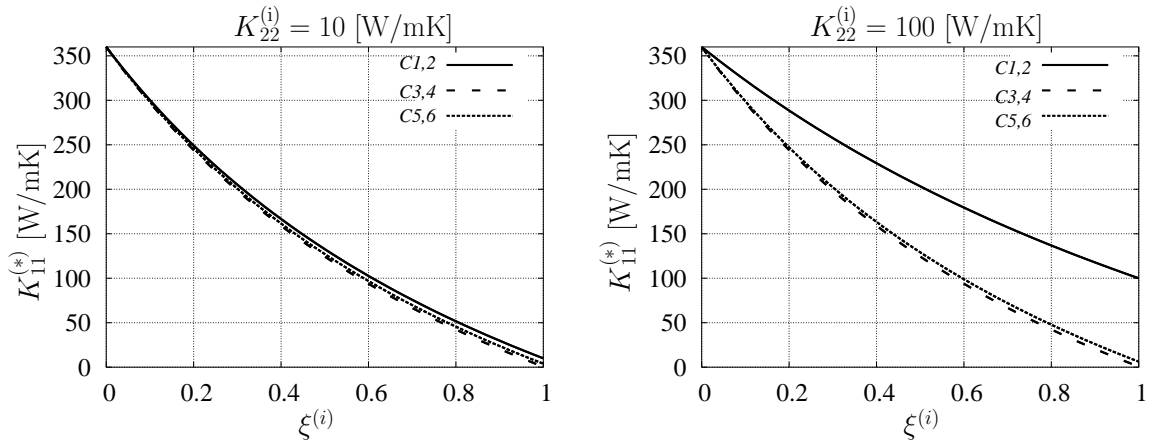


Figure 8.22: Dependence of the effective out-of-plane conductivity of a carbon-copper composite (cylindrical fibers, Gauss-type aspect ratio distribution following Table 8.5, planar random arrangement with no out-of-plane deviation, conductivities of constituents are given in Chapter 3) on the fiber volume fraction for transverse fiber conductivities of 10 W/mK (left) and 100 W/mK (right) predicted with a hybrid Mori-Tanaka method, (H-MT/2Dr).

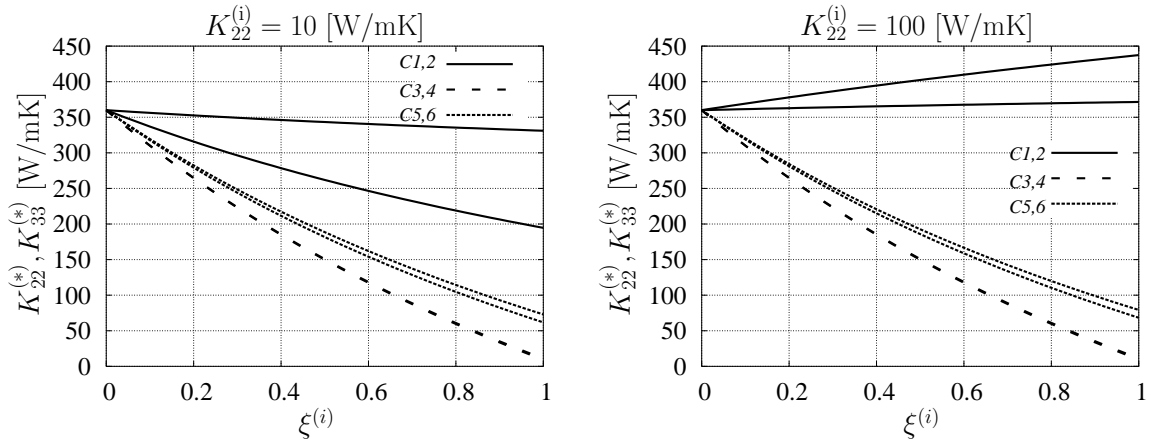


Figure 8.23: The dependence of the effective in-plane conductivity of a carbon-copper composite (cylindrical fibers, Gauss-type aspect ratio distribution following Table 8.5, planar random arrangement with no out-of-plane deviation, conductivities of constituents are given in Chapter 3) on the fiber volume fraction for transverse fiber conductivities of 10 W/mK (left) and 100 W/mK (right) predicted with a hybrid Mori-Tanaka method, (H-MT/2Dr).

is present for the scenarios relating to β^{sp} , i.e. $C5$ and $C6$.

8.3.5 Comparison with Experiments

In Fig. 8.24 hybrid Mori–Tanaka predictions of the effective conductivity of carbon–copper composites are compared with measurements. The effective conductivities of planar randomly oriented cylindrical fibers, which conform to a Gauss–type distribution of aspect ratios according to Table 8.5, are predicted with a hybrid Mori–Tanaka scheme, H–MT/2Dr. Six different scenarios of interfacial degradation (Table 3.4) in combination with transverse fiber conductivities of $K_{22}^{(i)} = 100$ W/mK are accounted for. In addition, results are provided for transverse fiber conductivities of $K_{22}^{(i)} = 10$ W/mK for perfectly bonded side faces, i.e. scenario C1 and C2. Note that the corresponding results for the remaining four scenarios, C3–C6, almost coincide with those pertaining to fibers of the higher transverse conductivity of $K_{22}^{(i)} = 100$ W/mK.

The experimental results correspond to measurements reported by Neubauer ? (squares), from Korb *et al.* ? (circles), and from Buchgraber ? (triangles pointing upwards). Triangles pointing downwards (Buchgraber*) pertain to a carbon–copper composite with a non–uniform fiber distribution. All measurements pertain to carbon fibers which have been copper coated via the electrochemical route.

All measured values lie below the predictions for fiber with perfect side face interfaces, indicating the presence of reduced interfacial conductances. Experimental data results on

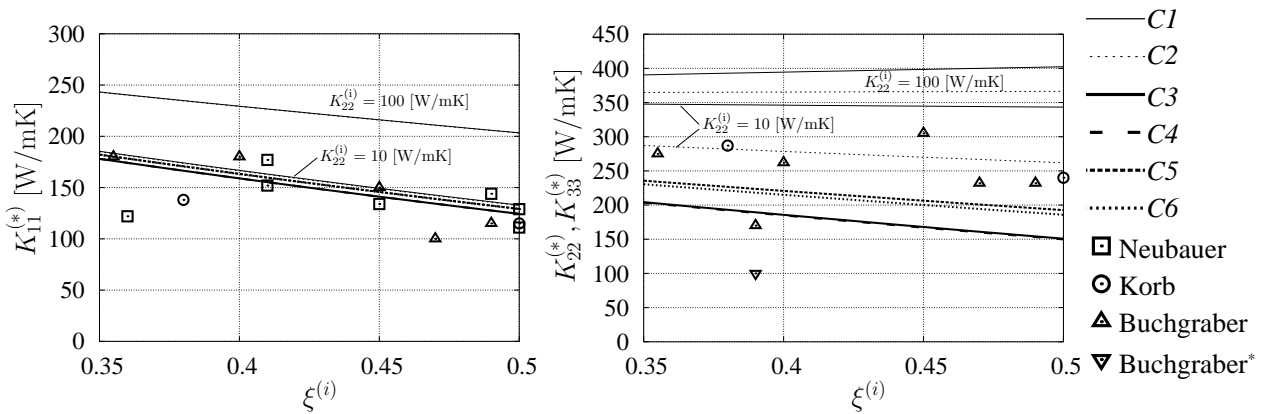


Figure 8.24: The lines show the effective out–of–plane (left) and in–plane (right) conductivities (cylindrical fibers, Gauss–type aspect ratio distribution) for C/Cu composites (material data is given in Chapter 3) as predicted with a hybrid Mori–Tanaka method (H–MT/2Dr). The symbols show measurements and are taken from Neubauer ? (squares), Korb *et al.* ? (circles), and Buchgraber ? (triangles).

the in-plane behavior suggest, however, that the interface conductances may be somewhat better than the values used for the present study. As the in-plane conductivity is considerably more sensitive to interfacial thermal resistances than is the out-of-plane conductivity, a increase of the interface parameter β would result in a better agreement between the numerical predictions for the in-plane conductivity and the measurements, while at the same time the predictions for the out-of-plane conductivity would not “drift away”, maintaining the excellent agreement with the measurements.

This effect can also be observed when comparing the behavior of the effective out-of-plane and in-plane conductivities on the interface conductance as displayed in Figs. 8.20 and 8.21, respectively. Considering interface conductances as determined by an interface parameter β^{ec} (i.e. electrochemical coating, marked as *C3*), it shows that both, the effective in-plane and out-of-plane conductivities, are almost independent of the conductivities of the fibers as the interfacial resistance is “hiding” them. For an interface conductance relating to β^{sp} (i.e. sputter technique, marked as *C5*), the situation has not changed much for the out-of-plane conductivities (Fig. 8.20) and some minor dependence on the fiber conductivities is showing. The corresponding in-plane conductivities (Fig. 8.21), however, are gaping apart more than 30 W/mK for the chosen fiber conductivities and interface conductance.

Chapter 9

Conclusions

In this work the effective thermal conductivity of carbon–copper composites was studied, special attention being paid to the effects of imperfect thermal interfaces. A unit cell approach solved with the FEM and an extended Mori–Tanaka mean field approach were employed. The localization capabilities of the latter method were improved significantly. Both micromechanical methods for obtaining estimates on the effective conductivity were subjected to thorough and critical discussion.

An analytical method was developed that enables studies of the effects of imperfect thermal interfaces between matrix and ellipsoidal inclusions. It is based on the idea of replacing the inclusion and the thermal barrier by a perfectly bonded but less conductive inhomogeneity. For “confocal” interfacial resistances a solution for interphases of finite thickness known from the literature was recovered. For more general distributions of interfacial resistances a straightforward and accurate approximation was developed. Subsequently, this idea of a replacement operation was applied to imperfectly bonded inclusions of arbitrary shape, numerical unit cell methods being used to evaluate the corresponding dilute concentration tensors and reduced conductivities.

For the case of imperfect thermal interfaces size effects that are known from the literature could be identified. They can be interpreted such that for inclusions of greater size the impact of an interfacial thermal resistance on the overall response is less severe than for small ones. The above solutions, in turn, could be used within Mori–Tanaka methods to provide a versatile, hybrid micromechanical tool for studying the thermal conduction behavior of nondilute composites with nonideal interfaces.

The “dilute” unit cell approach was also used to study and compare the averaged tem-

perature gradient fields and flux fields in spheroidal and cylindrical inclusions. A wide range of technical relevant sets of conductivities and aspect ratios was investigated for the case of perfect thermal interfaces. If the axial inclusion conductivities exceed the matrix conductivity, the averaged temperature gradient fields and flux fields of spheroids and cylinders were found to differ significantly for applied far fields in axial direction. For applied far fields in the transverse direction smaller discrepancies were observed between the averaged temperature gradient and flux fields of spheroids and cylinders. Dilute spheroidal and cylindrical carbon fibers that are bonded imperfectly to the copper matrix were investigated. It was found that especially for selective failure of the end face interface predictions based on spheroids and cylinders can differ significantly.

On the basis of the above results the thermal conductivity of carbon–copper composites of technically relevant fiber volume fractions was investigated. Different fiber arrangements, different configurations of interfacial thermal resistances as well as different conductivities of the carbon fibers were taken into account. Cylindrical and spheroidal inclusion shapes and their influence on the effective behavior were compared.

It was predicted that the thermal interfacial resistances typically associated with carbon fibers in a copper matrix severely reduce the effective conductivities of the resulting composites. Consequently, the overall conductivity of such MMCs can be significantly increased, if the interfacial thermal resistance between carbon and copper is decreased. Selective debonding of the end faces was found to reduce the effective conductivities to a significant degree only for the case of perfectly bonded side faces. In the presence of imperfectly bonded side faces, additional failure of the end faces was found to reduce the effective conductivity only insignificantly.

Microgeometries with aligned continuous fibers and staggered short fibers as well as three dimensional random and planar random arrangements of short fibers were studied. Except for the case of staggered short fibers the Mori–Tanaka predictions and unit cell predictions were found to agree very well, independent of the spatial variation of the interface parameter. The influence of various microgeometrical descriptors on the effective conductivity was studied comprehensively with a hybrid Mori–Tanaka approach. Good agreement with experiments was found.

Appendix A

Appendix: Transformation Tensor and Orientational Averaging

Transformation Tensor

The elements of vectors u_i and second rank tensors U_{ij} which are defined in different coordinate systems, e.g. a global coordinate system x_i and a local coordinate system ${}^l x_i$, can be related to each other via the second rank transformation tensor T_{ij} in the following way

$$\begin{aligned} {}^\angle u_i &= T_{ij} {}^l u_j \\ {}^\angle U_{ij} &= T_{ik} T_{jl} {}^l U_{kl} \quad , \end{aligned} \tag{A.1}$$

here the superscript \angle refers to tensors given with respect to the global coordinate system. The elements of the transformation tensor are given as

$$T_{ij} = \cos(\angle x_i {}^l x_j) \quad , \tag{A.2}$$

see e.g. ??, where \angle denotes the angle between two orientations.

Misaligned Inclusion

In the following inclusions of axisymmetric shape are considered, the axis of rotational symmetry of which coincides with ${}^l x_1$ (Fig. A.1). Additionally, for the equations to hold, the material symmetry of the inclusions is restricted to transversal isotropy, the axis of isotropy

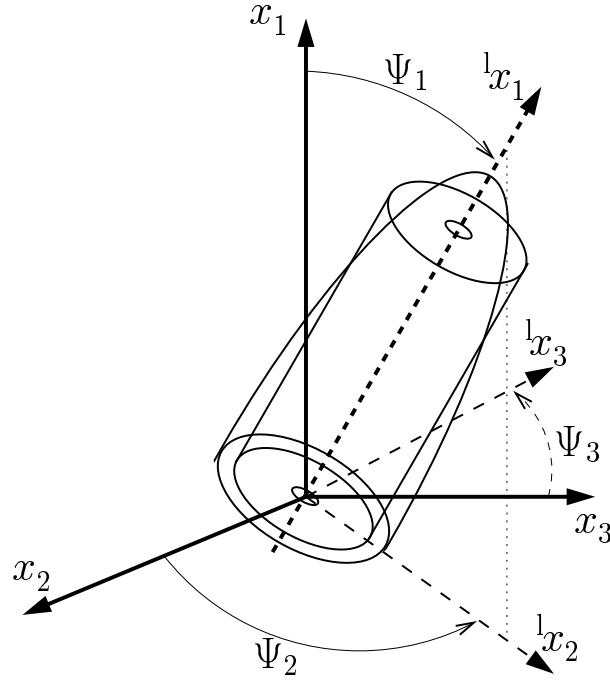


Figure A.1: Two inclusions of axisymmetric geometry of a given orientation, definition of the angles Ψ_1 , Ψ_2 , and Ψ_3 .

being aligned with ${}^l x_1$. Two angles, Ψ_1 and Ψ_2 , are sufficient for describing the orientation of the inclusion with respect to a global coordinate system. For the configuration as depicted in Fig. A.1 the transformation tensor T_{ij} can be provided as a function of Ψ_1 and Ψ_2 and reads

$$T_{ij} = \begin{bmatrix} \cos(\Psi_1) & 0 & \sin(\Psi_1) \\ \sin(\Psi_1) \sin(\Psi_2) & \cos(\Psi_2) & -\cos(\Psi_1) \sin(\Psi_2) \\ -\sin(\Psi_1) \cos(\Psi_2) & \sin(\Psi_2) & \cos(\Psi_1) \cos(\Psi_2) \end{bmatrix}. \quad (\text{A.3})$$

The transposed transformation tensor equals its inverse, i.e. $T_{ij}^{-1} = T_{ji}$. If the inclusion is aligned with the global coordinate system then T_{ij} equals δ_{ij} .

The above description implies that the local ${}^l x_2$ -axis is oriented such that it is in the global x_2 - x_3 -plane, note that T_{12} equals zero. The diagonal terms of the transformation tensors contain the angles between corresponding local and global principal axes (Eq. (A.2)), implying the angle subtended between x_3 and ${}^l x_3$, Ψ_3 , is tied to Ψ_1 and Ψ_2 such that

$$\cos(\Psi_3) = \cos(\Psi_1) \cos(\Psi_2) \quad (\text{A.4})$$

holds. Descriptions based on three independent angles (x_2 has “out-of-plane” orientations) result in complicated trigonometrical functions for each element of T_{ij} and Eq. (A.4) loses validity.

Orientalional Averaging

Inclusion families are composed of similar inclusions which are distributed according to the ODF of each family, $\rho^{(r)}$ ($r = 1, 2, \dots, N$). Orientalional averaging of the respective local vectors ${}^l u_i^{(r)}$ and local second rank tensors ${}^l U_{ij}^{(r)}$ of the r^{th} -inclusion phase must be performed in one coordinate system. The global coordinate system is chosen for averaging for all inclusions.

For vectors weighted averaging as prescribed by the ODF can be expressed as

$$\begin{aligned} \bar{u}_i^{(r)} &= \left\langle {}^l u_i^{(r)} \right\rangle \\ &= \frac{1}{\bar{\rho}^{(r)}} \int_{\Psi_1=0}^{\pi/2} \int_{\Psi_2=0}^{2\pi} T_{ij}(\Psi_1, \Psi_2) {}^l u_j^{(r)} \rho^{(r)} \sin(\Psi_1) \, d\Psi_1 d\Psi_2 \end{aligned} \quad (\text{A.5})$$

and for second rank tensors as

$$\begin{aligned} \bar{U}_{ij}^{(r)} &= \left\langle {}^l U_{ij}^{(r)} \right\rangle \\ &= \frac{1}{\bar{\rho}^{(r)}} \int_{\Psi_1=0}^{\pi/2} \int_{\Psi_2=0}^{2\pi} T_{ik}(\Psi_1, \Psi_2) {}^l U_{kl}^{(r)} T_{lj}^{-1}(\Psi_1, \Psi_2) \rho^{(r)} \sin(\Psi_1) \, d\Psi_1 d\Psi_2 \end{aligned} \quad (\text{A.6})$$

where $\bar{\rho}^{(r)}$ is defined as

$$\bar{\rho}^{(r)} = \int_{\Psi_1=0}^{\pi/2} \int_{\Psi_2=0}^{2\pi} \rho^{(r)} \sin(\Psi_1) \, d\Psi_1 d\Psi_2 \quad (\text{A.7})$$

for each inclusion phase respectively.

Within the framework of the proposed Mori–Tanaka theory only Eq. (A.6) needs to be employed a maximum of two times for each inclusion family – on the one hand averaged inclusion conductivities and resistivities for determining the effective conductivity (Eqs. (4.22–4.24)) and on the other hand averaged dilute temperature gradient concentration tensors, ${}^0 \bar{D}_{ij}^{(r)}$, and averaged dilute flux concentration tensors, ${}^0 \bar{F}_{ij}^{(r)}$ (Eq. (4.30)). Orientalional averaging of the conductivities and resistivities is not necessary for isotropic material properties. Note that the above integrals are evaluated numerically, the integral being replaced by a sum.

For perfectly bonded spheroidal inclusion families the above integrals are integrals over constant properties within the framework of the proposed theory due to the Eshelby-properties, i.e. no bar on top of the “ u ’s” and “ U ’s” in Eq. (A.5) and Eq. (A.6) is required. However, one must keep in mind that for imperfectly bonded spheroidal inclusions or cylindrical inclusions the above integrals are integrals over ”quasi-constant” properties, i.e. the fluctuating microfields have been replaced on a dilute level by averaged microfields.

Dominik Duschlbauer

Personal

Date of Birth: 05.12.1973
Place of Birth: Linz, Austria
Nationality: Austrian
Marital Status: married to Lisa Keiko Duschlbauer
son Dorian Duschlbauer (born 19.02.2002)

Education

January 2001 PhD-student at the Institute of Lightweight Structures and Aerospace Engineering, *Vienna University of Technology*, Vienna, Austria; research fields: computational micromechanics of materials; doctoral thesis: “Computational simulation of the thermal conductivity of MMCs under consideration of the inclusion-matrix interface”.

March 2000 Graduation to “Diplom-Ingenieur” (MSc) for Mechanical Engineering with honors at the *Technical University of Graz*, Graz, Austria.

1993–2000 Studies of Mechanical Engineering at the *Technical University of Graz*, Graz, Austria; main topics: energy technology, thermal and hydraulic turbomachinery; diploma-thesis in cooperation with *VA Tech Hydro* “Development of an experimental set-up to investigate the fluid dynamics of the backspace of a runner with respect to leakage, disc friction and axial thrust.”

1996/1997 Studies of Mechanical Engineering at the *University of Sydney*.

1984–1992 Grammar school in Freistadt, Austria.

Industrial Experience

June–December 2000 Mechanical engineer, Division of Materials Technology, *Austrian Research Centers*, Seibersdorf, Austria.

1997–2000 Free lance contributor in the field of vibration analysis, *AVL*, Graz, Austria.

1999 Diploma thesis, *VA Tech Hydro*, Linz, Austria.

Other Experience

1992/1993 Special training with the Austrian Armed Forces and qualified as Second Lieutenant.